A Total Lagrangian upwind Smooth Particle Hydrodynamics algorithm for large strain explicit solid dynamics

Chun Hean Lee [a,1], Antonio J. Gil [b,2], Ataollah Ghavamian [b], Javier Bonet [c]

(a) Glasgow Computational Engineering Centre, School of Engineering
University of Glasgow, Glasgow, G12 8QQ, United Kingdom
(b) Zienkiewicz Centre for Computational Engineering, College of Engineering
Swansea University, Bay Campus, SA1 8EN, United Kingdom
(c) University of Greenwich, London, SE10 9LS, United Kingdom

Abstract

In previous work [1, 2], Lee *et al*. introduced a new Smooth Particle Hydrodynamics (SPH) computational framework for large strain explicit solid dynamics with special emphasis on the treatment of near incompressibility. A first order system of hyperbolic equations was presented expressed in terms of the linear momentum and the minors of the deformation, namely the deformation gradient, its co-factor and its Jacobian. Taking advantage of this representation, the suppression of numerical deficiencies (e.g. spurious pressure, long term instability and/or consistency issues) was addressed through well-established stabilisation procedures. In Reference [1], the adaptation of the very efficient Jameson-Schmidt-Turkel algorithm was presented. Reference [2] introduced an adapted variationally consistent Streamline Upwind Petrov Galerkin methodology. In this paper, we now introduce a third alternative stabilisation strategy, extremely competitive, and which does not require the selection of any user-defined artificial stabilisation parameter. Specifically, a characteristic-based Riemann solver in conjunction with a linear reconstruction procedure is used, with the aim to guarantee both consistency and conservation of the overall algorithm. We show that the proposed SPH formulation is very similar in nature to that of the upwind vertex centred Finite Volume Method presented in [3]. In order to extend the application range towards the incompressibility limit, an artificial compressibility algorithm is also developed. Finally, an extensive set of challenging numerical examples is analysed. The new SPH algorithm shows excellent behaviour in compressible, nearly incompressible and truly incompressible scenarios, yielding second order of convergence for velocities, deviatoric and volumetric components of the stress.

Keywords: Conservation laws, SPH, Upwind, Riemann Solver, Explicit dynamics, Incompressibility

1. Introduction

The classical (displacement-based) Smooth Particle Hydrodynamics (SPH) Lagrangian formalism [4–10] is well-known to suffer from a number of severe drawbacks, namely: (1) tensile

[1]Corresponding author: chunhean.lee@glasgow.ac.uk. This work was completed whilst at the previous affiliation: Zienkiewicz Centre for Computational Engineering, College of Engineering, Swansea University, Bay Campus, SA1 8EN, United Kingdom

[2]Corresponding author: a.j.gil@swansea.ac.uk

instability, spurious pressure and hour-glassing [11, 12]; (2) numerical issues associated with conservation, consistency, long term stability and convergence [13, 14] and (3) the reduced order of convergence for derived variables (e.g. stresses and strains) [15–18].

Over the last two decades, significant effort has been devoted to enhance the robustness of classical SPH algorithms. The numerical deficiencies described above can be partially alleviated through the use of corrected kernel gradient approximations, combined with so-called non-consistent stabilisation strategies [8] (i.e. artificial viscous fluxes [4, 19, 20] and conservative strain smoothing regularisation [15, 21]). As reported in References [6, 8], the above enhanced SPH methodologies ensure the reproducibility of complete polynomial basis in finite domains [5, 22–24]), but still suffer from persistent artificial mechanisms similar to hour-glassing when attempting to model problems with predominant nearly incompressible behaviour.

In very recent works [1, 2], some of the authors of the present manuscript have successfully introduced a mixed-based SPH computational framework for explicit fast solid dynamics, where the conservation of linear momentum $\boldsymbol{p}$ is solved along with conservation equations for the deformation gradient $\boldsymbol{F}$, its co-factor $\boldsymbol{H}$ and its Jacobian J. Specifically, the SPH discretisation of the new system of conservation laws $\{\boldsymbol{p}, \boldsymbol{F}, \boldsymbol{H}, J\}$ was introduced through a family of well-established stabilisation strategies, namely a Jameson-Schmidt-Turkel (JST) algorithm [25, 26] and a variationally consistent Streamline Upwind Petrov Galerkin (SUPG) algorithm [2, 27]. Both computational methodologies were capable of eliminating spurious hourglass-like modes and spurious pressure oscillations in nearly incompressible scenarios.

The main objective of the current paper is to explore a third alternative SPH spatial discretisation of the same system $\{\boldsymbol{p}, \boldsymbol{F}, \boldsymbol{H}, J\}$ by means of a very competitive Riemann solver based stabilisation methodology, without the need to introduce any artificial stabilisation parameters. The mixed-based set of equations is advanced in time by means of an explicit time integrator, where the time step is controlled through the Courant-Friedrichs-Lewy number [28] dependent on the volumetric wave speed c_p. We also show that the new SPH algorithm is very similar to an upwind vertex centred FVM [3], where the latter requires the generation of a dual mesh using the medial dual approach [29]. In the near (or full) incompressibility limit, the wave speed c_p can reach very high (even infinite in the degenerate case) values potentially leading to a very inefficient algorithm [26, 30]. To address this issue, we then present an adapted artificial compressibility algorithm [31–33], supplemented with the use of a (conservative) Laplacian viscosity term, if necessary, to allow for the explicit simulation of (nearly) incompressible solids.

The paper is organised as follows. Section 2 briefly summarises the system of first order conservation laws $\{\boldsymbol{p}, \boldsymbol{F}, \boldsymbol{H}, J\}$ for large strain solid dynamics. Section 3 describes the computational methodology of the Upwind SPH framework. The variational statement of the $\{\boldsymbol{p}, \boldsymbol{F}, \boldsymbol{H}, J\}$ system, the SPH approximation, the Riemann solver based SPH discretisation and the linear reconstruction procedure are presented. For clarity, the complete explicit Upwind SPH algorithm is summarised in Section 4. In addition, an artificial compressibility algorithm is also presented in Section 5 to account for truly and nearly incompressible solids. Section 6 summarises the flowchart of the proposed SPH methodology. In Section 7, an extensive set of challenging numerical examples is examined to assess the performance of the proposed algorithm. Finally, Section 8 presents some concluding remarks and current directions of research.

2. Reversible elastodynamics

Consider the three dimensional deformation of an isothermal body of material density ρ_0 moving from its initial undeformed configuration occupying a volume V, of boundary ∂V, to

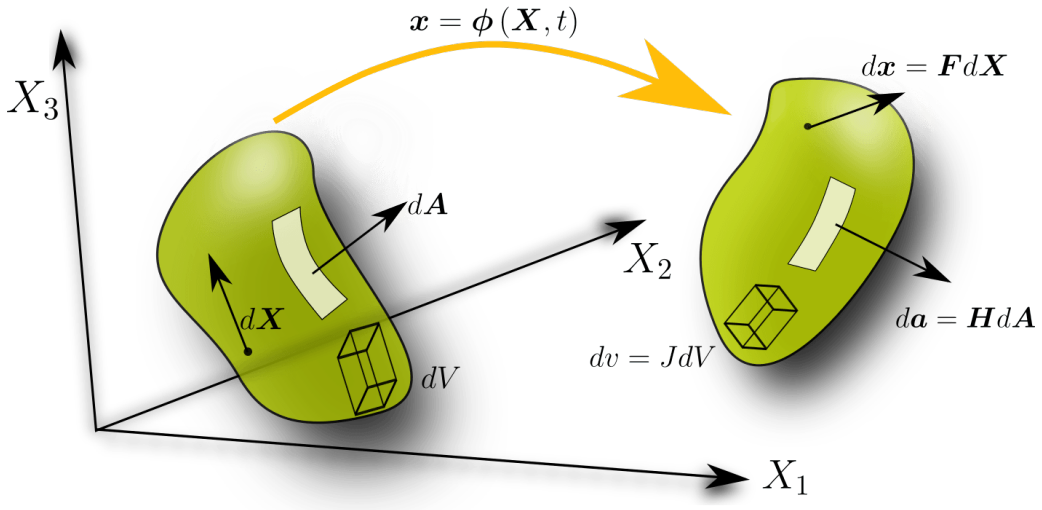

Figure 1: Motion of a deformable continuum domain

a current deformed configuration at time t occupying a volume v, of boundary ∂v (see Figure 1). The time dependent motion is defined through a deformation mapping $\boldsymbol{x} = \boldsymbol{\phi}(\boldsymbol{X}, t)$ which satisfies the following set of Total Lagrangian first order conservation laws [1, 2, 27, 34–38]

$$\frac{\partial \boldsymbol{p}}{\partial t} - \text{DIV}\, \boldsymbol{P} = \boldsymbol{f}_0; \tag{1a}$$

$$\frac{\partial \boldsymbol{F}}{\partial t} - \boldsymbol{\nabla}_0 \left(\frac{\boldsymbol{p}}{\rho_0} \right) = \boldsymbol{0}; \tag{1b}$$

$$\frac{\partial \boldsymbol{H}}{\partial t} - \text{CURL} \left(\frac{\boldsymbol{p}}{\rho_0} \times \boldsymbol{F} \right) = \boldsymbol{0}; \tag{1c}$$

$$\frac{\partial J}{\partial t} - \text{DIV} \left(\frac{1}{\rho_0} \boldsymbol{H}^T \boldsymbol{p} \right) = 0. \tag{1d}$$

Here, $\boldsymbol{p} := \rho_0 \boldsymbol{v}$ is the linear momentum per unit of undeformed volume, $\boldsymbol{v}$ is the velocity field, $\boldsymbol{F}$ is the deformation gradient (or fibre map), $\boldsymbol{H}$ is the co-factor of the deformation (or area map), J is the Jacobian of the deformation (or volume map), $\boldsymbol{P}$ is the first Piola-Kirchhoff stress tensor and $\boldsymbol{f}_0$ is a body force term per unit of undeformed volume. The symbol $\times$ represents the tensor cross product between vectors and/or second order tensors in the sense of [25, 30, 39, 40], DIV and CURL represent the material divergence and material curl operators as defined in expressions (5) and (7) of Reference [25], respectively, and $\boldsymbol{\nabla}_0$ represents the material gradient operator defined as $\boldsymbol{\nabla}_0 := \frac{\partial}{\partial \boldsymbol{X}}$.

Above equation (1a) represents the conservation of linear momentum, whilst the rest of the system equations (1b-1d) represent a supplementary set of conservation laws for the geometric strain measures $\{\boldsymbol{F}, \boldsymbol{H}, J\}$. Additionally, appropriate involutions [1, 26] must be satisfied by some of the strain variables $\{\boldsymbol{F}, \boldsymbol{H}\}$ [41] of the system as

$$\text{CURL}\boldsymbol{F} = \boldsymbol{0}; \quad \text{DIV}\boldsymbol{H} = \boldsymbol{0}. \tag{2}$$

Notice that, if necessary, the use of these involutions enables the conservation equations for

the area and volume maps in (1c) and (1d) to be re-written as [1]

$$\frac{\partial \boldsymbol{H}}{\partial t} - \boldsymbol{F} \boldsymbol{\times} \boldsymbol{\nabla}_0 \left(\frac{\boldsymbol{p}}{\rho_0} \right) = \boldsymbol{0}; \quad \frac{\partial J}{\partial t} - \boldsymbol{H} : \boldsymbol{\nabla}_0 \left(\frac{\boldsymbol{p}}{\rho_0} \right) = 0. \tag{3}$$

More generally, the above system of conservation laws (1) can be summarised in a concise manner as

$$\frac{\partial \boldsymbol{\mathcal{U}}}{\partial t} + \frac{\partial \boldsymbol{\mathcal{F}}_I}{\partial X_I} = \boldsymbol{\mathcal{S}}; \quad \forall I = 1, 2, 3, \tag{4}$$

where $\boldsymbol{\mathcal{U}}$ denotes the set of conservation variables, $\boldsymbol{\mathcal{S}}$ the source term and $\boldsymbol{\mathcal{F}}_I$ the flux vector in the material Cartesian direction I, as follows

$$\boldsymbol{\mathcal{U}} = \begin{bmatrix} \boldsymbol{p} \\ \boldsymbol{F} \\ \boldsymbol{H} \\ J \end{bmatrix}; \qquad \boldsymbol{\mathcal{F}}_I = - \begin{bmatrix} \boldsymbol{P}\boldsymbol{E}_I \\ \frac{1}{\rho_0} \boldsymbol{p} \otimes \boldsymbol{E}_I \\ \boldsymbol{F} \boldsymbol{\times} \left(\frac{1}{\rho_0} \boldsymbol{p} \otimes \boldsymbol{E}_I \right) \\ \boldsymbol{H} : \left(\frac{1}{\rho_0} \boldsymbol{p} \otimes \boldsymbol{E}_I \right) \end{bmatrix}; \qquad \boldsymbol{\mathcal{S}} = \begin{bmatrix} \boldsymbol{f}_0 \\ \boldsymbol{0} \\ \boldsymbol{0} \\ 0 \end{bmatrix}, \tag{5}$$

with $\boldsymbol{E}_I$ is the I-th unit vector of the Cartesian basis defined as

$$\boldsymbol{E}_1 = \begin{bmatrix} 1 \\ 0 \\ 0 \end{bmatrix}; \qquad \boldsymbol{E}_2 = \begin{bmatrix} 0 \\ 1 \\ 0 \end{bmatrix}; \qquad \boldsymbol{E}_3 = \begin{bmatrix} 0 \\ 0 \\ 1 \end{bmatrix}. \tag{6}$$

Furthermore, the corresponding flux vector (5b) associated with the material unit outward normal $\boldsymbol{N}$ can be expressed as

$$\boldsymbol{\mathcal{F}}_{\boldsymbol{N}} = \boldsymbol{\mathcal{F}}_I N_I = - \begin{bmatrix} \boldsymbol{P}\boldsymbol{N} \\ \frac{1}{\rho_0} \boldsymbol{p} \otimes \boldsymbol{N} \\ \boldsymbol{F} \boldsymbol{\times} \left(\frac{1}{\rho_0} \boldsymbol{p} \otimes \boldsymbol{N} \right) \\ \boldsymbol{H} : \left(\frac{1}{\rho_0} \boldsymbol{p} \otimes \boldsymbol{N} \right) \end{bmatrix}. \tag{7}$$

Crucially, in the presence of non-smooth solutions, all of the above conservation laws (1a-1d) are accompanied by appropriate jump conditions [34, 42] defined as

$$c \, [\![\boldsymbol{p}]\!] = - [\![\boldsymbol{P}]\!] \boldsymbol{N}; \tag{8a}$$

$$c \, [\![\boldsymbol{F}]\!] = - \frac{1}{\rho_0} [\![\boldsymbol{p}]\!] \otimes \boldsymbol{N}; \tag{8b}$$

$$c \, [\![\boldsymbol{H}]\!] = - \boldsymbol{F}^{\mathrm{Ave}} \boldsymbol{\times} \left(\frac{1}{\rho_0} [\![\boldsymbol{p}]\!] \otimes \boldsymbol{N} \right); \tag{8c}$$

$$c \, [\![J]\!] = - \boldsymbol{H}^{\mathrm{Ave}} : \left(\frac{1}{\rho_0} [\![\boldsymbol{p}]\!] \otimes \boldsymbol{N} \right), \tag{8d}$$

where $[\![\cdot]\!]$ denotes the jump operator across a discontinuity surface with normal $\boldsymbol{N}$ moving with speed c in the reference space and $\{ \boldsymbol{F}^{\mathrm{Ave}}, \boldsymbol{H}^{\mathrm{Ave}} \}$ being defined as an average of the geometric strain measures between the left and right states of a discontinuity surface.

For the particular case of a reversible process, the closure of the system described in (1) requires the introduction of a suitable constitutive law relating the stress tensor $\boldsymbol{P}$ with the

strain measures $\{\boldsymbol{F}, \boldsymbol{H}, J\}$, obeying the principle of objectivity [43] and thermodynamic consistency (via the Colemann-Noll procedure) [44]. In this work, a polyconvex nearly incompressible constitutive model is used (see Section 2.1 of Reference [1] on pg. 75). Taking advantage of the complete set of conservation laws described in (1), the polyconvex nature of the constitutive model (i.e. a guarantor of material stability [45, 46]) facilitates the transformation of the system of conservation laws into a symmetric set of hyperbolic equations expressed in terms of the entropy conjugates of the conservation variables [25, 30]. Finally, for the complete definition of the initial boundary value problem, initial and boundary (essential and natural) conditions must also be specified as appropriate.

Remark 1:

In the present manuscript, consideration of irreversible processes is restricted to the case of an isothermal elasto-plastic model typically used in metal forming applications [24]. Particularly, thermal effects will be neglected. In order to model irrecoverable plastic behaviour, the standard rate-independent von Mises plasticity model [43] with isotropic hardening is used and the basic structure is summarised for completeness in Appendix A.

---

3. Spatial discretisation

The set of local conservation equations described in (1a-1d) has recently been spatially discretised by the authors using two well-established (and consistent) stabilisation strategies, leading to the Jameson-Schmidt-Turkel Smooth Particle Hydrodynamics (JST-SPH) algorithm [1] and the Streamline Upwind Petrov-Galerkin Smooth Particle Hydrodynamics (SUPG-SPH) algorithm [2]. These numerical techniques resulted in being very efficient when attempting to solve problems with predominant nearly incompressible behaviour. JST-SPH requires the evaluation of a blend of Laplacian and bi-Laplacian operators for JST stabilisation and SUPG-SPH requires the generation of a secondary set of particles for the computation of a residual-based SUPG stabilisation. In this paper, we explore a third and extremely competitive stabilised SPH method. The new methodology is known as Upwind Smooth Particle Hydrodynamics (Upwind-SPH) and will be discussed in the following section.

3.1. General remark

In general, a standard weak variational statement for the mixed-based system $\{\boldsymbol{p}, \boldsymbol{F}, \boldsymbol{H}, J\}$ (1a-1d) (known as Bubnov-Galerkin contribution $\mathcal{A}_{\text{Gal}}$) is established by multiplying the local form of the conservation laws (4) by appropriate work conjugate virtual fields $\delta\boldsymbol{\mathcal{V}}$ and integrating over the volume V of the body, to give

$$0 = \mathcal{A}_{\text{Gal}}(\boldsymbol{\mathcal{U}}, \delta\boldsymbol{\mathcal{V}}) := \int_V \delta\boldsymbol{\mathcal{V}} \bullet \frac{\partial \boldsymbol{\mathcal{U}}}{\partial t}\, dV - \int_V \delta\boldsymbol{\mathcal{V}} \bullet \boldsymbol{\mathcal{S}}\, dV + \int_V \delta\boldsymbol{\mathcal{V}} \bullet \frac{\partial \boldsymbol{\mathcal{F}}_I}{\partial X_I}\, dV. \tag{9}$$

The symbol $\bullet$ is used to denote the inner (dual) product of work conjugate pairs, $\delta\boldsymbol{\mathcal{V}} := \{\delta\boldsymbol{v}, \delta\boldsymbol{\Sigma}_{\boldsymbol{F}}, \delta\boldsymbol{\Sigma}_{\boldsymbol{H}}, \delta\Sigma_J\}$ represent the virtual work conjugates of the conservation variables $\boldsymbol{\mathcal{U}}$, $\delta\boldsymbol{v}$ is the virtual velocity field and $\{\delta\boldsymbol{\Sigma}_{\boldsymbol{F}}, \delta\boldsymbol{\Sigma}_{\boldsymbol{H}}, \delta\Sigma_J\}$ are appropriate conjugate stresses to $\{\boldsymbol{F}, \boldsymbol{H}, J\}$ respectively.

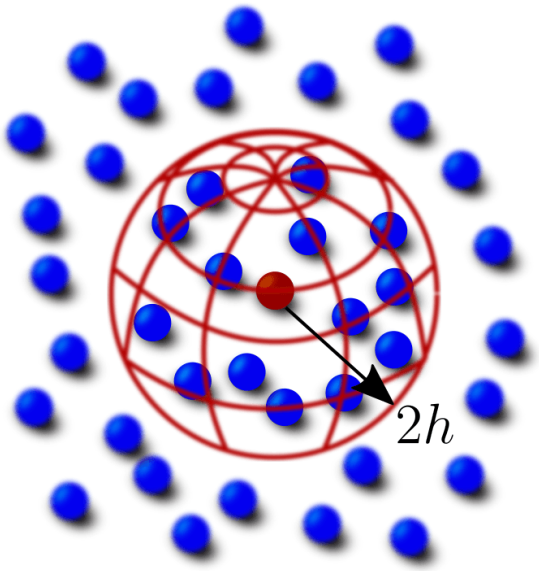

Figure 2: Particle approximation

Application of the Green-Gauss divergence theorem on the last term of (9) results in

$$0 = \mathcal{A}_{\text{Gal}}(\boldsymbol{\mathcal{U}}, \delta\boldsymbol{\mathcal{V}}) := \int_V \delta\boldsymbol{\mathcal{V}} \bullet \frac{\partial \boldsymbol{\mathcal{U}}}{\partial t}\, dV - \int_V \delta\boldsymbol{\mathcal{V}} \bullet \boldsymbol{\mathcal{S}}\, dV - \int_V \boldsymbol{\mathcal{F}}_I \bullet \frac{\partial \delta\boldsymbol{\mathcal{V}}}{\partial X_I}\, dV + \int_{\partial V} \delta\boldsymbol{\mathcal{V}} \bullet \boldsymbol{\mathcal{F}}_{\boldsymbol{\mathcal{N}}}\, dA. \quad (10)$$

Above Galerkin representation (10) can be particularised to the case of the linear momentum $\boldsymbol{p}$ and the extended set of geometric strain measures $\{\boldsymbol{F}, \boldsymbol{H}, J\}$

$$0 = \mathcal{A}^{\boldsymbol{p}}_{\text{Gal}} := \int_V \delta\boldsymbol{v} \cdot \frac{\partial \boldsymbol{p}}{\partial t}\, dV + \int_V \boldsymbol{P} : \boldsymbol{\nabla}_0 \delta\boldsymbol{v}\, dV - \int_V \delta\boldsymbol{v} \cdot \boldsymbol{f}_0\, dV - \int_{\partial V} \delta\boldsymbol{v} \cdot \boldsymbol{t}_B\, dA; \quad (11a)$$

$$0 = \mathcal{A}^{\boldsymbol{F}}_{\text{Gal}} := \int_V \delta\boldsymbol{\Sigma}_{\boldsymbol{F}} : \left[\frac{\partial \boldsymbol{F}}{\partial t} - \boldsymbol{\nabla}_0 \left(\frac{\boldsymbol{p}}{\rho_0}\right)\right] dV; \quad (11b)$$

$$0 = \mathcal{A}^{\boldsymbol{H}}_{\text{Gal}} := \int_V \delta\boldsymbol{\Sigma}_{\boldsymbol{H}} : \left[\frac{\partial \boldsymbol{H}}{\partial t} - \boldsymbol{F} \times \boldsymbol{\nabla}_0 \left(\frac{\boldsymbol{p}}{\rho_0}\right)\right] dV; \quad (11c)$$

$$0 = \mathcal{A}^{J}_{\text{Gal}} := \int_V \delta\Sigma_J \left[\frac{\partial J}{\partial t} - \boldsymbol{H} : \boldsymbol{\nabla}_0 \left(\frac{\boldsymbol{p}}{\rho_0}\right)\right] dV, \quad (11d)$$

with $\boldsymbol{t}_B$ being a possible boundary traction vector. Notice that only the linear momentum conservation equation (11a) has been integrated by parts in order to enable the imposition of boundary tractions.

3.2. Corrected SPH approximation

For evaluation of the material gradient of any arbitrary vector function $\boldsymbol{f}$, we employ the following particle approximation via the use of the "Corrected Gradient of a Corrected Kernel $\tilde{\boldsymbol{\nabla}}_0 \tilde{\mathrm{W}}$" [24, 47] described as follows

$$\boldsymbol{\nabla}_0 \boldsymbol{f}(\boldsymbol{X}_a) \approx \sum_{b \in \Lambda^b_a} \boldsymbol{f}_b \otimes \boldsymbol{G}_b(\boldsymbol{X}_a); \qquad \boldsymbol{G}_b(\boldsymbol{X}_a) := V_b \tilde{\boldsymbol{\nabla}}_0 \tilde{\mathrm{W}}_b(\boldsymbol{X}_a). \quad (12)$$

Here, Λ^b_a represents the set of neighbouring particles b that lie inside a sphere of a given radius $2h$ around $\boldsymbol{X}_a$ (see Figure 2), V_b and $\boldsymbol{f}_b$ represent the volume and time varying vector function $\boldsymbol{f}$

stored at particle b. The kernel approximation W being employed in this paper is the standard quadratic kernel function introduced in [48] (see equation (5) of Section 2.1 on pg. 350).

As shown in Reference [47] (see Section 4.3 on pg. 106-107), the above kernel gradient evaluation $\boldsymbol{G}_b(\boldsymbol{X}_a)$ reproduces exactly the gradient of any constant and/or linear function. For this reason, equation (12), if necessary, can also be alternatively expressed by including the redundant term $\boldsymbol{f}_a$ in (12) as

$$\boldsymbol{\nabla}_0 \boldsymbol{f}(\boldsymbol{X}_a) \approx \sum_{b \in \Lambda_a^b} 2 \left[\frac{1}{2} (\boldsymbol{f}_a + \boldsymbol{f}_b) \right] \otimes \boldsymbol{G}_b(\boldsymbol{X}_a). \tag{13}$$

Remark 2:

Another useful representation for the evaluation of a kernel gradient can be formulated by artificially adding the redundant term $-\boldsymbol{f}_a$ to (12), resulting in

$$\boldsymbol{\nabla}_0 \boldsymbol{f}(\boldsymbol{X}_a) \approx \sum_{b \in \Lambda_a^b} 2 \left[\frac{1}{2} (\boldsymbol{f}_b - \boldsymbol{f}_a) \right] \otimes \boldsymbol{G}_b(\boldsymbol{X}_a). \tag{14}$$

One of the key contributions of this paper is to show a relationship between the SPH particle approximation and the vertex centred Finite Volume Method (FVM) approximation [3], where the latter requires the definition of a dual mesh[3] which is constructed using the median dual approach [29]. This will enable a well-established upwinding finite volume spatial discretisation [49, 50] commonly used in the CFD community to be adapted to a SPH mesh-free method. To achieve this, we first recall the discrete gradient evaluation used within the control volume associated with node a by utilising a discrete version of the Green-Gauss divergence theorem

$$\boldsymbol{\nabla}_0 \boldsymbol{f}(\boldsymbol{X}_a) \approx \frac{1}{V_a} \int_{\partial V_a} \boldsymbol{f} \otimes \boldsymbol{N} dA, \tag{15}$$

with $\boldsymbol{N}$ being the outward unit normal vector on the boundary of the control volume ∂V_a. Above discrete boundary integral (15) can then be discretised by means of the FVM where a (second order) central difference approximation is used for the discretisation of the vector function $\boldsymbol{f}$, to give

$$\boldsymbol{\nabla}_0 \boldsymbol{f}(\boldsymbol{X}_a) \approx \frac{1}{V_a} \sum_{b \in \Lambda_a^b} \left[\frac{1}{2} (\boldsymbol{f}_a + \boldsymbol{f}_b) \right] \otimes \boldsymbol{C}_{ab}, \tag{16}$$

where for a given edge connecting nodes a and b (see Figure (3a)), the material area vector $\boldsymbol{C}_{ab}$ is defined as[4]

$$\boldsymbol{C}_{ab} := \sum_{k \in \Lambda_{ab}^k} \boldsymbol{N}_k A_k, \tag{17}$$

where Λ_{ab}^k is the set of facets belonging to edge ab, A_k is the area of a given facet k and $\boldsymbol{N}_k$ its outward normal. These material area vectors enable a substantial reduction in the computational cost when computing the boundary integral used in the Green-Gauss divergence theorem, since they save an additional loop on facets per edge ab [29, 38].

[3]The dual mesh is constructed by connecting edge midpoints with element centroids in two dimensions (see Figure 3a) and edge midpoints with face centroids and element centroids in three dimensions.

[4]Due to the definition of a dual mesh, the area vectors satisfy $\boldsymbol{C}_{ab}$ = -$\boldsymbol{C}_{ba}$.

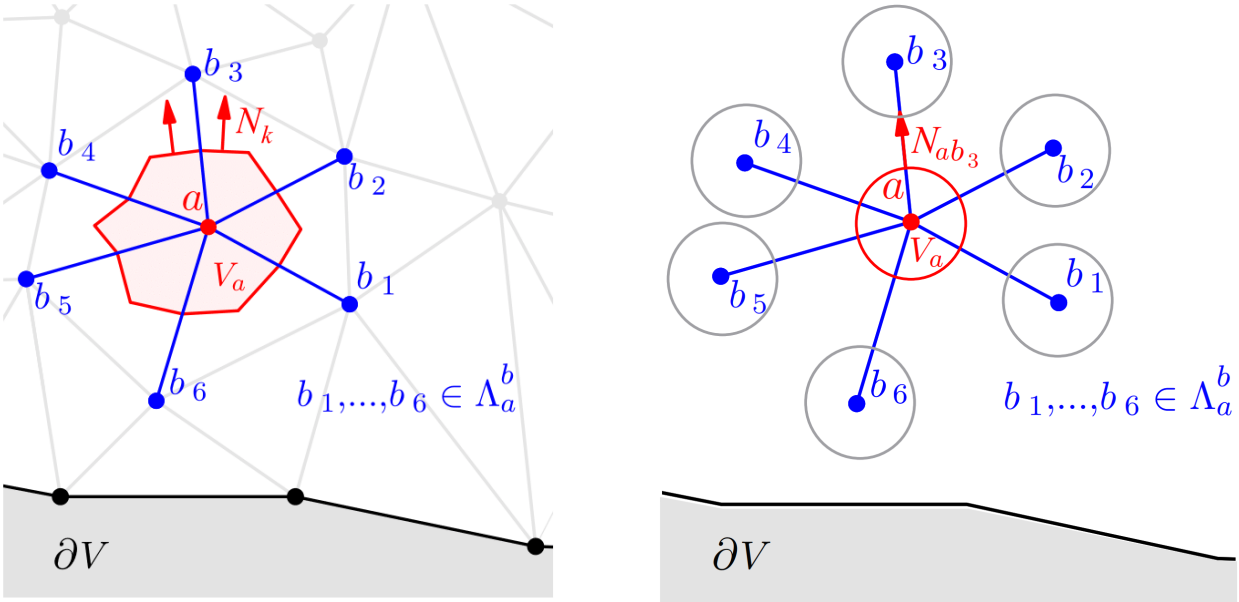

Figure 3: Control volume for (a) vertex centred FVM and (b) SPH mesh free approach in two dimensions. The red shaded area is the control volume associated to node a. The blue lines are the edges connecting node a to its neighbouring nodes b_i. The vertex centred FVM requires the outward unit normal $\boldsymbol{N}_{ab}$ to be defined using the material outward normal $\boldsymbol{N}_k$ of every facet k belonging to edge ab. However, for the SPH mesh free approach, the normal $\boldsymbol{N}_{ab}$ is defined by a direction vector between particles a and b.

Comparing equation (13) with (16), a useful relationship arises relating the (mesh-based) material outward area vector with the (mesh-free) SPH kernel gradient evaluation, defined as

$$\mathbf{C}_{ab} := 2V_a \boldsymbol{G}_b(\boldsymbol{X}_a). \tag{18}$$

Its reciprocal relationship can also be defined as $\mathbf{C}_{ba} := 2V_b \boldsymbol{G}_a(\boldsymbol{X}_b)$. Due to the anti-symmetric nature of the SPH gradient correction [7, 47], notice here that $\boldsymbol{G}_b(\boldsymbol{X}_a) \neq \boldsymbol{G}_a(\boldsymbol{X}_b)$ which in turn lead to $\mathbf{C}_{ab} \neq -\mathbf{C}_{ba}$.

3.3. SPH spatial discretisation

Typically, in the context of Element Free Galerkin schemes [51, 52], the Galerkin weak statements described in (11a-11d) are accurately evaluated using the necessary distribution of (Gauss) quadrature points in order to avoid spurious hourglass (or zero-energy) modes [12, 15, 53]. In general, the positions of these quadrature points do not coincide with those of the material particles [51, 54]. This is however not the case when employing a mesh-free SPH discretisation. In the latter case, above integrands (11a-11d) are under-integrated at the cloud of particles regarded as quadrature points [1, 4, 6, 8, 55, 56].

3.3.1. Bubnov-Galerkin contribution

Using a corrected kernel interpolation $\tilde{\mathrm{W}}$ (see Section 3.2 on pg. 77 in Reference [1]) along with the corresponding discrete gradient evaluation of $\boldsymbol{\nabla}_0 \delta\boldsymbol{v}$ described in (14), term $\mathcal{A}^{\boldsymbol{p}}_{\mathrm{Gal}}$ (11a) results in the following semi-discrete expression

$$\frac{d\boldsymbol{p}_a}{dt} = \boldsymbol{E}_a - \boldsymbol{T}_a. \tag{19a}$$

Here, the nodal external $\boldsymbol{E}_a$ and internal $\boldsymbol{T}_a$ force vectors are defined as

$$\boldsymbol{E}_a = \frac{A_a}{V_a}\boldsymbol{t}_B^a + \boldsymbol{f}_0^a; \qquad \boldsymbol{T}_a = \sum_{b\in\Lambda_a^b} 2V_b \left[\boldsymbol{P}_b \tilde{\boldsymbol{\nabla}}_0 \tilde{\mathrm{W}}_b(\boldsymbol{X}_a)\right]^{\mathrm{Ave}}, \tag{20}$$

where

$$\left[\boldsymbol{P}_b \tilde{\boldsymbol{\nabla}}_0 \tilde{\mathrm{W}}_b(\boldsymbol{X}_a)\right]^{\mathrm{Ave}} := \frac{1}{2}\left[\boldsymbol{P}_b \tilde{\boldsymbol{\nabla}}_0 \tilde{\mathrm{W}}_a(\boldsymbol{X}_b) - \boldsymbol{P}_a \tilde{\boldsymbol{\nabla}}_0 \tilde{\mathrm{W}}_b(\boldsymbol{X}_a)\right]. \tag{21}$$

Here, $\boldsymbol{P}_{a,b} := \boldsymbol{P}(\boldsymbol{F}_{a,b}, \boldsymbol{H}_{a,b}, J_{a,b})$. A_a and $\boldsymbol{t}_B^a$ are the tributary area and traction vector of those particles placed on the boundary, the latter being computed directly from the given traction boundary conditions [3, 34, 42]. The internal force representation $\boldsymbol{T}_a$ described in (20) satisfies the global conservation of linear momentum, that is $\sum_a V_a \boldsymbol{T}_a = \boldsymbol{0}$.

Analogously to the above discretisation procedure, the extended set of geometric conservation laws $\mathcal{A}_{\mathrm{Gal}}^{\boldsymbol{F},\boldsymbol{H},J}$ (11b-11d) can now follow, but this time using the gradient approximation of $\boldsymbol{\nabla}_0\left(\frac{\boldsymbol{p}}{\rho_0}\right)$ presented in (13). This will yield

$$\frac{d\boldsymbol{F}_a}{dt} = \sum_{b\in\Lambda_a^b} 2\left(\frac{\boldsymbol{p}^{\mathrm{Ave}}}{\rho_0}\right) \otimes \boldsymbol{G}_b(\boldsymbol{X}_a); \tag{22a}$$

$$\frac{d\boldsymbol{H}_a}{dt} = \boldsymbol{F}_a \boldsymbol{\times} \sum_{b\in\Lambda_a^b} 2\left(\frac{\boldsymbol{p}^{\mathrm{Ave}}}{\rho_0}\right) \otimes \boldsymbol{G}_b(\boldsymbol{X}_a); \tag{22b}$$

$$\frac{dJ_a}{dt} = \boldsymbol{H}_a : \sum_{b\in\Lambda_a^b} 2\left(\frac{\boldsymbol{p}^{\mathrm{Ave}}}{\rho_0}\right) \otimes \boldsymbol{G}_b(\boldsymbol{X}_a), \tag{22c}$$

where the average linear momentum $\boldsymbol{p}^{\mathrm{Ave}} := \frac{1}{2}(\boldsymbol{p}_a + \boldsymbol{p}_b)$.

Remark 3: It is easy to show that the vertex-centred FVM presented in Reference [3] is a particular case of the above representation (19a, 22a-22c). To show this, we utilise the relationship described in (18) and replacing the kernel gradient $\boldsymbol{G}_b(\boldsymbol{X}_a)$ in (19a, 22a-22c) with the material area vector $\mathbf{C}_{ab}$, which gives

$$\frac{d\boldsymbol{p}_a}{dt} = \frac{1}{V_a}\boldsymbol{E}_a - \frac{1}{V_a}\sum_{b\in\Lambda_a^b} \left[\boldsymbol{P}_b \mathbf{C}_{ab}\right]^{\mathrm{Ave}}; \tag{23a}$$

$$\frac{d\boldsymbol{F}_a}{dt} = \frac{1}{V_a}\sum_{b\in\Lambda_a^b} \left(\frac{\boldsymbol{p}^{\mathrm{Ave}}}{\rho_0}\right) \otimes \mathbf{C}_{ab}; \tag{23b}$$

$$\frac{d\boldsymbol{H}_a}{dt} = \frac{1}{V_a}\boldsymbol{F}_a \boldsymbol{\times} \sum_{b\in\Lambda_a^b} \left(\frac{\boldsymbol{p}^{\mathrm{Ave}}}{\rho_0}\right) \otimes \mathbf{C}_{ab}; \tag{23c}$$

$$\frac{dJ_a}{dt} = \frac{1}{V_a}\boldsymbol{H}_a : \sum_{b\in\Lambda_a^b} \left(\frac{\boldsymbol{p}^{\mathrm{Ave}}}{\rho_0}\right) \otimes \mathbf{C}_{ab}; \tag{23d}$$

with $\left[\boldsymbol{P}_b \mathbf{C}_{ab}\right]^{\mathrm{Ave}} := \frac{1}{2}\left[\boldsymbol{P}_b \mathbf{C}_{ba} - \boldsymbol{P}_a \mathbf{C}_{ab}\right]$. However, for the case of the dual mesh used in FVM, the area vectors become $\mathbf{C}_{ab} = \boldsymbol{C}_{ab}$, and thus satisfying $\boldsymbol{C}_{ba} = -\boldsymbol{C}_{ab}$. As a result, the linear momentum evolution (23a) reduces to the following expression

$$\frac{d\boldsymbol{p}_a}{dt} = \frac{1}{V_a}\boldsymbol{E}_a + \frac{1}{V_a}\sum_{b\in\Lambda_a^b} \boldsymbol{P}^{\mathrm{Ave}} \boldsymbol{C}_{ab}; \qquad \boldsymbol{P}^{\mathrm{Ave}} = \frac{1}{2}\left(\boldsymbol{P}_a + \boldsymbol{P}_b\right), \tag{24}$$

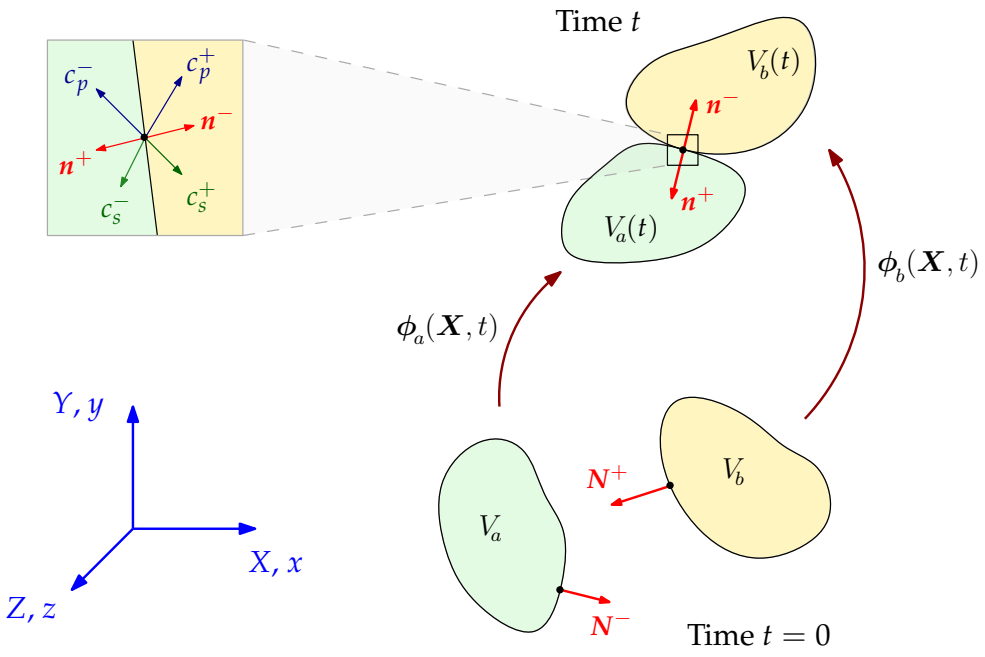

Figure 4: Contact mechanics

and the rest of the evolution equations for the geometric strain measures (23b-23d) remain exactly the same but replacing $\mathbf{C}_{ab}$ with $\boldsymbol{C}_{ab}$. Notice that expressions (24, 23b-23d) are exactly the semi-discrete equations presented for a vertex centred FVM [3].

However, the resulting spatially discretised systems, either the SPH discretisation described in (19a, 22a-22c) or the FVM discretisation in (24, 23b-23d), suffer from severe numerical instabilities (e.g. hour-glassing, pressure and tensile instabilities) [12, 18, 24, 57] and require some form of numerical dissipation [3, 25–27, 30, 34, 35, 38, 42]. In this work, an adapted (particle) Riemann-based upwinding stabilisation strategy is introduced to circumvent this shortcoming. This will be presented in the next section.

3.3.2. Riemann-based upwinding stabilisation

By taking advantage of the conservation structure of the mixed-based set of equations (1a-1d), numerical stabilisation is introduced via a characteristic-based Riemann solver previously explored in the context of finite volume methods [3, 34, 42]. In what follows, some of the results presented in Reference [42] (see Section 4.3 on pages. 417-420) will be employed.

In Lagrangian dynamics, it is often possible for two domains apart (i.e. V_a and V_b) to come into contact with each other after some time t. The impact would generate two types of shock waves (p-wave c_p and s-wave c_s) travelling within the domains, as illustrated in Figure 4. Similar waves propagate in the fictitious interface between neighbouring particles when considering piecewise discontinuous solutions.

Referring to Section 4.3 of [42], the numerical (interface) fluxes $\boldsymbol{\mathcal{F}}^{C}_{\boldsymbol{N}_{ab}}$ across a discontinuity

surface defined by the outward unit normal vector $\boldsymbol{N}_{ab}$ can be read as follows

$$\boldsymbol{\mathcal{F}}^{C}_{\boldsymbol{N}_{ab}} := -\begin{bmatrix} \boldsymbol{P}^{C}\boldsymbol{N}_{ab} \\ \frac{1}{\rho_0}\boldsymbol{p}^{C}\otimes\boldsymbol{N}_{ab} \\ \boldsymbol{F}_a \times \left(\frac{1}{\rho_0}\boldsymbol{p}^{C}\otimes\boldsymbol{N}_{ab}\right) \\ \boldsymbol{H}_a : \left(\frac{1}{\rho_0}\boldsymbol{p}^{C}\otimes\boldsymbol{N}_{ab}\right) \end{bmatrix}. \tag{25}$$

These numerical fluxes can be additively decomposed into the summation of an average state and an upwinding numerical stabilisation term, expressed as $[\cdot]^{C} := [\cdot]^{\text{Ave}} + [\cdot]^{\text{stab}}$.

In order to ensure the discrete satisfaction of the involutions described by equation (2), we must not introduce any numerical dissipation into (25b) and (25c) by setting the values of $\boldsymbol{p}^{C} = \boldsymbol{p}^{\text{Ave}}$. This implies that the update for $\{\boldsymbol{F}, \boldsymbol{H}\}$ are naturally curl- and divergence-free as their semi-discrete equations are formulated in terms of a material discrete gradient of a continuous velocity field [3, 30, 38]. As a result, above flux approximations (25) now reduce to

$$\boldsymbol{\mathcal{F}}^{C}_{\boldsymbol{N}_{ab}} = \underbrace{-\begin{bmatrix} \boldsymbol{P}^{\text{Ave}}\boldsymbol{N}_{ab} \\ \frac{1}{\rho_0}\boldsymbol{p}^{\text{Ave}}\otimes\boldsymbol{N}_{ab} \\ \boldsymbol{F}_a \times \left(\frac{1}{\rho_0}\boldsymbol{p}^{\text{Ave}}\otimes\boldsymbol{N}_{ab}\right) \\ \boldsymbol{H}_a : \left(\frac{1}{\rho_0}\boldsymbol{p}^{\text{Ave}}\otimes\boldsymbol{N}_{ab}\right) \end{bmatrix}}_{\text{Average}} \underbrace{-\begin{bmatrix} \boldsymbol{P}^{\text{stab}}\boldsymbol{N}_{ab} \\ \boldsymbol{0} \\ \boldsymbol{0} \\ \boldsymbol{H}_a : \left(\frac{1}{\rho_0}\boldsymbol{p}^{\text{stab}}\otimes\boldsymbol{N}_{ab}\right) \end{bmatrix}}_{\text{Upwinding stabilisation}}. \tag{26}$$

The first term on the right hand side of (26) represents the average (Galerkin) state, whereas the second term (being high order corrections) can be interpreted as an upwinding numerical stabilisation that damps the possible instabilities arising from the first term [34]. A detailed derivation of the upwinding stabilisation term described in (26) can be found in Reference [42].

For completeness, the expressions for the stabilised first Piola Kirchhoff stresses and linear momentum are [42]

$$\boldsymbol{P}^{\text{stab}} := \boldsymbol{S}^{\boldsymbol{p}}_{ab}\left[\left(\boldsymbol{p}^{+}_{f} - \boldsymbol{p}^{-}_{f}\right)\otimes\boldsymbol{N}_{ab}\right]; \quad \boldsymbol{p}^{\text{stab}} := \boldsymbol{S}^{\boldsymbol{P}}_{ab}\left[\left(\boldsymbol{P}^{+}_{f} - \boldsymbol{P}^{-}_{f}\right)\boldsymbol{N}_{ab}\right], \tag{27}$$

with the (acoustic) stabilisation matrices $\{\boldsymbol{S}^{\boldsymbol{p}}_{ab}, \boldsymbol{S}^{\boldsymbol{P}}_{ab}\}$ being defined as

$$\boldsymbol{S}^{\boldsymbol{p}}_{ab} = \frac{1}{2}\left[c_p\left(\boldsymbol{n}_{ab}\otimes\boldsymbol{n}_{ab}\right) + c_s\left(\boldsymbol{I} - \boldsymbol{n}_{ab}\otimes\boldsymbol{n}_{ab}\right)\right]; \qquad \boldsymbol{S}^{\boldsymbol{P}}_{ab} = \frac{1}{2c_p}\left(\boldsymbol{n}_{ab}\otimes\boldsymbol{n}_{ab}\right). \tag{28}$$

Here, the outward spatial normal is defined by the current direction vector between particles a and b such as $\boldsymbol{n}_{ab} := \frac{\boldsymbol{x}_b - \boldsymbol{x}_a}{\|\boldsymbol{x}_b - \boldsymbol{x}_a\|}$ and $\{\boldsymbol{p}^{-,+}_{f}, \boldsymbol{P}^{-,+}_{f}\}$ denote the left and right states of $\{\boldsymbol{p}, \boldsymbol{P}\}$ at fictitious interface f. The procedure of evaluating the reconstructed states $\{\boldsymbol{p}^{-,+}_{f}, \boldsymbol{P}^{-,+}_{f}\}$ will be discussed in Section 3.3.3.

It is now possible to introduce Riemann based stabilisation terms to the Galerkin contributions described in (24) and (23d). To achieve this, we need to replace $\{\boldsymbol{P}^{\text{Ave}}, \boldsymbol{p}^{\text{Ave}}\}$ of (24) and (23d) with $\{\boldsymbol{P}^{C}, \boldsymbol{p}^{C}\}$ via (26), and after some simple algebraic manipulation gives

$$\frac{d\boldsymbol{p}_a}{dt} = \left[\frac{1}{V_a}\boldsymbol{E}_a + \frac{1}{V_a}\sum_{b\in\Lambda^{b}_{a}}\frac{1}{2}\left(\boldsymbol{P}_b\mathbf{C}_{ba} - \boldsymbol{P}_a\mathbf{C}_{ab}\right)\right] + \boldsymbol{\mathcal{D}}(\boldsymbol{p}_a); \tag{29a}$$

$$\frac{dJ_a}{dt} = \left[\frac{1}{V_a}\boldsymbol{H}_a : \sum_{b\in\Lambda^{b}_{a}}\left(\frac{\boldsymbol{p}^{\text{Ave}}}{\rho_0}\right)\otimes\mathbf{C}_{ab}\right] + \mathcal{D}(J_a), \tag{29b}$$

where the Riemann based dissipative terms are

$$\boldsymbol{\mathcal{D}}(\boldsymbol{p}_a) = \frac{1}{V_a}\sum_{b\in\Lambda_a^b} \boldsymbol{P}^{\text{stab}}\mathbf{C}_{ab}; \quad \mathcal{D}(J_a) = \frac{1}{V_a}\sum_{b\in\Lambda_a^b} \frac{1}{\rho_0}\boldsymbol{p}^{\text{stab}}\cdot[\boldsymbol{H}_a\mathbf{C}_{ab}]\,. \tag{30}$$

Substitution of the fundamental relation (18) described by $\mathbf{C}_{ab} = 2V_a\boldsymbol{G}_b(\boldsymbol{X}_a)$ (and its reciprocal relation $\mathbf{C}_{ba} = 2V_b\boldsymbol{G}_a(\boldsymbol{X}_b)$) into (29) and (30), the squared bracket terms in (29a,b) recover the Galerkin discrete expressions for the conservation equations of linear momentum (19a) and Jacobian (22c), whereas the particle upwinding stabilisation terms can be found as

$$\boldsymbol{\mathcal{D}}(\boldsymbol{p}_a) = \sum_{b\in\Lambda_a^b} 2V_b\boldsymbol{P}^{\text{stab}}\tilde{\boldsymbol{\nabla}}_0\tilde{\mathrm{W}}_b(\boldsymbol{X}_a); \qquad \mathcal{D}(J_a) = \sum_{b\in\Lambda_a^b} 2V_b\frac{\boldsymbol{p}^{\text{stab}}}{\rho_0}\cdot\left[\boldsymbol{H}_a\tilde{\boldsymbol{\nabla}}_0\tilde{\mathrm{W}}_b(\boldsymbol{X}_a)\right]. \tag{31}$$

Since in this case $\tilde{\boldsymbol{\nabla}}_0\tilde{\mathrm{W}}_b(\boldsymbol{X}_a) \neq \tilde{\boldsymbol{\nabla}}_0\tilde{\mathrm{W}}_a(\boldsymbol{X}_b)$, the dissipation term $\boldsymbol{\mathcal{D}}(\boldsymbol{p}_a)$ presented in (31a) will not automatically satisfy the global conservation requirement [47]. However, this can be easily fulfilled by replacing $\tilde{\boldsymbol{\nabla}}_0\tilde{\mathrm{W}}_b(\boldsymbol{X}_a)$ with its average counterpart $\tilde{\boldsymbol{\nabla}}_0\tilde{\mathrm{W}}_b^{\text{Ave}}(\boldsymbol{X}_a)$ defined as

$$\tilde{\boldsymbol{\nabla}}_0\tilde{\mathrm{W}}_b^{\text{Ave}}(\boldsymbol{X}_a) := \frac{1}{2}\left[\tilde{\boldsymbol{\nabla}}_0\tilde{\mathrm{W}}_b(\boldsymbol{X}_a) - \tilde{\boldsymbol{\nabla}}_0\tilde{\mathrm{W}}_a(\boldsymbol{X}_b)\right]. \tag{32}$$

Similarly, in order to ensure the stabilisation term $\mathcal{D}(J_a)$ is globally conservative, the term $\left[\boldsymbol{H}_a\tilde{\boldsymbol{\nabla}}_0\tilde{\mathrm{W}}_b(\boldsymbol{X}_a)\right]$ presented in (31b) must also be replaced by $\left[\boldsymbol{H}_a\tilde{\boldsymbol{\nabla}}_0\tilde{\mathrm{W}}_b(\boldsymbol{X}_a)\right]^{\text{Ave}}$ defined by

$$\left[\boldsymbol{H}_a\tilde{\boldsymbol{\nabla}}_0\tilde{\mathrm{W}}_b(\boldsymbol{X}_a)\right]^{\text{Ave}} := \frac{1}{2}\left[\boldsymbol{H}_b\tilde{\boldsymbol{\nabla}}_0\tilde{\mathrm{W}}_a(\boldsymbol{X}_b) - \boldsymbol{H}_a\tilde{\boldsymbol{\nabla}}_0\tilde{\mathrm{W}}_b(\boldsymbol{X}_a)\right]. \tag{33}$$

3.3.3. Linear reconstruction procedure

In order to guarantee second order accuracy in space, a linear reconstruction procedure [34] is employed for the evaluation of the neighbouring states of the Riemann values, that is $\{\boldsymbol{p}_f^{-,+}, \boldsymbol{P}_f^{-,+}\}$.

The reconstruction procedure can be achieved using two different strategies. The first standard approach is to reconstruct both the linear momentum and the deformation gradient tensor (e.g. $\{\boldsymbol{p}_f^-, \boldsymbol{F}_f^-\}$ and $\{\boldsymbol{p}_f^+, \boldsymbol{F}_f^+\}$) at the mid-edge f connecting particles a and b, followed by the computation of the corresponding stresses $\{\boldsymbol{P}(\boldsymbol{F}_f^-), \boldsymbol{P}(\boldsymbol{F}_f^+)\}$. The second strategy is to first compute the stresses at each particle (i.e. $\boldsymbol{P}(\boldsymbol{F}_a)$ and $\boldsymbol{P}(\boldsymbol{F}_b)$) and then reconstruct the computed stresses to the interface f, namely $\{\boldsymbol{P}_f^-, \boldsymbol{P}_f^+\}$. The latter is of particular interest in this paper since it requires fewer evaluations of the stresses and, as complex constitutive models are typically used in solid mechanics, this can result in a faster algorithm.

For any individual component $\mathcal{U}$ of the variables $\boldsymbol{p}$ and $\boldsymbol{P}$, the linear reconstructed value at any position $\boldsymbol{X}$ is in the form of

$$\mathcal{U}(\boldsymbol{X}) = \mathcal{U}_a + \boldsymbol{\mathcal{G}}_a\cdot(\boldsymbol{X} - \boldsymbol{X}_a). \tag{34}$$

To achieve this, it is necessary to obtain an appropriate (particle) gradient operator $\boldsymbol{\mathcal{G}}_a$ through the least squares minimisation process [34, 42].

Introducing first the objective functional Π given as

$$\Pi(\boldsymbol{\mathcal{G}}_a) = \frac{1}{2}\sum_{b\in\Lambda_a^b}\frac{1}{\|\boldsymbol{d}_{ab}\|^2}\left[\mathcal{U}_b - (\mathcal{U}_a + \boldsymbol{\mathcal{G}}_a\cdot\boldsymbol{d}_{ab})\right]^2; \quad \boldsymbol{d}_{ab} = \boldsymbol{X}_b - \boldsymbol{X}_a. \tag{35}$$

Here, $b \in \Lambda_a^b$ represents a set of neighbouring (particle) values b associated with particle a, and $\boldsymbol{d}_{ab}$ represents a material vector measured from position a to b. Taking directional derivative of (35) with respect to $\boldsymbol{\mathcal{G}}_a$, yields

$$\boldsymbol{0} = D\Pi[\boldsymbol{\mathcal{G}}_a] = \sum_{b \in \Lambda_a^b} \frac{1}{\|\boldsymbol{d}_{ab}\|^2} \left[\mathcal{U}_b - (\mathcal{U}_a + \boldsymbol{\mathcal{G}}_a \cdot \boldsymbol{d}_{ab})\right] \boldsymbol{d}_{ab}. \tag{36}$$

Rearranging equation (36) gives the following expression for $\boldsymbol{\mathcal{G}}_a$

$$\boldsymbol{\mathcal{G}}_a = \left[\sum_{b \in \Lambda_a^b} \boldsymbol{N}_{ab} \otimes \boldsymbol{N}_{ab}\right]^{-1} \sum_{b \in \Lambda_a^b} \left(\frac{\mathcal{U}_b - \mathcal{U}_a}{\|\boldsymbol{d}_{ab}\|}\right) \boldsymbol{N}_{ab}, \tag{37}$$

where $\boldsymbol{N}_{ab}$ is the unit vector in the direction of $\boldsymbol{d}_{ab}$ described in (C.3) (see Figure 3b).

4. Complete Upwind-SPH algorithm

Addition of the discrete upwinding stabilisation terms (31) to the Bubnov-Galerkin discrete expressions (see (19a) and (22a-22c)), finally yields the complete semi-discrete set of governing equations for $\{\boldsymbol{p}, \boldsymbol{F}, \boldsymbol{H}, J\}$ as

$$\frac{d\boldsymbol{p}_a}{dt} = \boldsymbol{E}_a - \boldsymbol{T}_a + \boldsymbol{\mathcal{D}}(\boldsymbol{p}_a); \tag{38a}$$

$$\frac{d\boldsymbol{F}_a}{dt} = \sum_{b \in \Lambda_a^b} 2 \left(\frac{\boldsymbol{p}^{\mathrm{Ave}}}{\rho_0}\right) \otimes \boldsymbol{G}_b(\boldsymbol{X}_a); \tag{38b}$$

$$\frac{d\boldsymbol{H}_a}{dt} = \boldsymbol{F}_a \times \sum_{b \in \Lambda_a^b} 2 \left(\frac{\boldsymbol{p}^{\mathrm{Ave}}}{\rho_0}\right) \otimes \boldsymbol{G}_b(\boldsymbol{X}_a); \tag{38c}$$

$$\frac{dJ_a}{dt} = \boldsymbol{H}_a : \sum_{b \in \Lambda_a^b} 2 \left(\frac{\boldsymbol{p}^{\mathrm{Ave}}}{\rho_0}\right) \otimes \boldsymbol{G}_b(\boldsymbol{X}_a) + \mathcal{D}(J_a). \tag{38d}$$

The Riemann-based stabilising terms $\{\boldsymbol{\mathcal{D}}(\boldsymbol{p}_a), \mathcal{D}(J_a)\}$ and the internal $\boldsymbol{T}_a$ and external $\boldsymbol{E}_a$ force vectors are already defined in Section 3.3. Notice here that the upwinding stabilisation is only applied to the linear momentum evolution $\boldsymbol{\mathcal{D}}(\boldsymbol{p}_a)$ (38a) and the volume map evolution $\mathcal{D}(J_a)$ (38d). The former alleviates the appearance of spurious zero-energy (hourglass-like [8]) modes due to rank deficiency inherent to the use of Galerkin particle integration, whereas the latter removes pressure instabilities in near incompressibility [26].

Remark 4:

Alternatively, it is also possible to show that the (particle) discrete system (38a-38d) can

be re-written as

$$\frac{d\boldsymbol{p}_a}{dt} = \boldsymbol{E}_a - \sum_{b\in\Lambda_a^b} \frac{V_b}{V_a}\boldsymbol{P}_b\boldsymbol{G}_a(\boldsymbol{X}_b) + \boldsymbol{\mathcal{D}}(\boldsymbol{p}_a); \tag{39a}$$

$$\frac{d\boldsymbol{F}_a}{dt} = \sum_{b\in\Lambda_a^b} \frac{\boldsymbol{p}_b}{\rho_0} \otimes \boldsymbol{G}_b(\boldsymbol{X}_a); \tag{39b}$$

$$\frac{d\boldsymbol{H}_a}{dt} = \boldsymbol{F}_a \times \sum_{b\in\Lambda_a^b} \frac{\boldsymbol{p}_b}{\rho_0} \otimes \boldsymbol{G}_b(\boldsymbol{X}_a); \tag{39c}$$

$$\frac{dJ_a}{dt} = \boldsymbol{H}_a : \sum_{b\in\Lambda_a^b} \frac{\boldsymbol{p}_b}{\rho_0} \otimes \boldsymbol{G}_b(\boldsymbol{X}_a) + \mathcal{D}(J_a). \tag{39d}$$

Insofar as the mixed-based system $\{\boldsymbol{p}, \boldsymbol{F}, \boldsymbol{H}, J\}$, either (38) or (39), is rather large, it will only be suitable to employ an explicit type of time integrator. For simplicity, an explicit one-step two-stage Total Variation Diminishing Runge-Kutta (TVD-RK) scheme has been used [1–3, 25–27, 34, 38, 42]. This is described by the following time update equations from time step t^n to t^{n+1}:

$$\begin{aligned} \boldsymbol{\mathcal{U}}_a^\star &= \boldsymbol{\mathcal{U}}_a^n + \Delta t\, \dot{\boldsymbol{\mathcal{U}}}_a^n(\boldsymbol{\mathcal{U}}_a^n, t^n); \\ \boldsymbol{\mathcal{U}}_a^{\star\star} &= \boldsymbol{\mathcal{U}}_a^\star + \Delta t\, \dot{\boldsymbol{\mathcal{U}}}_a^\star(\boldsymbol{\mathcal{U}}_a^\star, t^{n+1}); \\ \boldsymbol{\mathcal{U}}_a^{n+1} &= \frac{1}{2}(\boldsymbol{\mathcal{U}}_a^n + \boldsymbol{\mathcal{U}}_a^{\star\star}). \end{aligned} \tag{40}$$

In this manuscript, the geometry is also updated through the above TVD-RK algorithm [1, 2, 42]. This results in a monolithic time integration procedure where the unknowns $\boldsymbol{\mathcal{U}} = (\boldsymbol{p}, \boldsymbol{F}, \boldsymbol{H}, J,)^T$ along with the geometry $\boldsymbol{x}$ are all updated via (40).

The maximum time step $\Delta t := t^{n+1} - t^n$ is governed by a standard Courant-Friedrichs-Lewy (CFL) condition [28] given as

$$\Delta t = \alpha_{CFL} \frac{h_{min}}{c_{p,max}}, \tag{41}$$

where $c_{p,max}$ is the maximum p-wave speed, h_{min} is the characteristic particle spacing within the computational domain and α_{CFL} is the CFL stability number. For the numerical computations presented in this paper, a value of $\alpha_{CFL} = 0.3$, unless otherwise stated, has been chosen to ensure both accuracy and stability [38] of the algorithm.

It is important to point out that the resulting Upwind-SPH algorithm (either (38) or (39)) does not intrinsically fulfil conservation of angular momentum, since the strain measures $\{\boldsymbol{F}, \boldsymbol{H}, J\}$ are no longer exclusively computed from the current geometry [42]. For instance, the deformation gradient $\boldsymbol{F} \neq \boldsymbol{F}_{\boldsymbol{x}} := \boldsymbol{\nabla}_0 \boldsymbol{x}$, its co-factor $\boldsymbol{H} \neq \boldsymbol{H}_{\boldsymbol{x}} := \frac{1}{2}\boldsymbol{F}_{\boldsymbol{x}} \times \boldsymbol{F}_{\boldsymbol{x}}$ and its Jacobian $J \neq J_{\boldsymbol{x}} := \det \boldsymbol{F}_{\boldsymbol{x}}$. In this paper, a monolithic discrete angular momentum projection algorithm presented in Lee *et al*. [1] is employed and is summarised in Appendix B. Specifically, both the internal nodal force $\boldsymbol{T}_a$ and the particle-based upwinding stabilisation term $\boldsymbol{\mathcal{D}}(\boldsymbol{p}_a)$, described in (38a), are modified in a least-square sense in order to preserve the total angular momentum, whilst still ensuring the global conservation of linear momentum.

5. Artificial compressibility

5.1. General remark

As it is well known, in the case of truly incompressible or nearly incompressible materials, the volumetric wave speed c_p can reach very large values leading to prohibitively small time steps [28]. This can have a very negative effect on the computational efficiency of any time-explicit algorithm. One of the most popular approaches to address this issue is the artificial compressibility method, originally developed for the Navier-Stokes equations [31–33]. Taking inspiration from the fractional step algorithm presented in Gil *et al.* [26, 30], the artificial compressibility approach is here adapted to the set of first order conservation law equations presented in (1).

To achieve this, it is first important to re-write the volume map conservation law (3b) in terms of the pressure unknown by utilising the volumetric constitutive law used in this paper, namely $p = \kappa(J-1)$ (refer to equation (11) on pg. 75 in Reference [1]). This equation now reads

$$\frac{1}{\kappa}\frac{\partial p}{\partial t} = \boldsymbol{H} : \boldsymbol{\nabla}_0 \left(\frac{\boldsymbol{p}}{\rho_0} \right). \tag{42}$$

In this case, the new unknowns of the problem are $\{\boldsymbol{p}, \boldsymbol{F}, \boldsymbol{H}, p\}$ (with J being replaced by the pressure variable p). For a truly incompressible material, $\kappa \approx \infty$ and the left hand side of equation (42) vanishes, resulting in an incompressibility constraint [31].

In this approach, we first discretise the continuum equations (1a, 1b, 1c, 42) in time and then proceed to discretise in space via a Riemann-based upwinding stabilisation as presented in Section 3.3.2. For satisfaction of the incompressibility constraint, we can update the evolution equations of the linear momentum (1a) and pressure (42) as follows [26, 30]

$$\frac{\boldsymbol{p}^{n+1} - \boldsymbol{p}^n}{\Delta t} - \mathrm{DIV}\boldsymbol{P}(\boldsymbol{F}^n, \boldsymbol{H}^n, p^{n+1}) - \boldsymbol{f}_0^n = \boldsymbol{0}; \tag{43a}$$

$$\frac{p^{n+1} - p^n}{\kappa \Delta t} - \boldsymbol{H}^n : \boldsymbol{\nabla}_0 \left(\frac{\boldsymbol{p}^{n+1}}{\rho_0} \right) = 0. \tag{43b}$$

Both the pressure and linear momentum conservation variables are solved implicitly in t^{n+1}, assuming the deformation gradient $\boldsymbol{F}$ and its cofactor $\boldsymbol{H}$ to be frozen at time t^n.

In order to solve equations (43a,b), a predictor-corrector algorithm is used. The algorithm is first advanced explicitly yielding intermediate variables $\{\boldsymbol{p}^{\mathrm{int}}, p^{\mathrm{int}}\}$ which are then projected after iteratively solving an implicit system known as pressure correction. Therefore, the first (predictor or intermediate) step of the scheme over a time step Δt is defined as

$$\frac{\left(\boldsymbol{p}^{\mathrm{int}} - \boldsymbol{p}^n\right)}{\Delta t} - \mathrm{DIV}\boldsymbol{P}(\boldsymbol{F}^n, \boldsymbol{H}^n, p^n) - \boldsymbol{f}_0^n = \boldsymbol{0}; \tag{44a}$$

$$\frac{\boldsymbol{F}^{n+1} - \boldsymbol{F}^n}{\Delta t} - \boldsymbol{\nabla}_0 \left(\frac{\boldsymbol{p}^n}{\rho_0} \right) = \boldsymbol{0}; \tag{44b}$$

$$\frac{\boldsymbol{H}^{n+1} - \boldsymbol{H}^n}{\Delta t} - \boldsymbol{F}^n \boldsymbol{\times} \boldsymbol{\nabla}_0 \left(\frac{\boldsymbol{p}^n}{\rho_0} \right) = \boldsymbol{0}; \tag{44c}$$

$$\frac{1}{\kappa}\frac{p^{\mathrm{int}} - p^n}{\Delta t} - \boldsymbol{H}^n : \boldsymbol{\nabla}_0 \left(\frac{\boldsymbol{p}^n}{\rho_0} \right) = 0. \tag{44d}$$

The second (corrector or projection) step becomes

$$\frac{\left(\boldsymbol{p}^{n+1}-\boldsymbol{p}^{\text{int}}\right)}{\Delta t}-\text{DIV}\left[\left(p^{n+1}-p^{n}\right)\boldsymbol{H}^{n}\right]=\boldsymbol{0}; \tag{45a}$$

$$\frac{1}{\kappa}\frac{\left(p^{n+1}-p^{\text{int}}\right)}{\Delta t}-\boldsymbol{H}^{n}:\boldsymbol{\nabla}_{0}\left(\frac{\boldsymbol{p}^{n+1}}{\rho_{0}}-\frac{\boldsymbol{p}^{n}}{\rho_{0}}\right)=0. \tag{45b}$$

Here, the maximum time step Δt of the predictor-corrector algorithm described above is governed by the maximum p-wave speed dependent on the bulk modulus κ of a material.

For nearly (and truly) incompressible materials, the bulk modulus present in the first term of equation (44d) can potentially reach very high values (even infinite), leading to extremely small time steps. This will then destroy the explicit nature of the predictor step of the scheme. It is for this reason that a fictitious bulk modulus $\tilde{\kappa}$ is used in its place, yielding

$$\frac{1}{\tilde{\kappa}}\frac{p^{\text{int}}-p^{n}}{\Delta t}-\boldsymbol{H}^{n}:\boldsymbol{\nabla}_{0}\left(\frac{\boldsymbol{p}^{n}}{\rho_{0}}\right)=0. \tag{46}$$

As a consequence, the projection step of the pressure equation (45b) now becomes

$$\frac{1}{\kappa}\frac{\left(p^{n+1}-p^{n}\right)}{\Delta t}-\frac{1}{\tilde{\kappa}}\frac{p^{\text{int}}-p^{n}}{\Delta t}-\boldsymbol{H}^{n}:\boldsymbol{\nabla}_{0}\left(\frac{\boldsymbol{p}^{n+1}}{\rho_{0}}-\frac{\boldsymbol{p}^{n}}{\rho_{0}}\right)=0. \tag{47}$$

Notice that the summation of both equations (46) and (47) recovers the original assumption in which the linear momentum variable is treated implicitly in the formulation.

Finally, in order to solve the implicit system for the correction (refer to (45a) and (47)), one approach is to employ an iterative artificial compressibility algorithm [29]. This can be achieved through the introduction of a pseudo time derivative term $\frac{\partial}{\partial\tau}$ to expressions (45a) and (47), and after rearranging gives

$$\frac{\partial\boldsymbol{p}}{\partial\tau}=\text{DIV}\left[\left(p^{n+1}-p^{n}\right)\boldsymbol{H}^{n}\right]-\frac{\left(\boldsymbol{p}^{n+1}-\boldsymbol{p}^{\text{int}}\right)}{\Delta t}; \tag{48a}$$

$$\frac{1}{\gamma}\frac{\partial p}{\partial\tau}=\frac{1}{\tilde{\kappa}}\frac{p^{\text{int}}-p^{n}}{\Delta t}+\boldsymbol{H}^{n}:\boldsymbol{\nabla}_{0}\left(\frac{\boldsymbol{p}^{n+1}}{\rho_{0}}-\frac{\boldsymbol{p}^{n}}{\rho_{0}}\right)-\frac{1}{\kappa}\frac{\left(p^{n+1}-p^{n}\right)}{\Delta t}, \tag{48b}$$

where γ represents the artificial compressibility parameter. In this work, the pseudo terms are also advanced in time using exactly the same time integrator described in (40). The SPH spatial discretisation for the predictor-corrector system (44a, 44b, 44c, 46, 48a, 48b) will be presented in the following section.

Remark 5:

In contrast to the artificial compressibility algorithm used in system (48a-48b), an alternative approach based on a pressure Poisson equation [26, 30] is also presented here for completeness. In this approach, the pressure correction can be re-formulated by combining (46) into (47), to give

$$\frac{1}{\kappa}\frac{\left(p^{n+1}-p^{n}\right)}{\Delta t}-\boldsymbol{H}^{n}:\boldsymbol{\nabla}_{0}\left(\frac{\boldsymbol{p}^{n+1}}{\rho_{0}}\right). \tag{49}$$

Substitution of (45a) into (49) for $\boldsymbol{p}^{n+1}$ yields

$$\frac{1}{\kappa}\frac{\left(p^{n+1}-p^{n}\right)}{\Delta t}-\Delta t\boldsymbol{H}^{n}:\boldsymbol{\nabla}_{0}\left(\frac{\boldsymbol{p}^{\text{int}}}{\rho_{0}}\right)-\boldsymbol{H}^{n}:\boldsymbol{\nabla}_{0}\left[\text{DIV}\left(\frac{1}{\rho_{0}}\left(p^{n+1}-p^{n}\right)\boldsymbol{H}^{n}\right)\right]=0. \tag{50}$$

For evaluation of the pressure increment, equation above however requires the solution of a system of nonlinear equations at each time step. This is indeed not computationally efficient when employing a mesh-free SPH discretisation, hence not pursued in this work.

5.2. SPH artificial compressibility algorithm

Following the SPH discretisation procedure presented in Section 3, the predictor step of the mixed-based system $\{\boldsymbol{p}, \boldsymbol{F}, \boldsymbol{H}, p\}$ is

$$\frac{\boldsymbol{p}_a^{\text{int}} - \boldsymbol{p}_a^n}{\Delta t} = \boldsymbol{E}_a^n - \boldsymbol{T}_a^n + \boldsymbol{\mathcal{D}}(\boldsymbol{p}_a^n); \tag{51a}$$

$$\frac{\boldsymbol{F}_a^{n+1} - \boldsymbol{F}_a^n}{\Delta t} = \sum_{b \in \Lambda_a^b} \left(\frac{\boldsymbol{p}_b^n}{\rho_0} \right) \otimes \boldsymbol{G}_b(\boldsymbol{X}_a); \tag{51b}$$

$$\frac{\boldsymbol{H}_a^{n+1} - \boldsymbol{H}_a^n}{\Delta t} = \boldsymbol{F}_a^n \boldsymbol{\times} \sum_{b \in \Lambda_a^b} \left(\frac{\boldsymbol{p}_b^n}{\rho_0} \right) \otimes \boldsymbol{G}_b(\boldsymbol{X}_a); \tag{51c}$$

$$\frac{1}{\tilde{\kappa}} \frac{p_a^{\text{int}} - p_a^n}{\Delta t} = \boldsymbol{H}_a^n : \sum_{b \in \Lambda_a^b} \left(\frac{\boldsymbol{p}_b^n}{\rho_0} \right) \otimes \boldsymbol{G}_b(\boldsymbol{X}_a) + \mathcal{D}(J_a^n), \tag{51d}$$

with the stabilising terms $\{\boldsymbol{\mathcal{D}}(\boldsymbol{p}_a), \mathcal{D}(J_a)\}$ and the internal and external force vectors $\{\boldsymbol{T}_a, \boldsymbol{E}_a\}$ defined in Section 3.3.

In addition, the corrector step of the discrete system $\{\boldsymbol{p}, \boldsymbol{F}, \boldsymbol{H}, p\}$ becomes

$$\frac{d\boldsymbol{p}_a}{d\tau} = \sum_{b \in \Lambda_a^b} \left[\left(p_b^{n+1} - p_b^n \right) \boldsymbol{H}_b^n \right] \boldsymbol{G}_b(\boldsymbol{X}_a) - \frac{\left(\boldsymbol{p}_a^{n+1} - \boldsymbol{p}_a^{\text{int}} \right)}{\Delta t}; \tag{52a}$$

$$\frac{1}{\gamma} \frac{dp_a}{d\tau} = \frac{1}{\tilde{\kappa}} \frac{p_a^{\text{int}} - p_a^n}{\Delta t} - \frac{1}{\kappa} \frac{(p_a^{n+1} - p_a^n)}{\Delta t} + \boldsymbol{H}_a^n : \sum_{b \in \Lambda_a^b} \left(\frac{\boldsymbol{p}_b^{n+1}}{\rho_0} - \frac{\boldsymbol{p}_b^n}{\rho_0} \right) \otimes \boldsymbol{G}_b(\boldsymbol{X}_a). \tag{52b}$$

At each time step Δt, above system (52) is iteratively solved for the linear momentum and pressure within the pseudo time integration, aims at obtaining convergence to a pseudo steady state (e.g. $\frac{d\boldsymbol{p}_a}{d\tau} \approx \boldsymbol{0}$ and $\frac{dp_a}{d\tau} \approx 0$).

5.3. Iteration speed-up procedure

To accelerate the speed of convergence within the iterative process, we can incorporate an additional Laplacian (or harmonic) dissipative operator to equation (52b), which results in

$$\frac{1}{\gamma} \frac{dp_a}{d\tau} = \frac{1}{\tilde{\kappa}} \frac{p_a^{\text{int}} - p_a^n}{\Delta t} - \frac{1}{\kappa} \frac{(p_a^{n+1} - p_a^n)}{\Delta t} + \boldsymbol{H}_a^n : \sum_{b \in \Lambda_a^b} \left(\frac{\boldsymbol{p}_b^{n+1}}{\rho_0} - \frac{\boldsymbol{p}_b^n}{\rho_0} \right) \otimes \boldsymbol{G}_b(\boldsymbol{X}_a) + \mathcal{D}_{\text{pseudo}}(p_a). \tag{53}$$

The discrete pseudo viscosity term at particle a can be written as

$$\mathcal{D}_{\text{pseudo}}(p_a) := \eta \mathcal{L}\left[p(\boldsymbol{X}_a) \right]; \qquad \eta = \alpha \frac{c_s^2 \Delta t}{\mu}, \tag{54}$$

where α is a dimensionless user-defined parameter in the range of $[0, 1]$. A challenging aspect remains as to how to approximate the (particle based) Laplacian dissipative operator to ensure fulfillment of the global conservation requirement, that is $\sum_a V_a \mathcal{D}_{\text{pseudo}}(p_a) = 0$.

Referring to Appendix C, the discrete Laplacian viscosity operator (C.4) used in this work is approximated as [64]

$$\mathcal{L}\left[p(\boldsymbol{X}_a)\right] \approx 2\sum_{b\in\Lambda_a^b} V_b \left[\frac{p_b - p_a}{\|\boldsymbol{X}_b - \boldsymbol{X}_a\|}\boldsymbol{N}_{ab}\right]\cdot \tilde{\boldsymbol{\nabla}}_0 \tilde{\mathrm{W}}_b(\boldsymbol{X}_a). \tag{55}$$

Unfortunately, the evaluation of Laplacian operator prevents the exact global conservation due to the lack of symmetry of the kernel gradient correction, that is $\tilde{\boldsymbol{\nabla}}_0\tilde{\mathrm{W}}_b(\boldsymbol{X}_a) \neq \tilde{\boldsymbol{\nabla}}_0\tilde{\mathrm{W}}_a(\boldsymbol{X}_b)$. This issue can also be addressed by replacing $\tilde{\boldsymbol{\nabla}}_0\tilde{\mathrm{W}}_b(\boldsymbol{X}_a)$ with $\tilde{\boldsymbol{\nabla}}_0\tilde{\mathrm{W}}_b^{\mathrm{Ave}}(\boldsymbol{X}_a)$ (32).

Remark 6: Following [1], an alternative approach to approximate the (globally conservative) Laplacian evaluation of the pressure variable p can be expressed as

$$\mathcal{L}\left[p(\boldsymbol{X}_a)\right] \approx \sum_{b\in\Lambda_a^b} V_b \left[p_b - p_a\right] \tilde{\Delta}_0 \mathrm{W}_b^{\mathrm{Ave}}(\boldsymbol{X}_a), \tag{56}$$

where $\tilde{\Delta}_0\mathrm{W}_b^{\mathrm{Ave}}(\boldsymbol{X}_a)$ is defined as

$$\tilde{\Delta}_0\mathrm{W}_b^{\mathrm{Ave}}(\boldsymbol{X}_a) := \frac{1}{2}\left[\tilde{\Delta}_0\mathrm{W}_b(\boldsymbol{X}_a) + \tilde{\Delta}_0\mathrm{W}_a(\boldsymbol{X}_b)\right]. \tag{57}$$

Here, $\tilde{\Delta}_0$ is a corrected Laplacian approximation which can be obtained through a least-square minimisation procedure (see Appendix A in [1] for further details). This requires the solution of a system of equations and for this reason not pursued in this paper.

Thus, the discrete pseudo viscosity operator can be described as

$$\mathcal{D}_{\mathrm{pseudo}}(p_a) \approx 2\eta\sum_{b\in\Lambda_a^b} V_b \left[\frac{p_b - p_a}{\|\boldsymbol{X}_b - \boldsymbol{X}_a\|}\boldsymbol{N}_{ab}\right]\cdot \tilde{\boldsymbol{\nabla}}_0 \tilde{\mathrm{W}}_b^{\mathrm{Ave}}(\boldsymbol{X}_a). \tag{58}$$

Notice here that the only purpose of adding viscosity operator $\mathcal{D}_{\mathrm{pseudo}}(p_a)$ to (53) is to accelerate the speed of convergence within the pseudo time integration process when iteratively solving the implicit system for pressure correction (52a, 53). This is in clear contrast to the upwinding stabilisation terms $\{\boldsymbol{\mathcal{D}}(\boldsymbol{p}_a), \mathcal{D}(J_a)\}$ introduced in the predictor step (51), crucial to ensure the robustness (stability) of the algorithm.

6. Algorithmic description

For ease of understanding, Algorithm 1 summarises the complete algorithmic description of the mixed-based $\{\boldsymbol{p}, \boldsymbol{F}, \boldsymbol{H}, J\}$ Upwind Smooth Particle Hydrodynamics (Upwind-SPH) methodology, with all the necessary numerical ingredients. Notice that simpler $\{\boldsymbol{p}, \boldsymbol{F}\}$ and $\{\boldsymbol{p}, \boldsymbol{F}, J\}$ versions of the algorithm can be easily obtained by neglecting the relevant geometric conservation laws (i.e. (39b) and/or (39c)).

7. Numerical examples

An ample spectrum of numerical examples is presented in order to examine the performance of the proposed SPH methodology in compressible, nearly incompressible and truly incompressible scenarios. Specifically, three stabilised mixed-based SPH methodologies are analysed, namely $\{\boldsymbol{p}, \boldsymbol{F}\}$, $\{\boldsymbol{p}, \boldsymbol{F}, J\}$ and $\{\boldsymbol{p}, \boldsymbol{F}, \boldsymbol{H}, J\}$ Upwind-SPH. For validation purposes, some of the results are benchmarked against other in-house mixed-based numerical schemes, including: Finite Element Method [25–27, 30, 35], Finite Volume Method [3, 34, 38, 42] and SPH [1, 2].

Algorithm 1: Complete stabilised Upwind-SPH mixed methodology

Input : $\boldsymbol{\mathcal{U}}_a^n$ where $\boldsymbol{\mathcal{U}} = [\boldsymbol{p}\ \boldsymbol{F}\ \boldsymbol{H}\ J]^T$

Output: $\boldsymbol{\mathcal{U}}_a^{n+1}$, $\boldsymbol{P}_a^{n+1}$, $\boldsymbol{x}_a^{n+1}$

(1) ASSIGN old primary variables: $\boldsymbol{\mathcal{U}}_a^{\text{old}} = \boldsymbol{\mathcal{U}}_a^n$ and $\boldsymbol{x}_a^{\text{old}} = \boldsymbol{x}_a^n$

(2) EVALUATE p-wave speed: c_p (see References [30, 42])

(3) COMPUTE time increment: Δt

for *TVD-RK time integrator* $= 1$ **to** 2 **do**

(4) COMPUTE right-hand-side of the mixed-based system: $\dot{\boldsymbol{p}}_a$ (38a), $\dot{\boldsymbol{F}}_a$ (38b), $\dot{\boldsymbol{H}}_a$ (38c) and $\dot{J}_a$ (38d)

(5) APPLY discrete angular momentum preserving algorithm (see Section 6 of [1])

(6) EVOLVE $\{\boldsymbol{\mathcal{U}}_a, \boldsymbol{x}_a\}$ via TVD-RK (40)

(7) COMPUTE first Piola $\boldsymbol{P}_a$ (see Eqn. (12) on pg. 75 in Reference [1])

end

(8) UPDATE $\{\boldsymbol{\mathcal{U}}_a^{n+1}, \boldsymbol{x}_a^{n+1}\}$ (see 40)

(9) COMPUTE first Piola $\boldsymbol{P}_a^{n+1}$ (see Eqn. (12) on pg. 75 in Reference [1])

Table 1: Numerical values for the relative error of the components of linear momentum and stress as compared to the exact solution, measured with the L_2 norm. Comparison between the $\{\boldsymbol{p}, \boldsymbol{F}, \boldsymbol{H}, J\}$ Upwind-SPH, $\{\boldsymbol{p}, \boldsymbol{F}, \boldsymbol{H}, J\}$ SUPG-SPH and $\{\boldsymbol{p}, \boldsymbol{F}, \boldsymbol{H}, J\}$ JST-SPH. Convergence rate calculated using the results of the two finest meshes.

Error values p_x

h	$\{\boldsymbol{p}, \boldsymbol{F}, \boldsymbol{H}, J\}$ Upwind	$\{\boldsymbol{p}, \boldsymbol{F}, \boldsymbol{H}, J\}$ SUPG-SPH	$\{\boldsymbol{p}, \boldsymbol{F}, \boldsymbol{H}, J\}$ JST-SPH
1/4	2.490×10^{-3}	2.690×10^{-3}	6.635×10^{-3}
1/8	8.123×10^{-4}	8.987×10^{-4}	1.986×10^{-3}
1/16	2.198×10^{-4}	2.578×10^{-4}	5.697×10^{-4}
1/24	9.342×10^{-5}	1.177×10^{-4}	2.510×10^{-4}
conv. rate	2.110	1.934	2.022

Error values P_{xX}

h	$\{\boldsymbol{p}, \boldsymbol{F}, \boldsymbol{H}, J\}$ Upwind	$\{\boldsymbol{p}, \boldsymbol{F}, \boldsymbol{H}, J\}$ SUPG-SPH	$\{\boldsymbol{p}, \boldsymbol{F}, \boldsymbol{H}, J\}$ JST-SPH
1/4	4.422×10^{-3}	3.964×10^{-3}	9.976×10^{-3}
1/8	2.269×10^{-3}	2.051×10^{-3}	4.156×10^{-3}
1/16	5.554×10^{-4}	5.805×10^{-4}	1.184×10^{-3}
1/24	2.513×10^{-4}	2.456×10^{-4}	5.248×10^{-4}
conv. rate	1.956	2.122	2.007

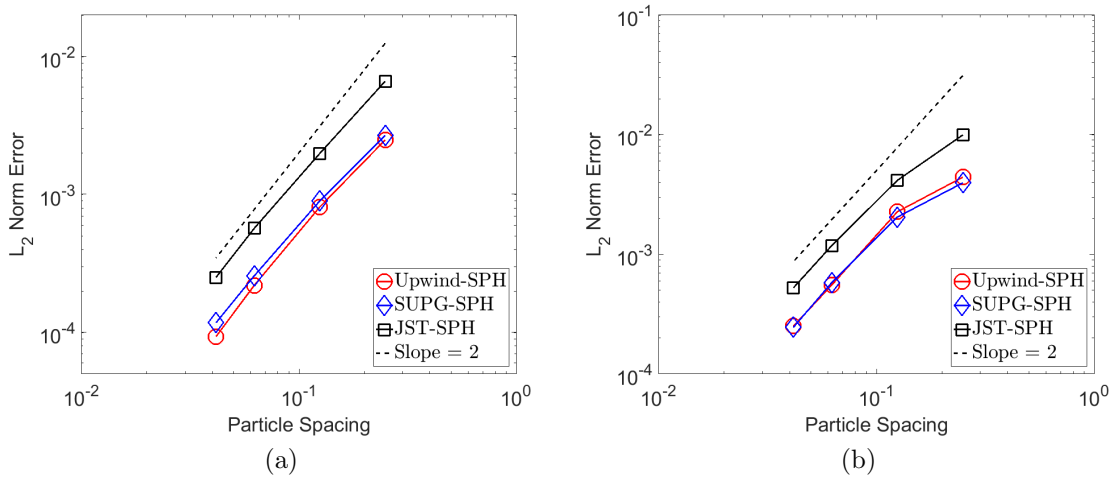

Figure 5: Swinging cube. L_2 norm convergence of components of (a) Linear momentum; and (b) Stresses at a particular time $t = 0.002$ s. Results obtained using a neo-Hookean constitutive model with $A = B = C = 1$ and $U_0 = 5 \times 10^{-4}$ using the proposed SPH methodologies. The material properties used are Young's modulus $E = 17$ MPa, density $\rho_0 = 1100$ kg/m^3, Poisson's ratio $\nu = 0.3$ and $\alpha_{\text{CFL}} = 0.3$.

7.1. Conservation, consistency and convergence

7.1.1. Swinging cube

As already explored in References [2, 3, 25–27, 30, 34, 38, 42, 58], the first example shows a cube of unit side length with symmetric boundary conditions (e.g. restricted normal displacement) at faces $X = 0$, $Y = 0$ and $Z = 0$ and skew-symmetric boundary conditions (i.e. restricted tangential displacement) at faces $X = 1$m, $Y = 1$m and $Z = 1$m (see Figure 3 on pg. 526 in [2]). The main objective of this example is to show the convergence behaviour of the proposed $\{\boldsymbol{p}, \boldsymbol{F}\}$, $\{\boldsymbol{p}, \boldsymbol{F}, J\}$ and $\{\boldsymbol{p}, \boldsymbol{F}, \boldsymbol{H}, J\}$ Upwind-SPH methodologies[5]. A linear elastic material with Young's modulus $E = 17$ MPa and Poisson's ratio $\nu = 0.3$ is considered. The density of the material is $\rho_0 = 1100$ kg/m^3 and the Courant-Friedrich-Levy number is $\alpha_{CFL} = 0.3$. Following Section 8.2 on pg. 85 of Reference [1], the convergence analysis is carried out by computing the L_2 norm of the error between the analytical solution of this problem and the numerical solution obtained for different values of the particle spacing. Table 1 shows a global L_2 convergence analysis of the linear momentum $\boldsymbol{p}$ and the first Piola Kirchhoff stress tensor $\boldsymbol{P}$ simulated using the $\{\boldsymbol{p}, \boldsymbol{F}, \boldsymbol{H}, J\}$ Upwind-SPH method[6], as compared to the analytical solution described in equation (52) of [1] (see Section 8.2 on pg. 85). Their corresponding graphical representations are depicted in Figure 5. As expected, all of the SPH schemes show equal second order convergence for both linear momentum and the components of the stress tensor. Both Upwind-SPH and SUPG-SPH methodologies show very similar convergence behaviour, as the stabilisation terms introduced in both methodologies are very well designed from a mathematical standpoint (e.g. Riemann solver and residual based stabilisation). However, a slight disadvantage of the SUPG-SPH method is the need to establish a secondary cloud of particles (e.g. stress points) for the evaluation of the residual based stabilisation term, which would

[5]Nearly identical results have been obtained for $\{\boldsymbol{p}, \boldsymbol{F}\}$ and $\{\boldsymbol{p}, \boldsymbol{F}, J\}$ Upwind-SPH methodologies, hence not presented.

[6]Given the fact that A=B=C, all the three components of linear momentum and stresses are of the same magnitude, namely p_x=p_y=p_z and P_{xX}=P_{yY}=P_{zZ}.

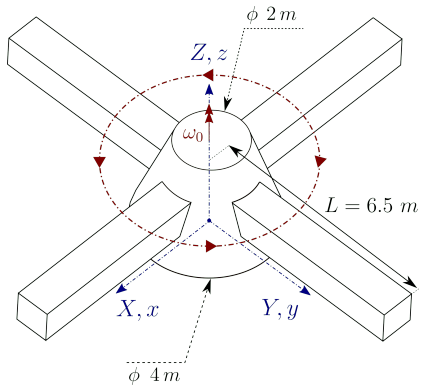

Figure 6: Satellite problem setup

require a non-trivial intervention of the user prior to the analysis run. More interestingly, the proposed Upwind-SPH method shows better accuracy than the JST-SPH algorithm previously reported in [1], with the same slope but with a lower translation error (see Figure 5). This is due to the fact that the Upwind-SPH method requires careful design (via an acoustic Riemann solver) of the stabilisation terms, without relying on the use of any user defined stabilisation parameters.

7.1.2. Satellite-like structure

In order to demonstrate the momentum conservation characteristics of the proposed algorithm, the motion of a satellite-like structure originally proposed by [59] is studied. The structure of a truncated cone of base radius 4 m, of top radius 2 m and of height 3 m, along with four attached arms of unit cross-section that extend 6.5 m from the centre of the structure (see Figure 6). The satellite is released without any initial deformation but with an initial angular velocity of $\Omega = 1$ rad/s about the centre of mass. The velocity field relative to the centre of mass $\boldsymbol{X}_{\text{cm}}$ is given as

$$\boldsymbol{v}^0(\boldsymbol{X}) = \boldsymbol{\omega} \times (\boldsymbol{X} - \boldsymbol{X}_{\text{cm}})\,; \qquad \boldsymbol{\omega} = (0, 0, \Omega)^T\,; \qquad \boldsymbol{X} = (X, Y, 0)\,. \tag{59}$$

A neo-Hookean model is chosen with the material parameters $\rho_0 = 1000$ kg/m^3, Young's modulus $E = 50.05$ kPa and Poisson's ratio $\nu = 0.3$. For visualisation purposes, a sequence of snapshots capturing the deformation of the satellite-like structure is shown in Figure 7. Figure 8 shows the time history of the components of the global angular and linear momenta, where both fields can be seen to remain constant whilst the structure deforms free from external effects. Activation of the angular momentum preserving algorithm enables the global angular momentum to remain constant. We show how the new Riemann-based $\{\boldsymbol{p}, \boldsymbol{F}\}$ Upwind-SPH algorithm fulfill global conservation, namely $\sum_a V_a \boldsymbol{\mathcal{D}}(\boldsymbol{p}_a) = \boldsymbol{0}$ and $\sum_a V_a \boldsymbol{T}_a = \boldsymbol{0}$ (see Figure 9).

7.2. Spurious pressure

7.2.1. Tensile test

A perforated block is clamped on its bottom surface and is left free on the rest of the boundaries (see Figure 10a). The main aim of this example is to illustrate the capability of the proposed Total Lagrangian Upwind-SPH algorithm in surpressing spurious pressure modes. The block is initially pulled with a linear variation in initial velocity field $\boldsymbol{v}_0 = V[0, 0, (Z/H)]^T$ where $V = 100$ m/s and $H = 0.5$ m. This problem is solved using a nearly incompressible

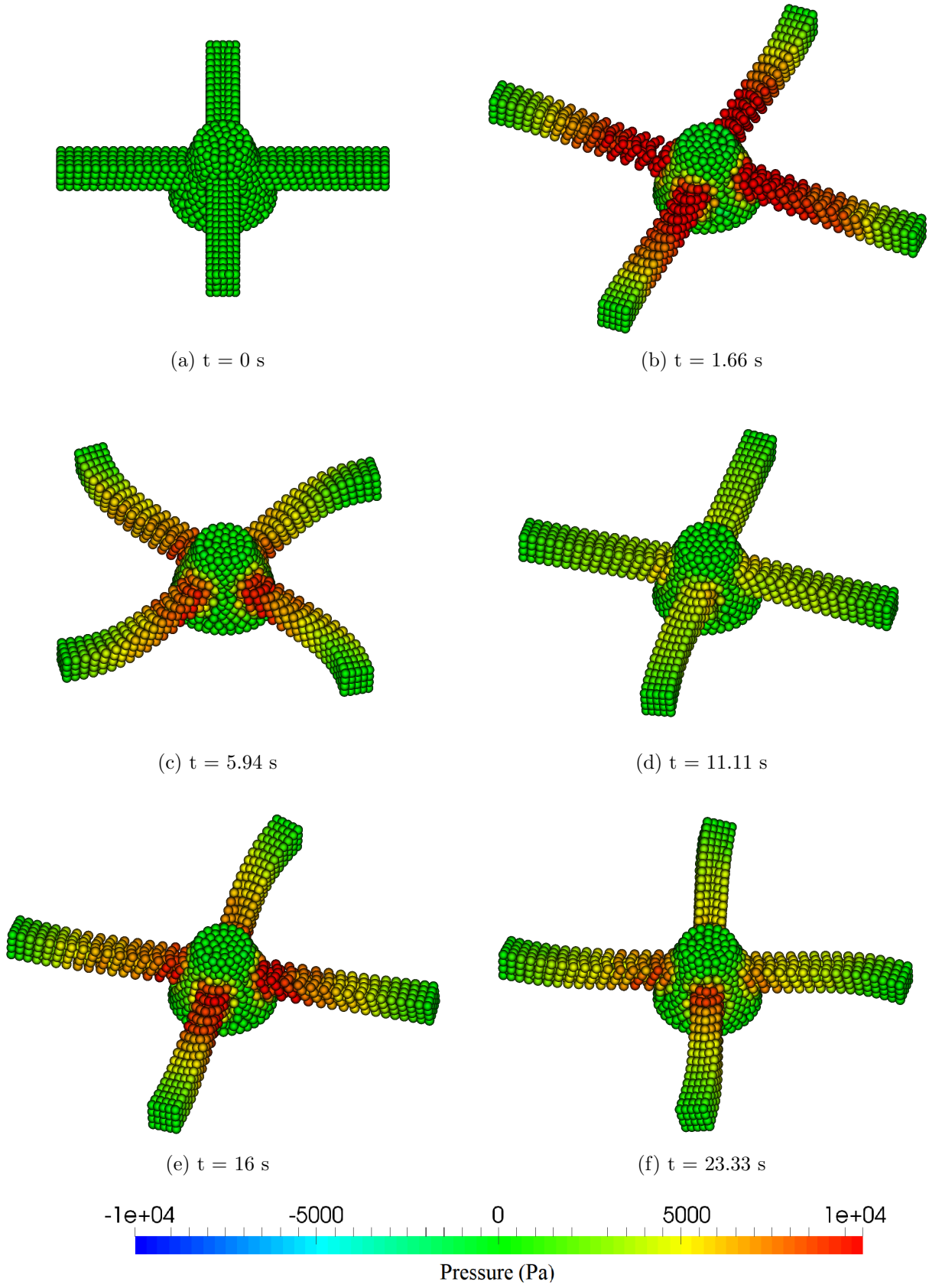

(a) t = 0 s

(b) t = 1.66 s

(c) t = 5.94 s

(d) t = 11.11 s

(e) t = 16 s

(f) t = 23.33 s

Figure 7: Satellite-like structure. Time evolution of the deformation along with the pressure distribution using the mixed-based $\{\boldsymbol{p}, \boldsymbol{F}\}$ Upwind-SPH. Results obtained with an angular velocity of $\boldsymbol{\omega} = [0, 0, 1]^T$ rad/s. A neo-Hookean constitutive model is employed with Young's modulus $E = 50046$ Pa, density $\rho_0 = 1000$ kg/m^3, Poisson's ratio $\nu = 0.3$ and $\alpha_{\text{CFL}} = 0.3$.

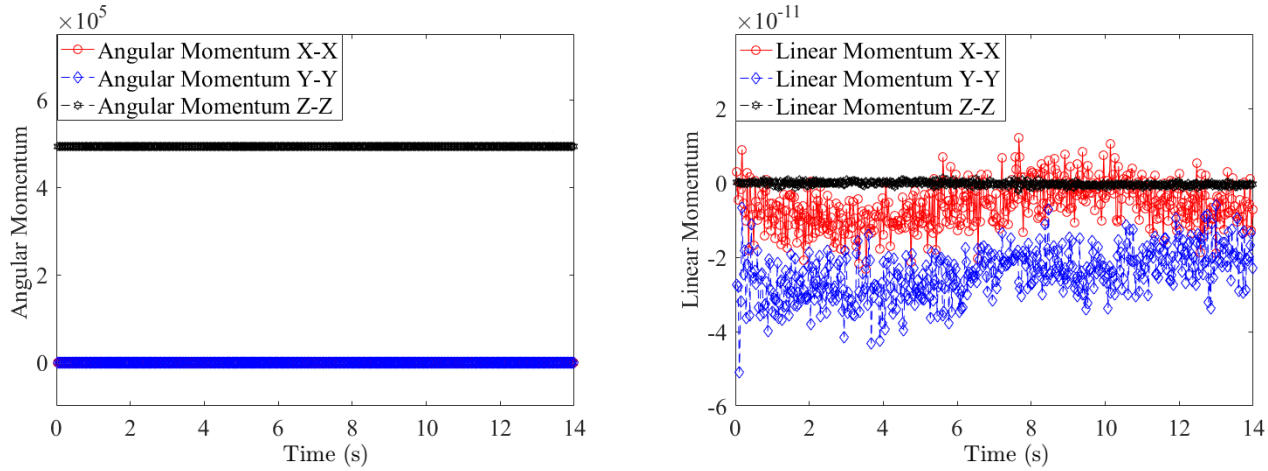

Figure 8: Satellite-like structure. Time evolution of the components of (a) Global angular momentum; and (b) Global linear momentum using the mixed-based $\{\boldsymbol{p}, \boldsymbol{F}\}$ Upwind-SPH. Results obtained with an angular velocity of $\boldsymbol{\omega} = [0, 0, 1]^T$ rad/s. A neo-Hookean constitutive model is employed with Young's modulus $E = 50046$ Pa, density $\rho_0 = 1000$ kg/m^3, Poisson's ratio $\nu = 0.3$ and $\alpha_{\text{CFL}} = 0.3$.

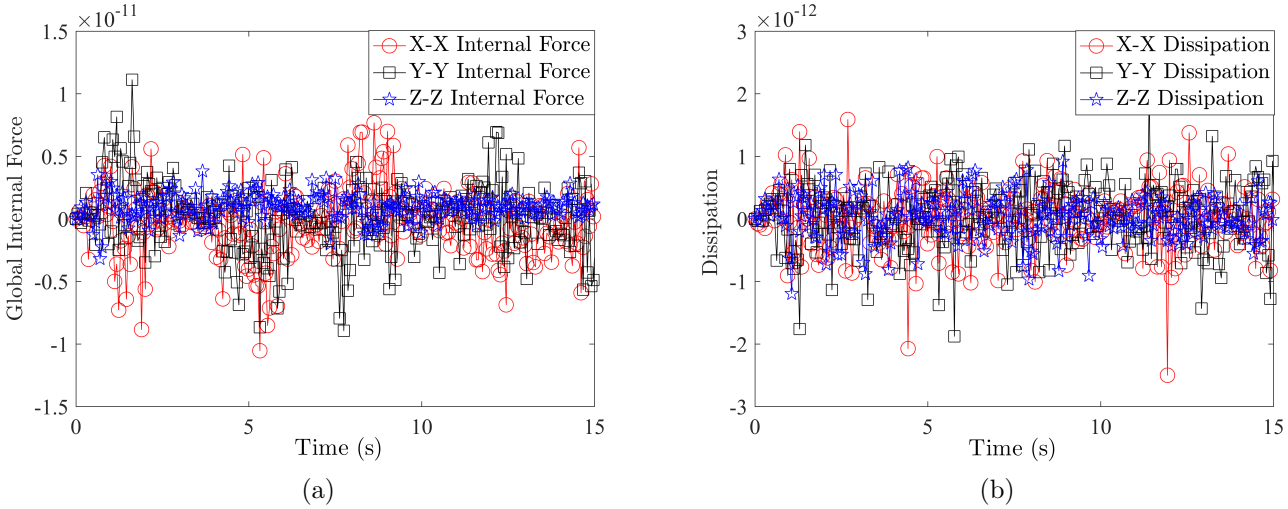

Figure 9: Satellite-like structure. Time evolution of the components of (a) Global internal force $\sum_a V_a \boldsymbol{T}_a \approx \boldsymbol{0}$ and (b) Global Riemann-based dissipation $\sum_a V_a \boldsymbol{\mathcal{D}}(\boldsymbol{p}_a) \approx \boldsymbol{0}$ of linear momentum evolution using the mixed-based $\{\boldsymbol{p}, \boldsymbol{F}\}$ Upwind-SPH algorithm. Results obtained with an angular velocity of $\boldsymbol{\omega} = [0, 0, 1]^T$ rad/s. A neo-Hookean constitutive model is employed with Young's modulus $E = 50046$ Pa, density $\rho_0 = 1000$ kg/m^3, Poisson's ratio $\nu = 0.3$ and $\alpha_{\text{CFL}} = 0.3$.

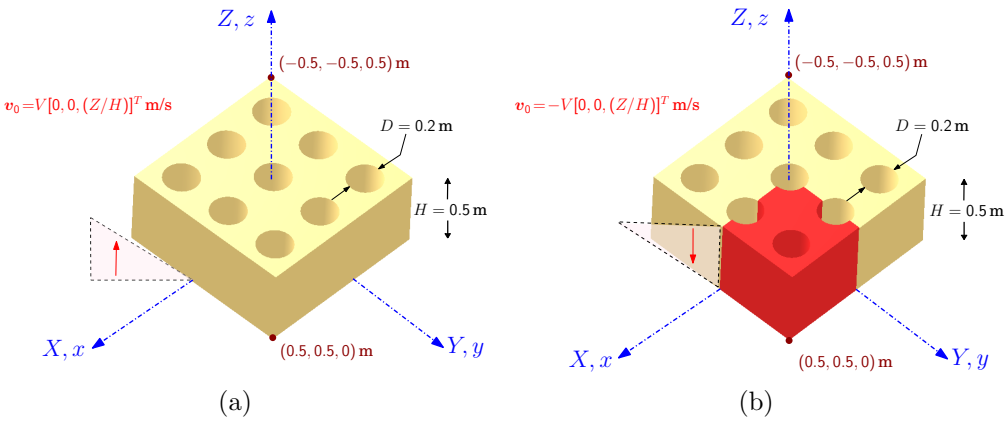

Figure 10: Problem setup: (a) Tensile test and (b) Punching test

neo-Hookean material with Young's modulus $E = 1.7 \times 10^7$ Pa, density $\rho_0 = 1.1 \times 10^3$ kg/m^3 and Poisson's ratio $\nu = 0.45$.

As illustrated in Figure 11, all of the proposed Total Lagrangian SPH methodologies, namely $\{\boldsymbol{p}, \boldsymbol{F}\}$, $\{\boldsymbol{p}, \boldsymbol{F}, J\}$ and $\{\boldsymbol{p}, \boldsymbol{F}, \boldsymbol{H}, J\}$ Upwind-SPH, are capable of eliminating tensile instability without showing pressure oscillations. Figure 12 shows the time evolution of the deformation pattern along with its pressure contour plot with three different views: isometric view, front view and top view. In this problem, extremely large distortions around the holes of the block are displayed[7]. Notice that in this type of problems, mesh-based methods as presented in [3, 25–27, 30, 34, 38, 42] are not suitable unless adaptive mesh refinement [60] is carried out.

To further examine the efficiency of the algorithm, the same problem is now assessed using a larger value of Poisson's ratio $\nu = 0.499$. As presented in Figure 13, the $\{\boldsymbol{p}, \boldsymbol{F}\}$ Upwind-SPH methodology shows excessive pressure fluctuations which eventually lead to an incorrect deformation path. For this reason, the conservation law for the Jacobian J is incorporated in order to stabilise the formulation, as already explored in previous publications [1, 2]. A smooth pressure spatial representation can then be observed when using $\{\boldsymbol{p}, \boldsymbol{F}, J\}$ and $\{\boldsymbol{p}, \boldsymbol{F}, \boldsymbol{H}, J\}$ Upwind-SPH methodologies. For completeness, Figure 14 depicts the time evolution of the deformation of the problem simulated using the $\{\boldsymbol{p}, \boldsymbol{F}, \boldsymbol{H}, J\}$ algorithm, displaying a smooth pressure contour.

7.2.2. Punch test

Similar to the tensile test described in Section 7.2.1, the perforated block is now left free on its top face and constrained with roller supports (i.e. symmetric boundary conditions) on the rest of the boundaries (see Figure 10b). The main objective of this example is to show the ability of the proposed methodology in alleviating severe pressure oscillations in highly constrained problems. The block is punched on a quarter of the domain with a linear variation of a velocity field $\boldsymbol{v}_0 = -V[0, 0, (Z/H)]^T$ where $V = 250$ m/s and $H = 0.5$ m. A nearly incompressible neo-Hookean material is used where Young's modulus $E = 1.7 \times 10^7$ Pa, density $\rho_0 = 1.1 \times 10^3$ kg/m^3 and Poisson's ratio $\nu = 0.499$.

As shown in [1, 2], addition of the volume map conservation law to the $\{\boldsymbol{p}, \boldsymbol{F}\}$ mixed-based system seems to be very efficient when solving problems with predominant nearly incompressible

[7]For simplicity, the inter-particle contact algorithm [56] is not considered in the present manuscript.

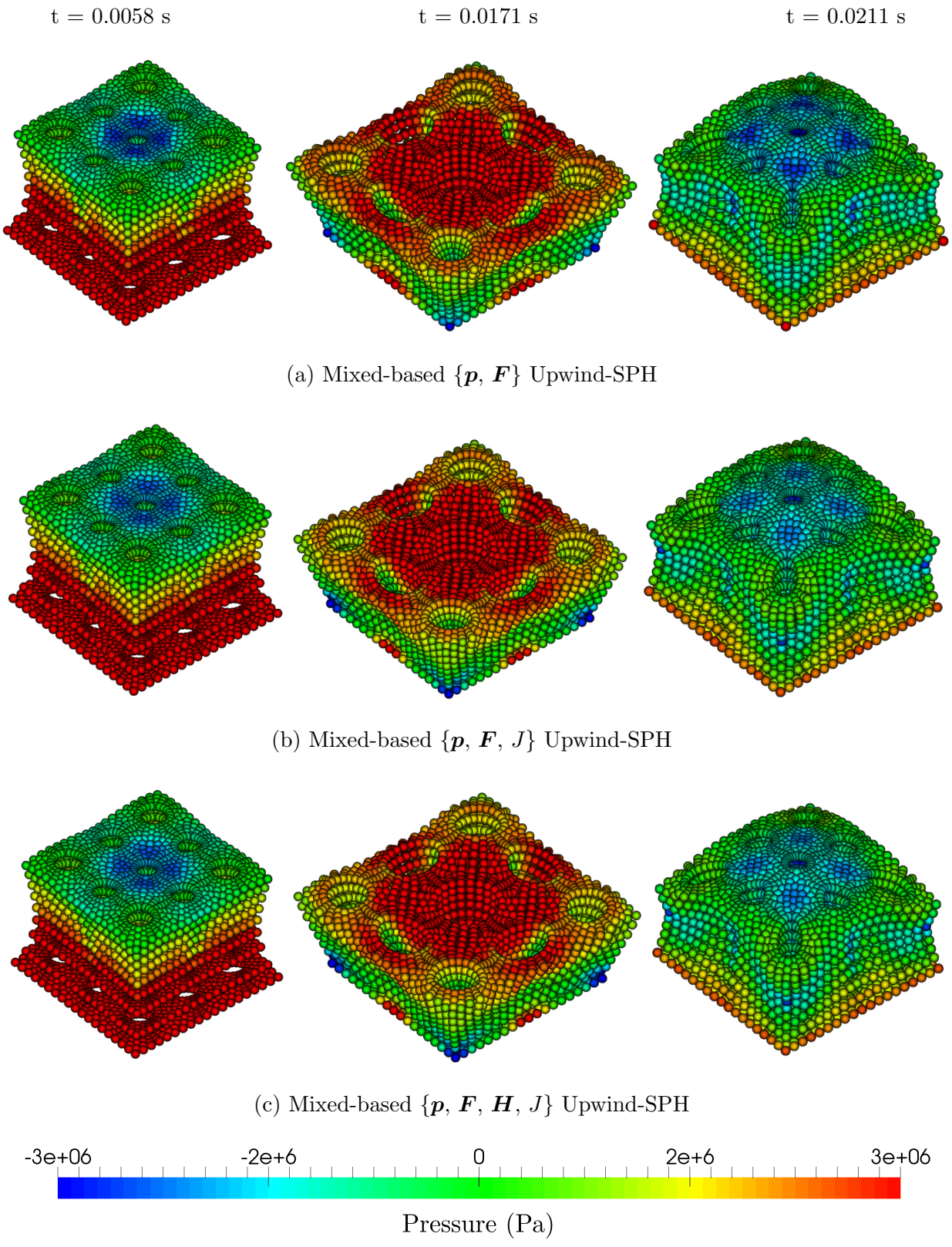

(a) Mixed-based $\{\boldsymbol{p}, \boldsymbol{F}\}$ Upwind-SPH

(b) Mixed-based $\{\boldsymbol{p}, \boldsymbol{F}, J\}$ Upwind-SPH

(c) Mixed-based $\{\boldsymbol{p}, \boldsymbol{F}, \boldsymbol{H}, J\}$ Upwind-SPH

Figure 11: Tensile cube. A sequence of deformed configurations using the mixed-based (a) $\{\boldsymbol{p}, \boldsymbol{F}\}$, (b) $\{\boldsymbol{p}, \boldsymbol{F}, J\}$ and (c) $\{\boldsymbol{p}, \boldsymbol{F}, \boldsymbol{H}, J\}$ Upwind-SPH. Results obtained with velocity field $\boldsymbol{v}_0 = V[0, 0, (Z/H)]^T$ where $V = 100$ m/s and $H = 0.5$ m. A neo-Hookean constitutive model is employed with Young's modulus $E = 1.7 \times 10^7$ Pa, density $\rho_0 = 1.1 \times 10^3$ kg/m^3, Poisson's ratio $\nu = 0.45$ and $\alpha_{\text{CFL}} = 0.3$.

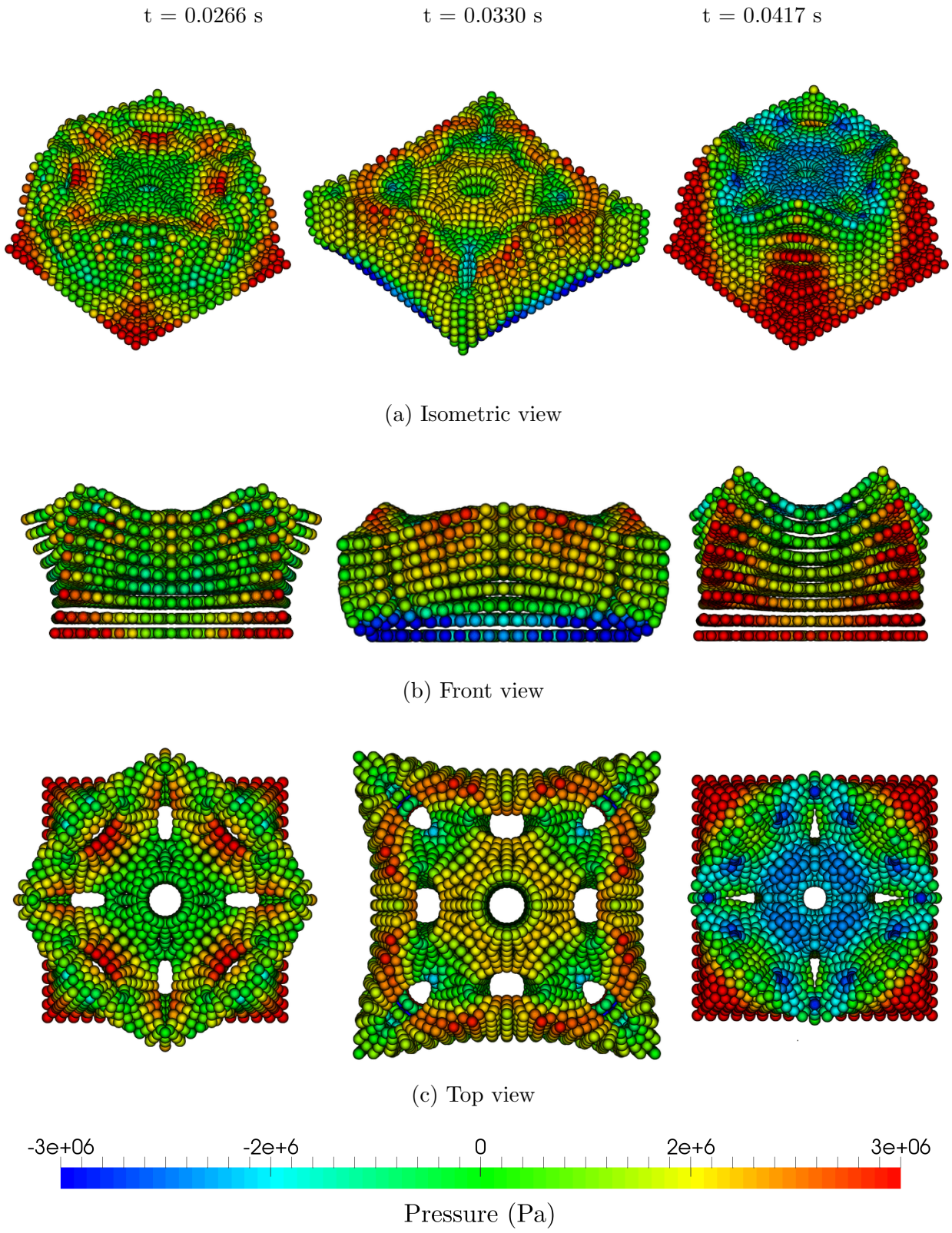

Figure 12: Tensile cube. A sequence of deformed configurations in three different views via the $\{\boldsymbol{p}, \boldsymbol{F}\}$ Upwind-SPH, namely: (a) Isometric view, (b) Front view, and (c) Top view. Results obtained with velocity field $\boldsymbol{v}_0 = V[0, 0, (Z/H)]^T$ where $V = 100$ m/s and $H = 0.5$ m. A neo-Hookean constitutive model is employed with Young's modulus $E = 1.7 \times 10^7$ Pa, density $\rho_0 = 1.1 \times 10^3$ kg/m^3, Poisson's ratio $\nu = 0.45$ and $\alpha_{\text{CFL}} = 0.3$.

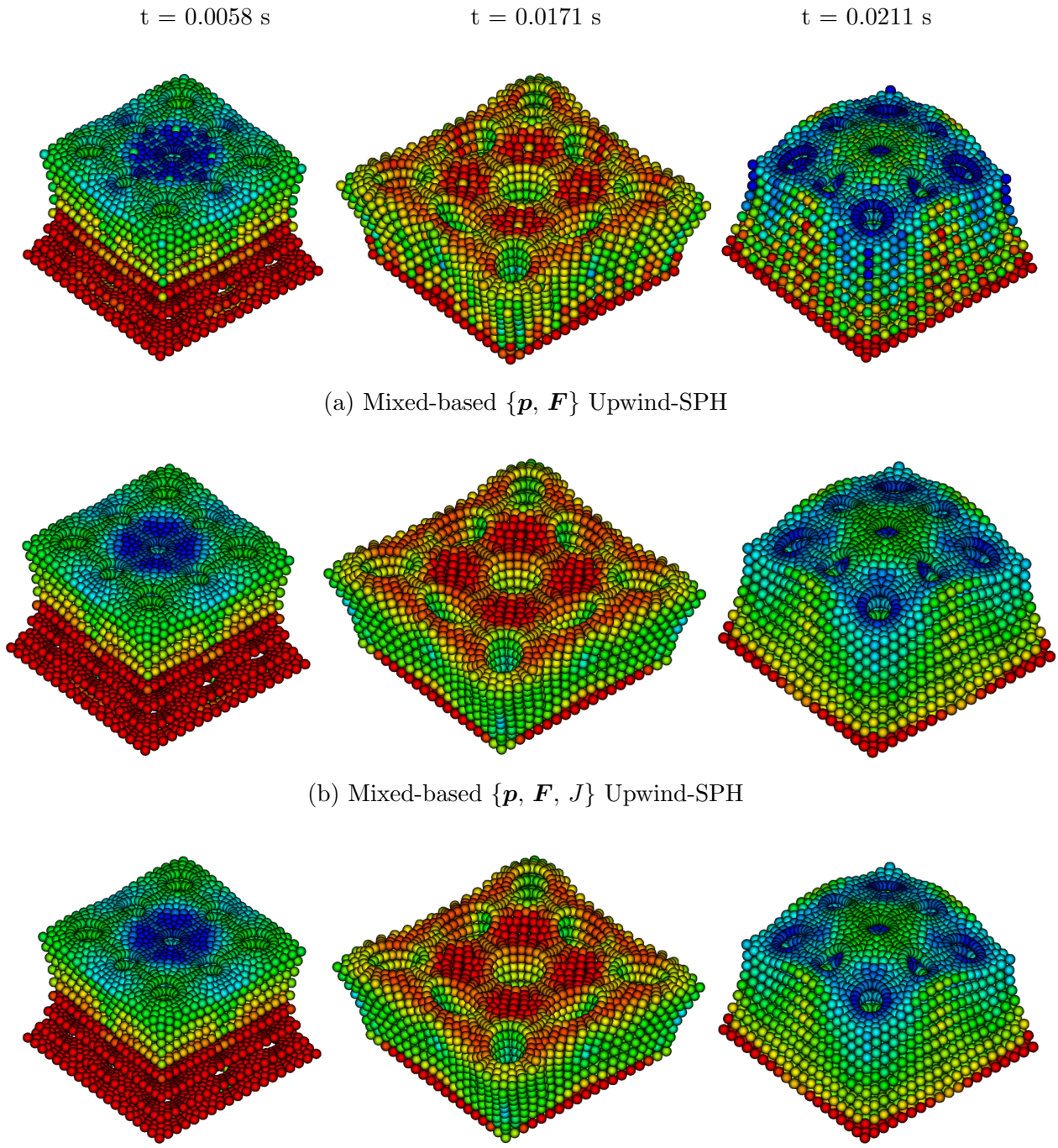

(a) Mixed-based $\{\boldsymbol{p}, \boldsymbol{F}\}$ Upwind-SPH

(b) Mixed-based $\{\boldsymbol{p}, \boldsymbol{F}, J\}$ Upwind-SPH

(c) Mixed-based $\{\boldsymbol{p}, \boldsymbol{F}, \boldsymbol{H}, J\}$ Upwind-SPH

Figure 13: Tensile cube. A sequence of deformed configurations using the mixed-based (a) $\{\boldsymbol{p}, \boldsymbol{F}\}$, (b) $\{\boldsymbol{p}, \boldsymbol{F}, J\}$ and (c) $\{\boldsymbol{p}, \boldsymbol{F}, \boldsymbol{H}, J\}$ Upwind-SPH. Results obtained with velocity field $\boldsymbol{v}_0 = V[0, 0, (Z/H)]^T$ where $V = 100$ m/s and $H = 0.5$ m. A nearly incompressible neo-Hookean constitutive model is employed with Young's modulus $E = 1.7 \times 10^7$ Pa, density $\rho_0 = 1.1 \times 10^3$ kg/m^3, Poisson's ratio $\nu = 0.499$ and $\alpha_{\text{CFL}} = 0.3$.

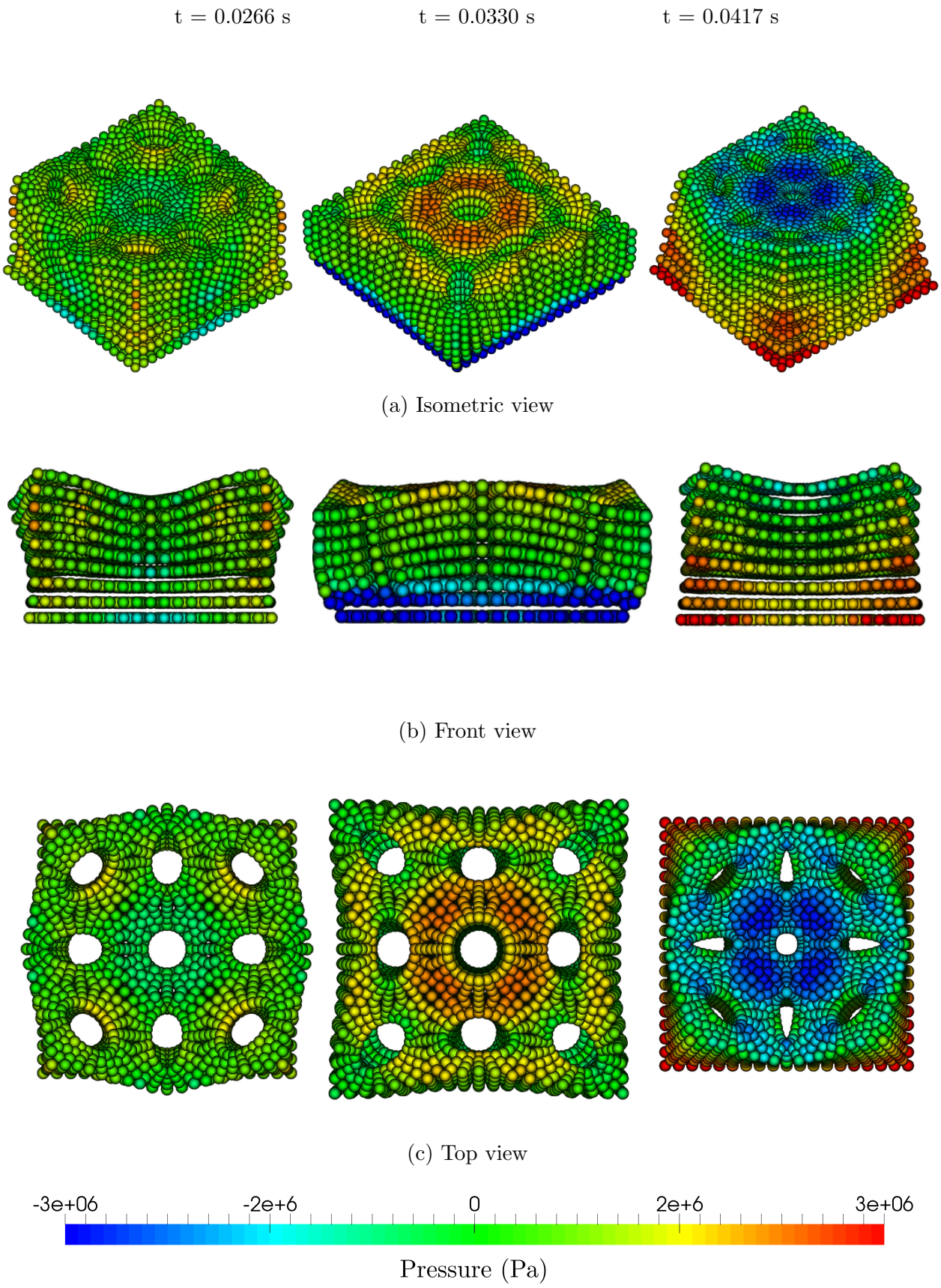

Figure 14: Tensile cube. A sequence of deformed configurations in three different views via the $\{\boldsymbol{p}, \boldsymbol{F}, \boldsymbol{H}, J\}$ Upwind-SPH: (a) Isometric view, (b) Front view, and (c) Top view. Results obtained with velocity field $\boldsymbol{v}_0 = V[0, 0, (Z/H)]^T$ where $V = 100$ m/s and $H = 0.5$ m. A nearly incompressible neo-Hookean model is used with Young's modulus $E = 1.7 \times 10^7$ Pa, density $\rho_0 = 1.1 \times 10^3$ kg/m^3, Poisson's ratio $\nu = 0.499$ and $\alpha_{\text{CFL}} = 0.3$.

behaviours. In Figure 15, it is clear that the $\{\boldsymbol{p}, \boldsymbol{F}\}$ Upwind-SPH introduces spurious pressure modes. These non-physical pressure instabilities can be effectively removed by using alternative $\{\boldsymbol{p}, \boldsymbol{F}, J\}$ and $\{\boldsymbol{p}, \boldsymbol{F}, \boldsymbol{H}, J\}$ stabilised schemes. For completeness, Figures 16 and 17 show a sequence of deformed states of the problem for a relatively long period of time. Very smooth pressure field is observed surrounding the holes of the perforated block.

7.2.3. Taylor impact plasticity

Previously presented in References [27, 38, 42], a copper bar of initial length $L = 0.0324$ m and of initial radius $r = 0.0032$ m impacts against a rigid wall with a dropping velocity of 227 m/s, as shown in Figure 18. The main objective of this benchmark problem is to assess the performance of the proposed mesh-free algorithm in capturing large plastic deformations with application to metal forming [43]. A von Mises hyperelastic-plastic material with isotropic hardening is chosen for the simulation of this problem. The material parameters are Young's modulus $E = 117$ GPa, density $\rho_0 = 8.930 \times 10^3$ kg/m^3, Poisson's ratio $\nu = 0.35$, yield stress $\bar{\tau}_y^0 = 0.4$ GPa and hardening modulus $H = 0.1$ GPa. Figure 19 shows the contours of both plastic strain and pressure at eight different time instants. Extremely smooth pressure field is observed. For verification purposes, the final radius of the copper bar at time $t = 80\mu s$ predicted by the $\{\boldsymbol{p}, \boldsymbol{F}\}$ Upwind-SPH algorithm is shown in Table 2, benchmarked against other published numerical results [15, 27, 38]. As shown in References [15, 16], the solutions obtained using the standard linear 4-noded tetrahedra (being widely used in commercial software) typically suffers from volumetric locking and pressure instabilities. The new mesh-free method clearly circumvents these issues.

Table 2: Final radii of copper bar at $t = 80\mu s$. Results obtained using the proposed $\{\boldsymbol{p}, \boldsymbol{F}\}$ Upwind-SPH mesh-free algorithm, benchmarked against other published methodologies.

Method	Final radius (cm)
Standard 4-Noded Tetrahedra [15]	0.555
Under-integrated 8-Noded Hexahedra [15]	0.695
Average Nodal Pressure 4-Noded Tetrahedra [15]	0.699
Jameson-Schmidt-Turkel Vertex Centred FVM [38]	0.698
Petrov-Galerkin FEM [27]	0.700
Upwind Cell Centred FVM [42]	0.700
Upwind-SPH mesh-free method	**0.689**

7.3. Robustness

7.3.1. Twisting column

In order to examine the robustness of the algorithm, the challenging twisting column example previously explored in References [1, 2, 42] is now considered (see Figure 20). The problem is initialised with a sinusoidal angular velocity field relative to the origin given by $\boldsymbol{\omega}_0 = [0, \Omega \sin(\pi Y/2L), 0]^T$, where $\Omega = 105$ rad/s and $L = 6$ m is the length of the column. A nearly incompressible neo-Hookean material is considered and the material parameters are Young's modulus $E = 1.7 \times 10^7$ Pa, density $\rho_0 = 1.1 \times 10^3$ kg/m^3 and Poisson's ratio $\nu = 0.4995$.

A particle refinement study is shown in Figure 21. Interestingly, both the deformation and pressure resolution obtained are practically identical, showing optimal convergence for the

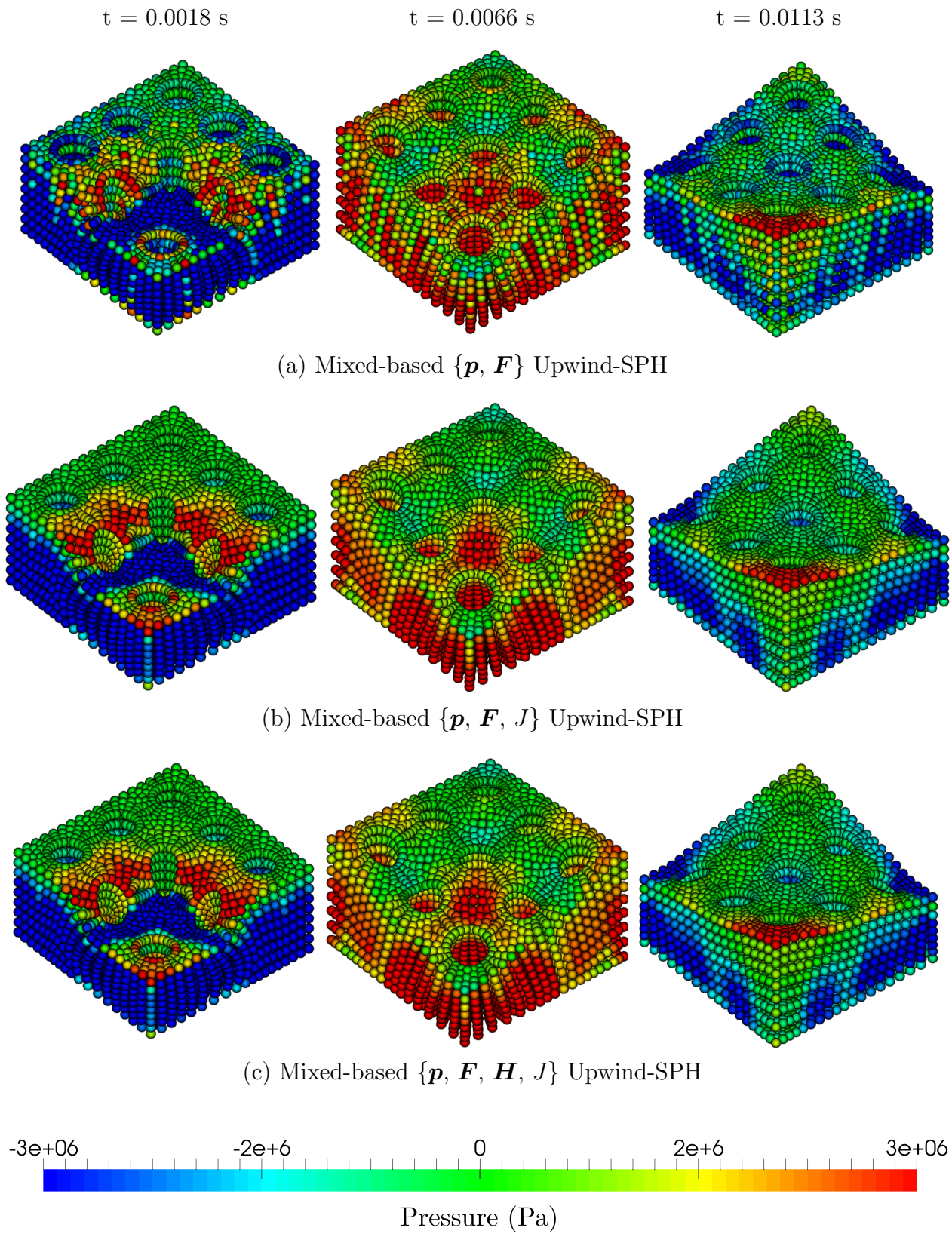

(a) Mixed-based $\{\boldsymbol{p}, \boldsymbol{F}\}$ Upwind-SPH

(b) Mixed-based $\{\boldsymbol{p}, \boldsymbol{F}, J\}$ Upwind-SPH

(c) Mixed-based $\{\boldsymbol{p}, \boldsymbol{F}, \boldsymbol{H}, J\}$ Upwind-SPH

Figure 15: Punch test. A sequence of deformed configurations using the mixed-based (a) $\{\boldsymbol{p}, \boldsymbol{F}\}$, (b) $\{\boldsymbol{p}, \boldsymbol{F}, J\}$ and (c) $\{\boldsymbol{p}, \boldsymbol{F}, \boldsymbol{H}, J\}$ Upwind-SPH. Results obtained with velocity field $\boldsymbol{v}_0 = -V[0, 0, (Z/H)]^T$ where $V = 250$ m/s and $H = 0.5$ m. A nearly incompressible neo-Hookean constitutive model is employed with Young's modulus $E = 1.7 \times 10^7$ Pa, density $\rho_0 = 1.1 \times 10^3$ kg/m^3, Poisson's ratio $\nu = 0.499$ and $\alpha_{\text{CFL}} = 0.3$.

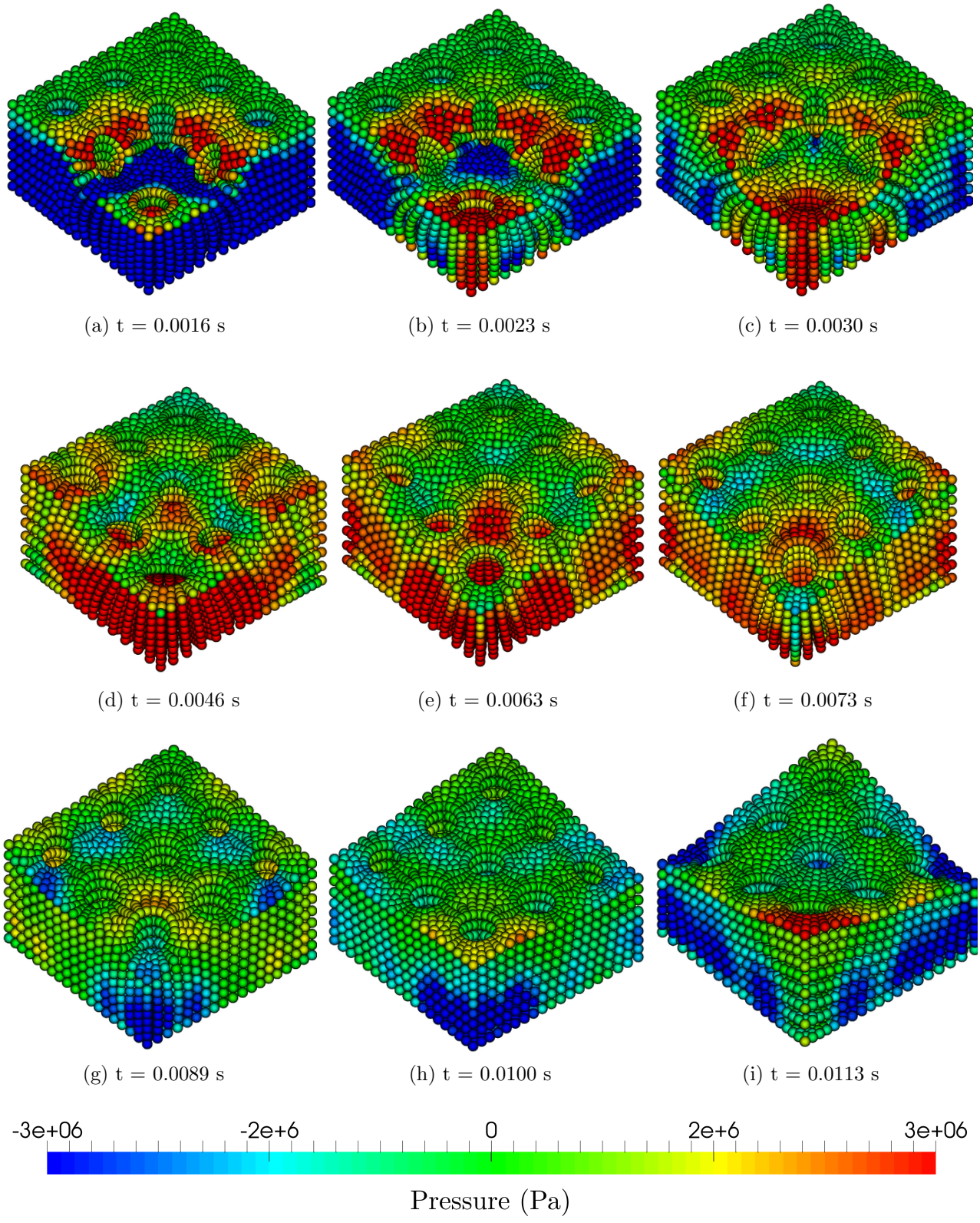

Figure 16: Punch test. A sequence of deformed configurations using the mixed-based $\{\boldsymbol{p}, \boldsymbol{F}, \boldsymbol{H}, J\}$ Upwind-SPH. Results obtained with velocity field $\boldsymbol{v}_0 = -V[0, 0, (Z/H)]^T$ where $V = 250$ m/s and $H = 0.5$ m. A nearly incompressible neo-Hookean constitutive model is employed with Young's modulus $E = 1.7 \times 10^7$ Pa, density $\rho_0 = 1.1 \times 10^3$ kg/m^3, Poisson's ratio $\nu = 0.499$ and $\alpha_{\text{CFL}} = 0.3$.

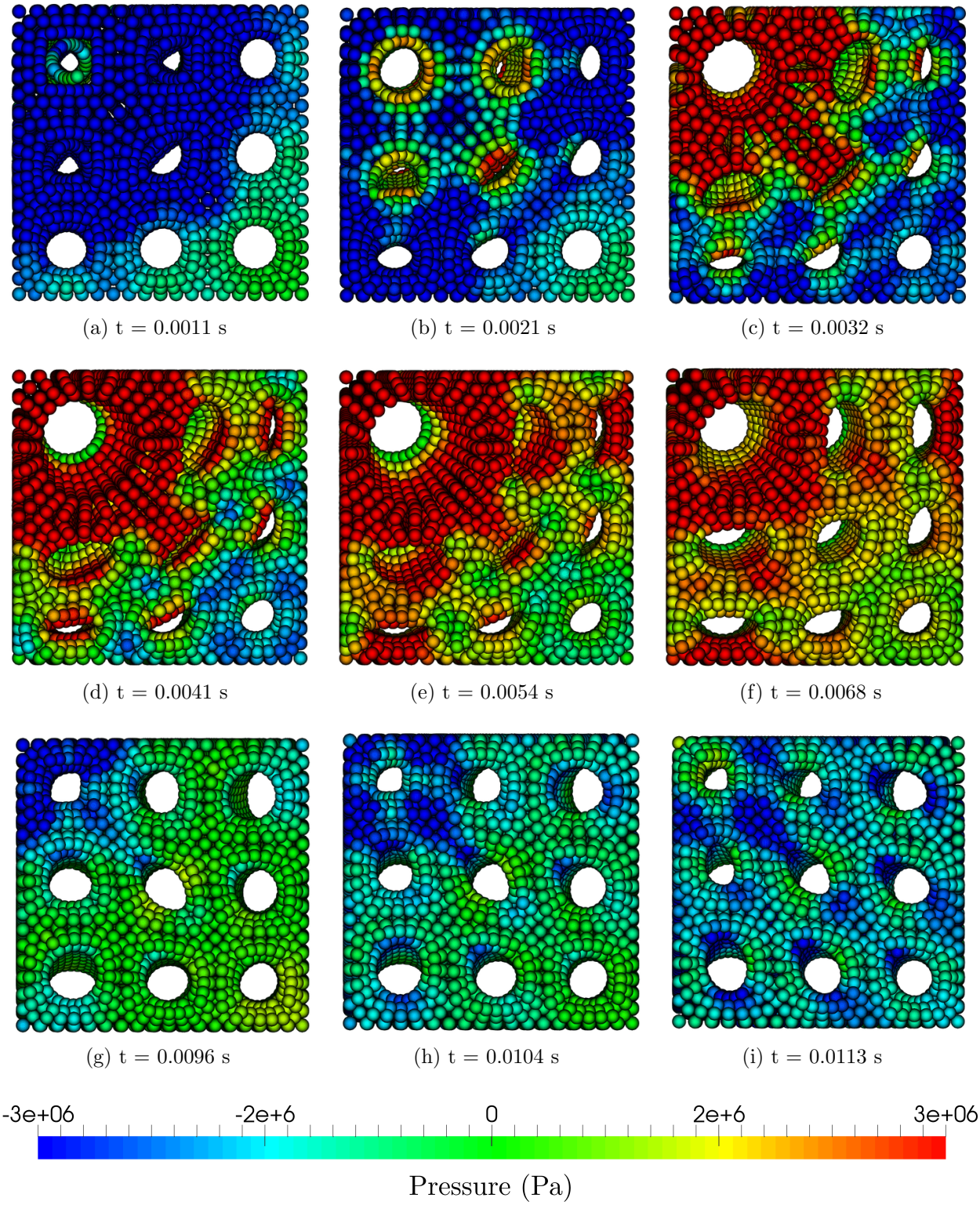

Figure 17: Punch test. A sequence of deformed configurations (emphasising bottom view) using the mixed-based $\{\boldsymbol{p}, \boldsymbol{F}, \boldsymbol{H}, J\}$ Upwind-SPH. Results obtained with velocity field $\boldsymbol{v}_0 = -V[0, 0, (Z/H)]^T$ where $V = 250$ m/s and $H = 0.5$ m. A nearly incompressible neo-Hookean constitutive model is employed with Young's modulus $E = 1.7 \times 10^7$ Pa, density $\rho_0 = 1.1 \times 10^3$ kg/m^3, Poisson's ratio $\nu = 0.499$ and $\alpha_{\text{CFL}} = 0.3$.

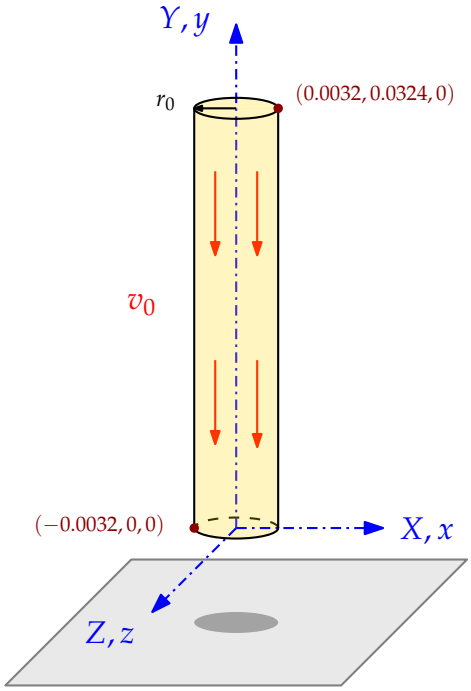

Figure 18: Taylor bar configuration

proposed method. It is also interesting to notice how the methodology preserves perfect axial rotation without introducing out-of-axis characteristics. This can be easily shown in Figure 22 by monitoring the evolution of the horizontal velocity and horizontal displacement components at point $\boldsymbol{X} = [0.5, 0.5, 6]^T$ m, both within zero machine accuracy. For benchmarking purposes, Figure 23 depicts a comparison of the new Upwind-SPH methodology against the recently proposed JST-SPH [1], SUPG-SPH [2] mesh-free methods and other in-house mixed-based methodologies. All of the schemes described above produce very similar results in terms of deformed shape and pressure field.

In comparison to the Upwind-SPH and SUPG-SPH schemes, it is clear that the JST-SPH (see Figure 23c) requires a considerably larger number of particles in order to capture the correct deformation pattern of the column. The results simulated using the SUPG-SPH (see Figure 23b) are in good agreement with the Upwind-SPH scheme (see Figure 23a). However, the SUPG-SPH method requires the generation of a secondary set of particles for the evaluation of the SUPG stabilisation, thus resulting in a greater computational cost.

The problem becomes significantly more challenging by increasing the initial angular velocity now to $\Omega = 200\,\text{rad/s}$ with a Poisson's ratio of $\nu = 0.4995$. A refinement study is also carried out in Figure 24 using a sequentially refined number of particles of $5 \times 5 \times 30$, $6 \times 6 \times 36$ and $7 \times 7 \times 42$. Notably, the number of twists shown in the column is captured extremely well even with a small number of particles. As illustrated in the top view of the simulation of Figure 24, no out-of-plane deformation can be observed.

Finally, we can further examine the robustness of the algorithm by increasing the value of Poisson's ratio to the limit such that $\nu \approx 0.5$. Its main objective is to show the efficiency of the artificial compressibility approach (see Section 5) in comparison to the explicit Upwind-SPH, especially in problems characterised by nearly or truly incompressible behaviours. Figure 25 shows the qualitative comparison between those two approaches. As expected, the artificial compressibility algorithm introduces a larger numerical dissipation due to the use of the (con-

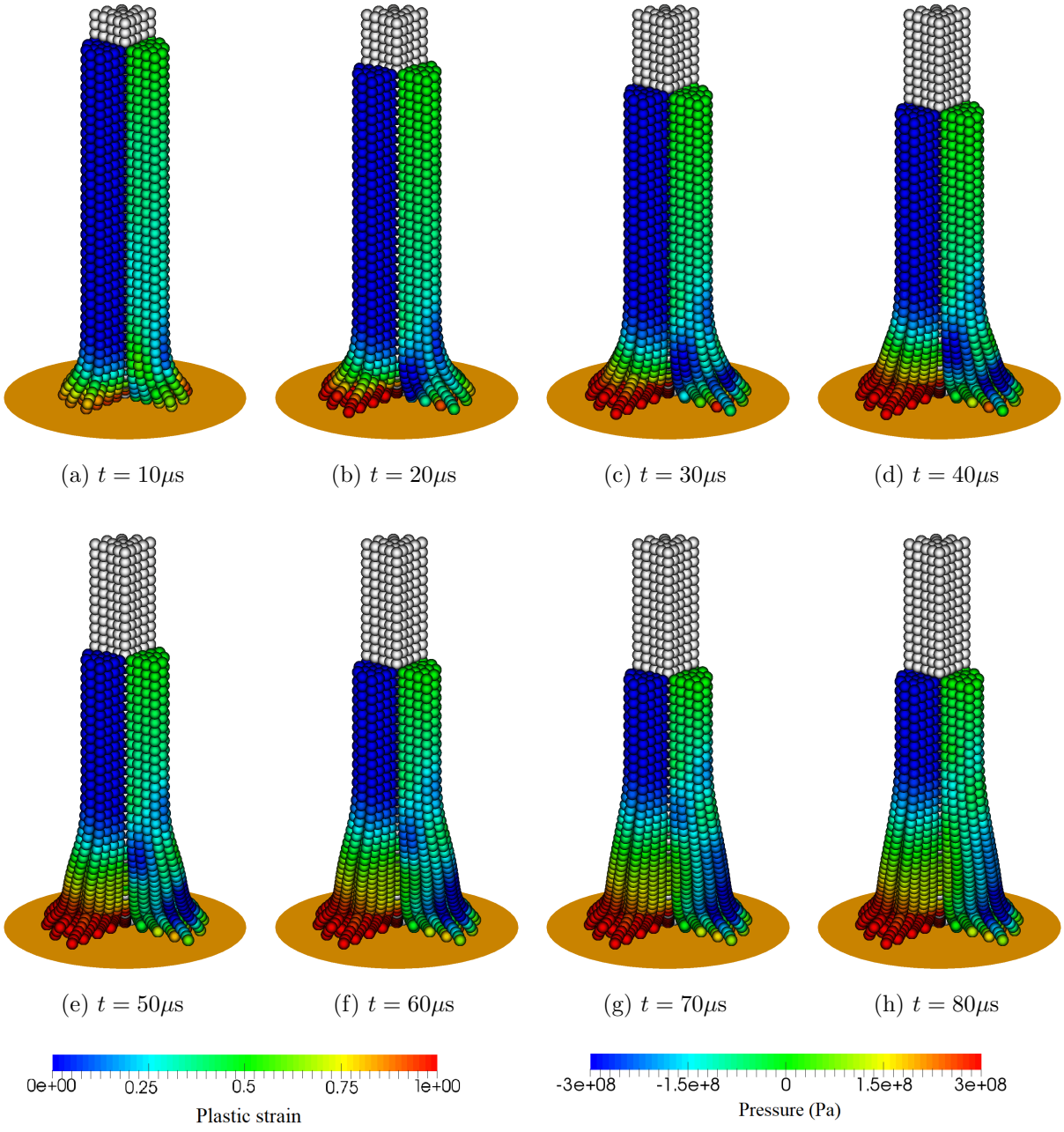

(a) $t = 10\mu$s (b) $t = 20\mu$s (c) $t = 30\mu$s (d) $t = 40\mu$s

(e) $t = 50\mu$s (f) $t = 60\mu$s (g) $t = 70\mu$s (h) $t = 80\mu$s

Figure 19: Taylor impact. Time evolution of plastic strain in the left quarter and pressure distribution in the right quarter of the domain along with the deformation. Results obtained using the proposed $\{\boldsymbol{p}, \boldsymbol{F}\}$ Upwind-SPH algorithm with dropping velocity $\boldsymbol{v}_0 = (0, -227, 0)^T$ m/s. A hyperelastic-plastic constitutive model is employed with Young's modulus $E = 117$ GPa, density $\rho_0 = 8930$ kg/m^3, Poisson's ratio $\nu = 0.35$, yield stress $\bar{\tau}_y^0 = 0.4$ GPa, hardening modulus $H = 0.1$ GPa and $\alpha_{\text{CFL}} = 0.3$.

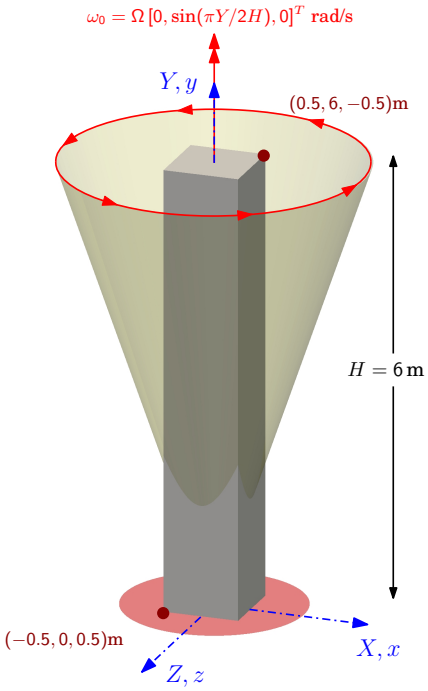

Figure 20: Twisting column problem setup

servative) Laplacian viscosity term described in (58). A particle refinement study is carried out in Figure 26, with a progressive level of refinement. It is remarkable that the deformation pattern predicted with a small number of particles agrees extremely well with those results obtained using a fine discretisation. The accuracy of the pressure contour is clearly enhanced as we increase the number of particles. Figure 27 shows the importance of adding (particle based) pseudo viscosity term to the artificial compressibility approach, with the primary aim to speed up the iterative process of the algorithm. As presented in Figure 27, the use of viscosity term dramatically reduces the number of iterations required for convergence within the pseudo time integration when solving truly incompressible solids.

7.3.2. Complex geometry

In the last example of this paper, we demonstrate the robustness of the proposed SPH algorithm on a complex geometry displayed in Figure 28. As reported in Reference [61], the geometry used in this example is a simplified version of a cardiovascular stent used in biomedical applications. The structure has an initial outer diameter of 20 mm, a thickness of 0.5 mm and a total length of 20 mm. The diameter of every hole is 2 mm. In this problem, we study the deformation pattern of this stent-like structure by applying a velocity field at the top and bottom of the structure, described as follows

$$\boldsymbol{v}_0 = \begin{cases} \left[0, 0, -\frac{ab\gamma}{(\gamma+1)^2}\right]^T & \text{if } t \leq 0.03 \text{ s} \\ \mathbf{0} & \text{otherwise} \end{cases} ; \qquad \gamma = \exp\left[a(c-t)\right], \tag{60}$$

where $a = 800$, $b = 0.006$ and $c = 0.015$. Due to the presence of three symmetry planes, only one eighth of the problem is solved with appropriate boundary conditions. The structure is made of a nearly incompressible neo-Hookean material with density $\rho = 1100$ kg/m^3, Young's Modulus $E = 17$ MPa and Poisson's ratio $\nu = 0.45$. Figure 29 shows the overall deformation of a structure at time $t = 0.0216$ s. It is remarkable that the pressure is extremely well captured

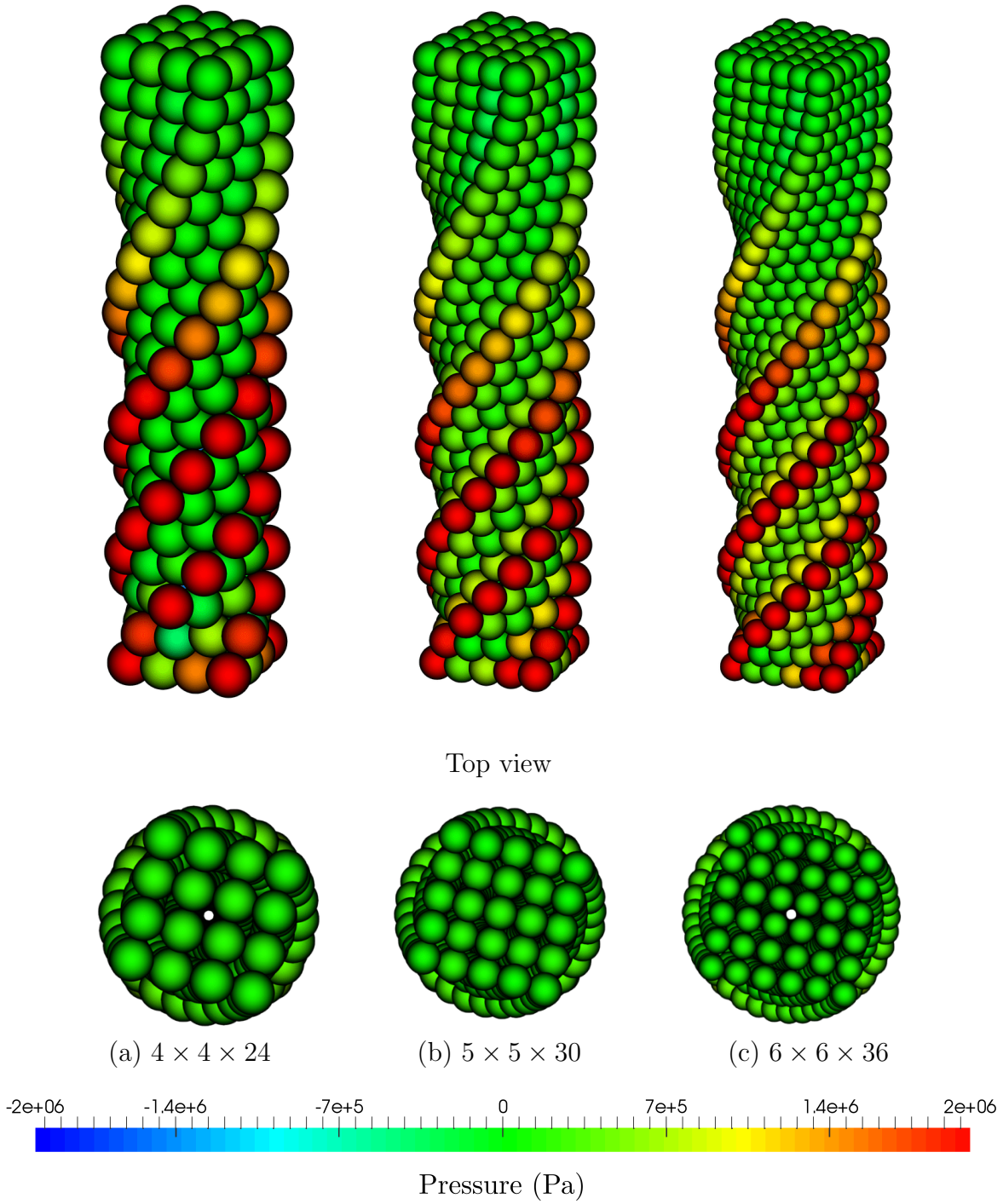

Figure 21: Twisting column. A sequence of particle refinement using the mixed-based $\{\boldsymbol{p}, \boldsymbol{F}, \boldsymbol{H}, J\}$ Upwind-SPH at time step $t = 0.1$s: (a) $4 \times 4 \times 24$, (b) $5 \times 5 \times 30$, and (c) $6 \times 6 \times 36$ particles. Results obtained with an angular velocity field $\boldsymbol{\omega}_0 = [0, \Omega \sin(\pi Y/2L), 0]$ where $\Omega = 105$ rad/s and $L = 6$ m. A nearly incompressible neo-Hookean constitutive model is employed with Young's modulus $E = 1.7 \times 10^7$ Pa, density $\rho_0 = 1.1 \times 10^3$ kg/m^3, Poisson's ratio $\nu = 0.4995$ and $\alpha_{\text{CFL}} = 0.3$.

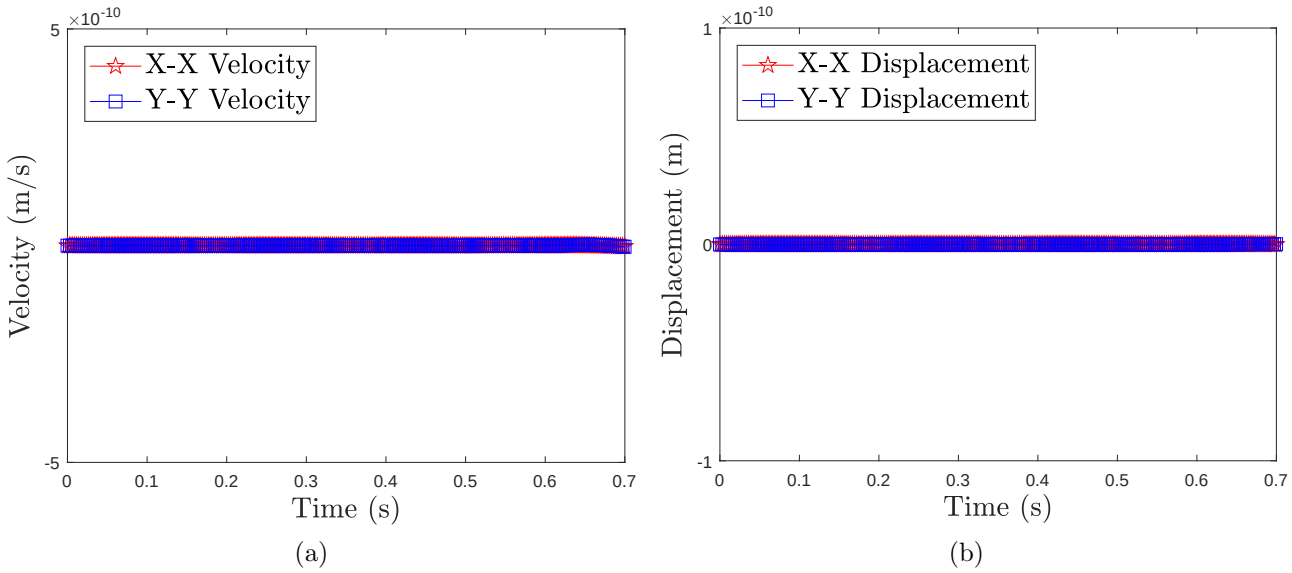

Figure 22: Twisting column. Time evolution of the components of (a) Velocity and (b) Displacement at point $\boldsymbol{X} = [0.5, 0.5, 6]^T$ m via the mixed-based $\{\boldsymbol{p}, \boldsymbol{F}, \boldsymbol{H}, J\}$ Upwind-SPH algorithm. A nearly incompressible neo-Hookean constitutive model is employed with Young's modulus $E = 1.7 \times 10^7$ Pa, density $\rho_0 = 1.1 \times 10^3$ kg/m^3, Poisson's ratio $\nu = 0.4995$ and $\alpha_{\text{CFL}} = 0.3$.

even with a minimum of two particles across the thickness. As can be seen in Figure 30, the mixed-based $\{\boldsymbol{p}, \boldsymbol{F}, \boldsymbol{H}, J\}$ Upwind-SPH method produces reliable results that are freed from zero energy modes. This will open up interesting possibilities for modelling in the field of biomechanics [62, 63], where this consideration is very relevant.

8. Conclusions

This paper presents a new Upwind Smooth Particle Hydrodynamics (Upwind-SPH) computational methodology for the analysis of nearly and truly incompressible large deformations in explicit fast solid dynamics. The methodology is established starting from a mixed-based system of Total Lagrangian first order conservation laws, where the linear momentum $\boldsymbol{p}$ conservation law is solved along with conservation equations for the extended set of geometric strain measures $\{\boldsymbol{F}, \boldsymbol{H}, J\}$.

In this work, a Riemann solver based spatial discretisation has been employed for stabilisation, offering a series of advantages over the recently proposed JST-SPH method [1] and SUPG-SPH method [2]. First, the nature of the Riemann based upwinding stabilisation does not explicitly rely on the use of any artificial stabilisation parameters. This differs from the JST-SPH and SUPG-SPH methodologies, as the former requires the evaluation of user-defined harmonic and bi-harmonic operators and the latter requires the selection of a number of user-defined stabilisation parameters for the evaluation of the SUPG stabilisation. Second, the Upwind-SPH framework is more accurate than its JST-SPH counterpart, and its accuracy is comparable to that of the SUPG-SPH but with a reduced computational cost.

It has also been shown that the resulting Upwind-SPH algorithm overcomes a number of numerical difficulties posed by the classical SPH method, namely non-physical hydrostatic pressure fluctuations, hour-glassing and numerical issues associated with conservation, consistency, long term instability and convergence. As a result, the new algorithm provides a good balance

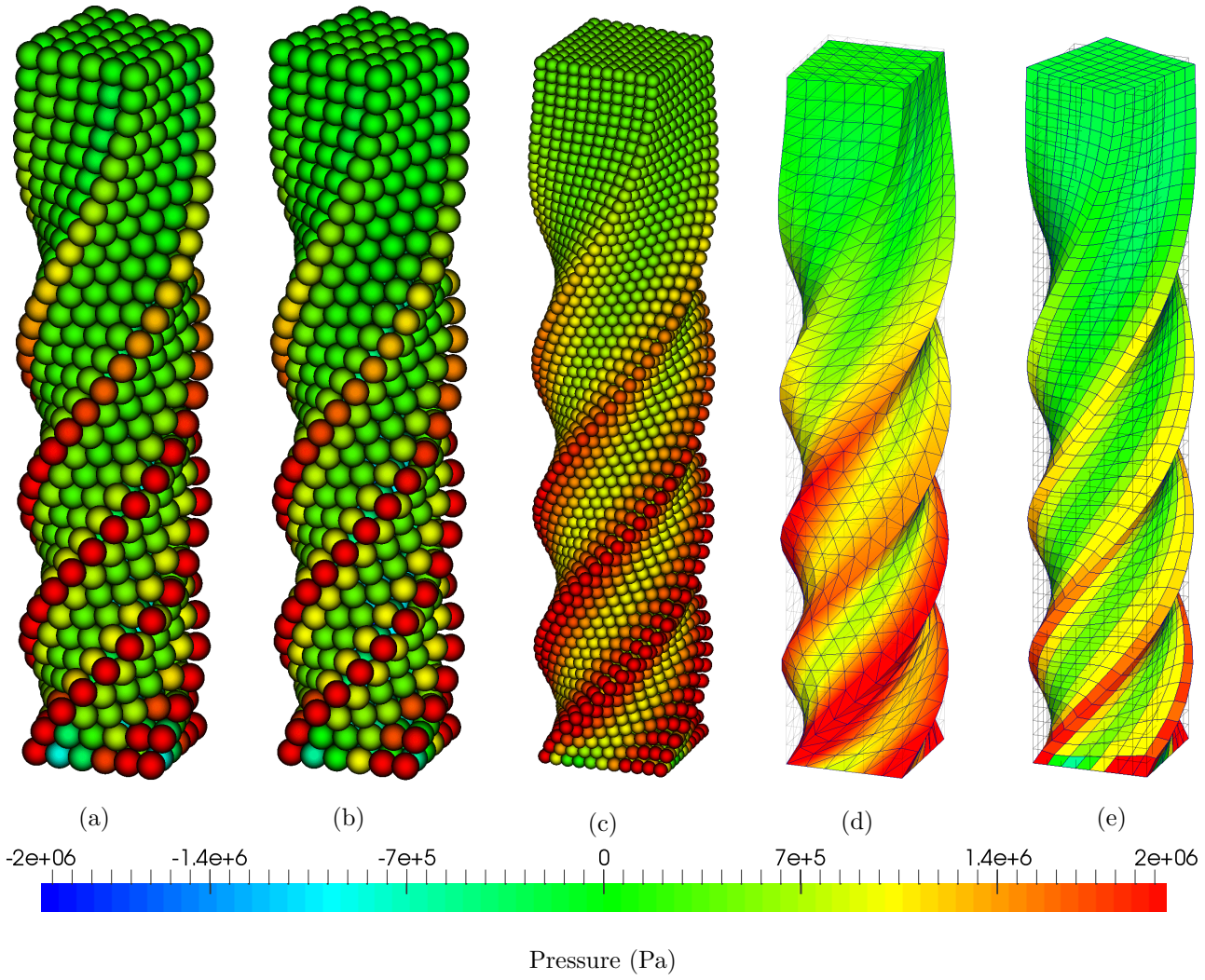

Figure 23: Twisting column. Comparison of deformed shapes plotted with pressures at time $t = 0.1$ s using: (a) Mixed-based $\{\boldsymbol{p}, \boldsymbol{F}\}$ Upwind-SPH; (b) Mixed-based $\{\boldsymbol{p}, \boldsymbol{F}, \boldsymbol{H}, J\}$ SUPG-SPH-H1 ($\tau_{\boldsymbol{F}} = \Delta t$, $\xi_{\boldsymbol{F}} = 0.2$, $\tau_{\boldsymbol{p}} = 0.1\Delta t$); (c) Mixed-based $\{\boldsymbol{p}, \boldsymbol{F}\}$ JST-SPH ($\varepsilon_{\boldsymbol{p}}^{(2)} = 0$ and $\varepsilon_{\boldsymbol{p}}^{(4)} = \frac{1}{8}$); (d) PG-FEM [26]; and (e) Constrained-TOUCH [42]. Results obtained with an angular velocity field $\boldsymbol{\omega}_0 = [0, \Omega \sin(\pi Y/2L), 0]$ where $\Omega = 105$ rad/s and $L = 6$ m. A neo-Hookean material is used with density $\rho_0 = 1100$ kg/m^3, Young's modulus $E = 17$ MPa and Poisson's ratio $\nu = 0.495$.

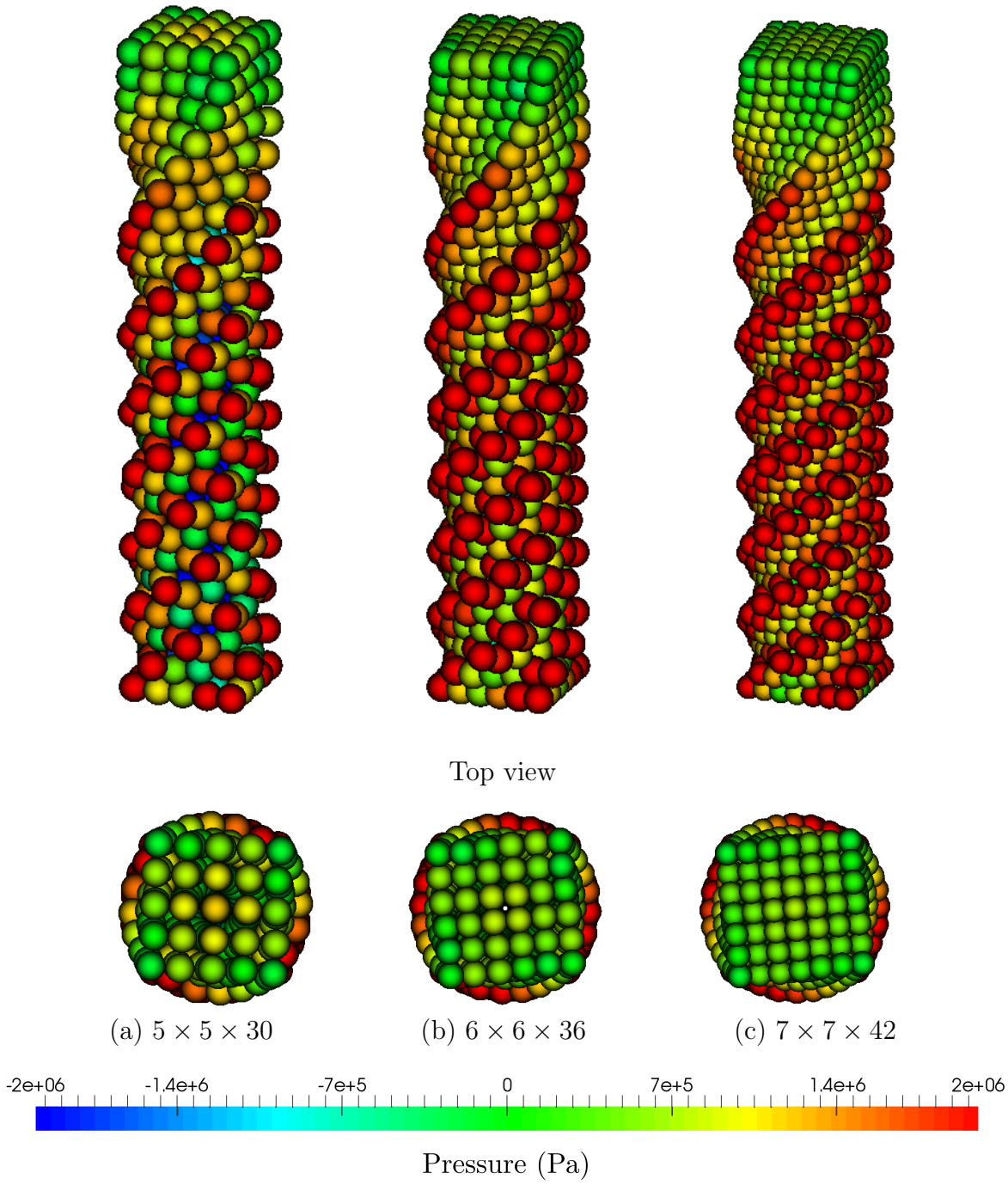

Figure 24: Twisting column. A sequence of particle refinement using the mixed-based $\{\boldsymbol{p}, \boldsymbol{F}, \boldsymbol{H}, J\}$ Upwind-SPH at time step $t = 0.1$ s: (a) $5 \times 5 \times 30$, (b) $6 \times 6 \times 36$, and (c) $7 \times 7 \times 42$ particles. Results obtained with an angular velocity field $\boldsymbol{\omega}_0 = [0, \Omega \sin(\pi Y/2L), 0]$ where $\Omega = 200$ rad/s and $L = 6$ m. A nearly incompressible neo-Hookean constitutive model is employed with Young's modulus $E = 1.7 \times 10^7$ Pa, density $\rho_0 = 1.1 \times 10^3$ kg/m^3, Poisson's ratio $\nu = 0.4995$ and $\alpha_{\text{CFL}} = 0.3$.

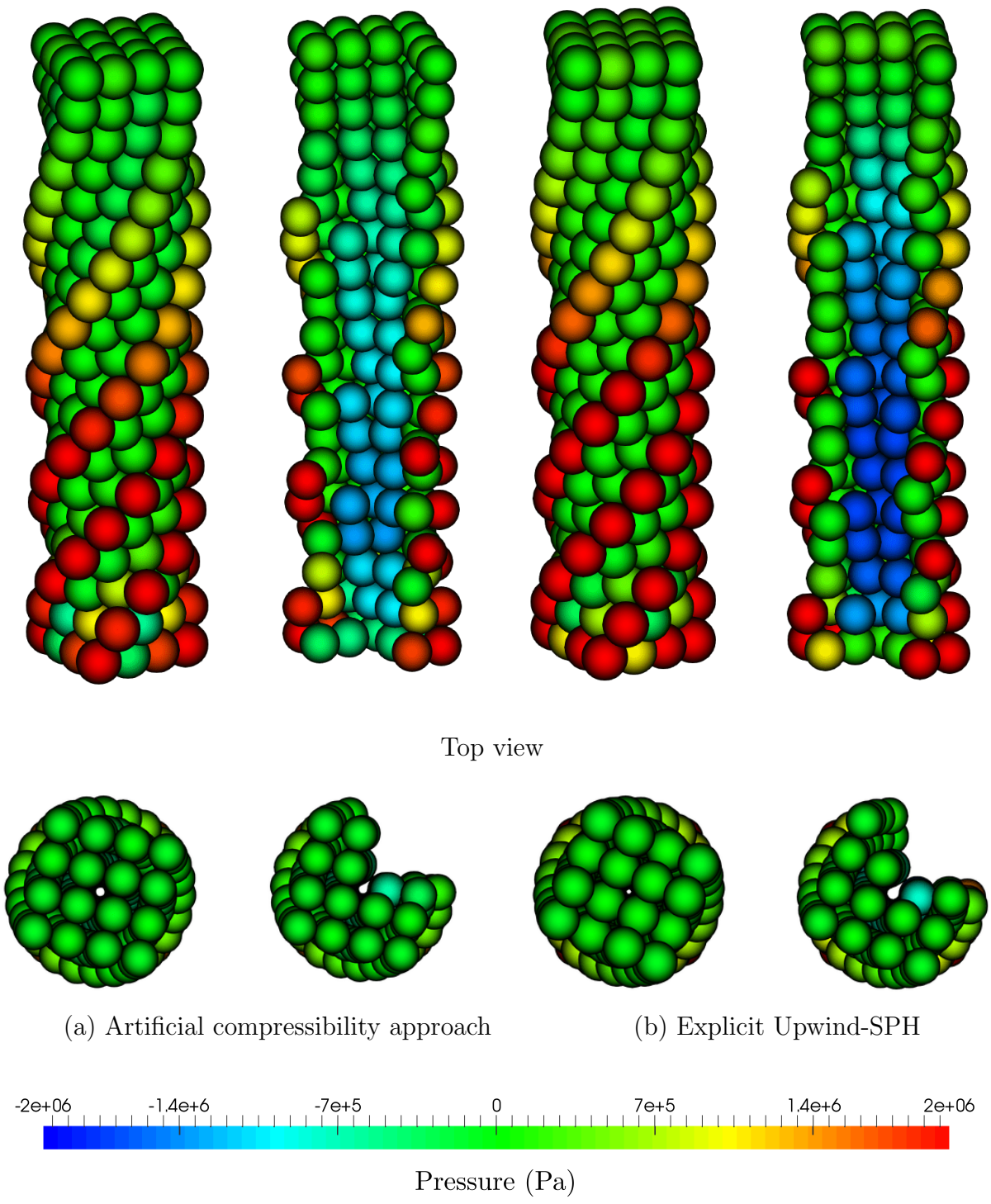

Figure 25: Twisting column. A comparison between (a) $\{\boldsymbol{p},\ \boldsymbol{F},\ \boldsymbol{H}, p\}$ artificial compressibility approach and (b) Explicit $\{\boldsymbol{p},\ \boldsymbol{F}, \boldsymbol{H}, J\}$ Upwind-SPH at time step $t = 0.1$s. Results obtained with an angular velocity field $\boldsymbol{\omega}_0 = [0, \Omega \sin(\pi Y/2L), 0]$ where $\Omega = 105$ rad/s and $L = 6$ m. A nearly incompressible neo-Hookean constitutive model is employed with Young's modulus $E = 1.7 \times 10^7$ Pa, density $\rho_0 = 1.1 \times 10^3$ kg/m^3, Poisson's ratio $\nu = 0.4999$ and $\alpha_{\text{CFL}} = 0.3$.

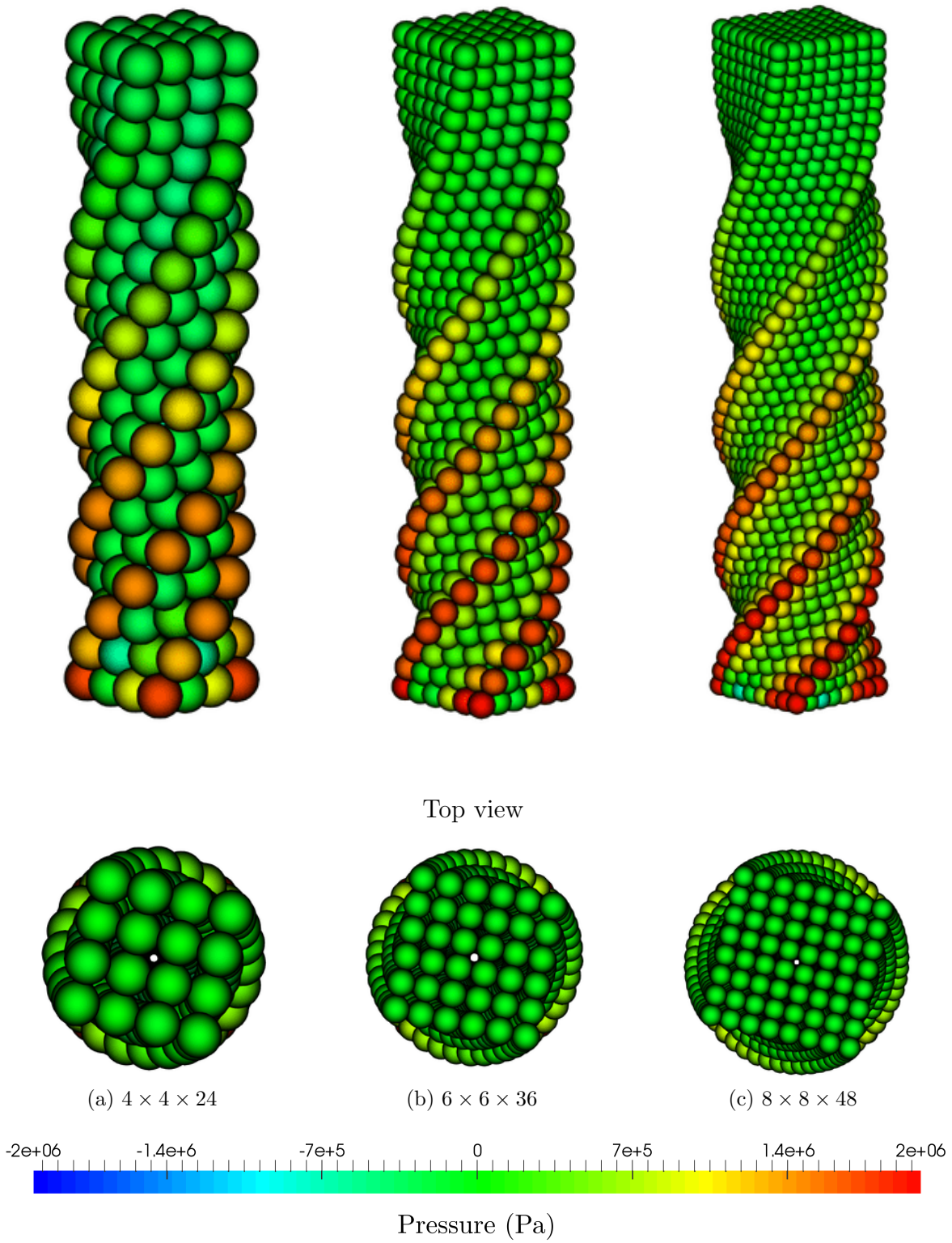

Figure 26: Twisting column. A sequence of particle refinement using the mixed-based $\{\boldsymbol{p}, \boldsymbol{F}\}$ Upwind-SPH through artificial compressibility at time step $t = 0.1$s: (a) $4 \times 4 \times 24$, (b) $6 \times 6 \times 36$, and (c) $8 \times 8 \times 48$ particles. Results obtained with an angular velocity field $\boldsymbol{\omega}_0 = [0, \Omega \sin(\pi Y/2L), 0]$ where $\Omega = 105$ rad/s and $L = 6$ m. A truly incompressible neo-Hookean constitutive model is employed with Young's modulus $E = 1.7 \times 10^7$ Pa, density $\rho_0 = 1.1 \times 10^3$ kg/m^3, Poisson's ratio $\nu = 0.5$ and $\alpha_{\text{CFL}} = 0.3$.

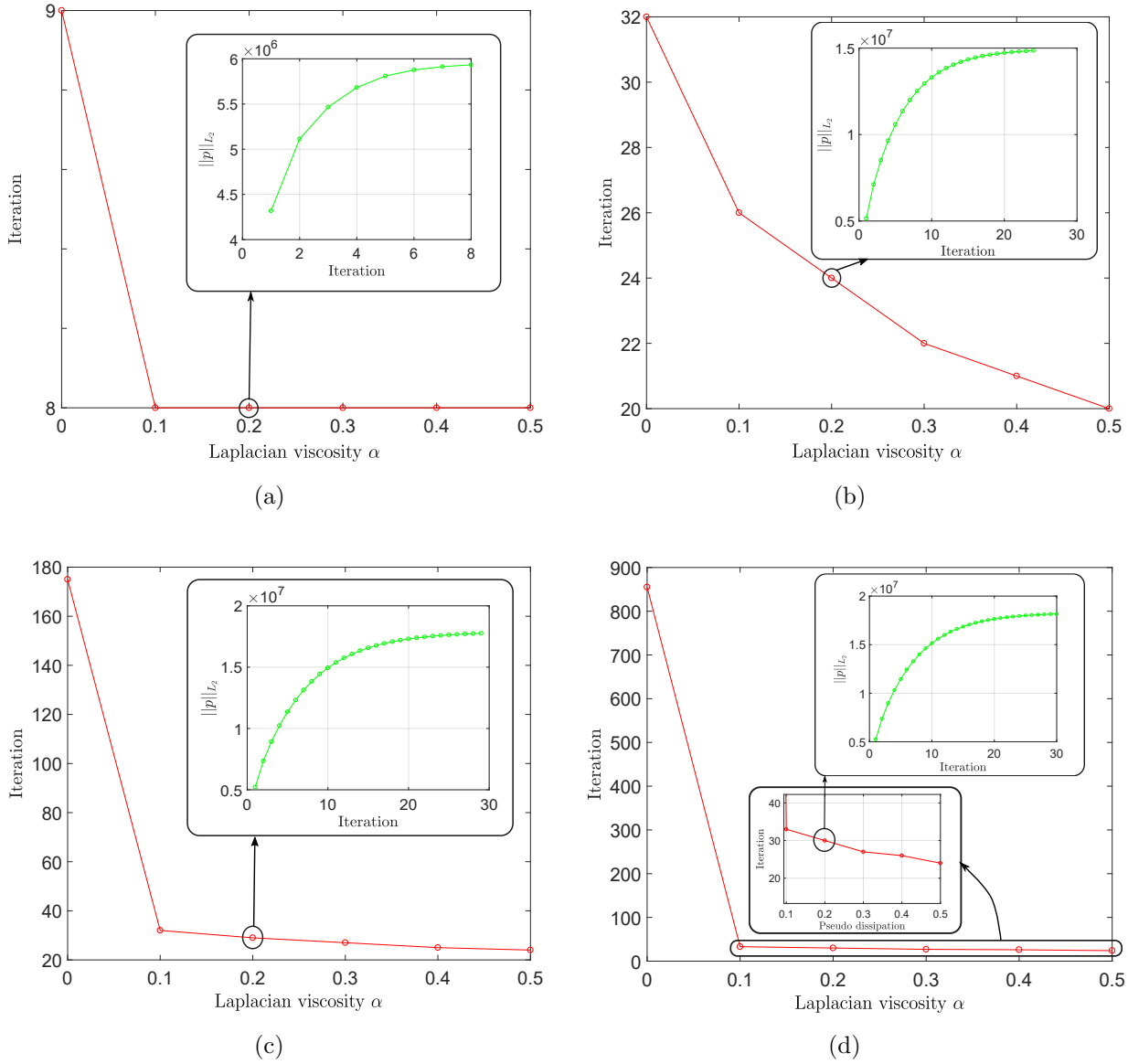

Figure 27: Twisting column. The effect of incorporating Laplacian viscosity (54) to the artificial compressibility approach with the primary aim to enhance the iterative process of the algorithm in various scenarios: (a) $\nu = 0.499$, (b) $\nu = 0.4999$, (c) $\nu = 0.49999$ and (d) $\nu = 0.5$. Results obtained for the first step of Runge-Kutta time integrator with an angular velocity field $\boldsymbol{\omega}_0 = [0, \Omega \sin(\pi Y/2L), 0]$ where $\Omega = 105$ rad/s and $L = 6$ m. The green curve represents the number of iterations required to achieve steady state convergence in pseudo-time for a fixed Laplacian viscosity α. A neo-Hookean constitutive model is employed with Young's modulus $E = 1.7 \times 10^7$ Pa, density $\rho_0 = 1.1 \times 10^3$ kg/m^3 and $\alpha_{\text{CFL}} = 0.3$.

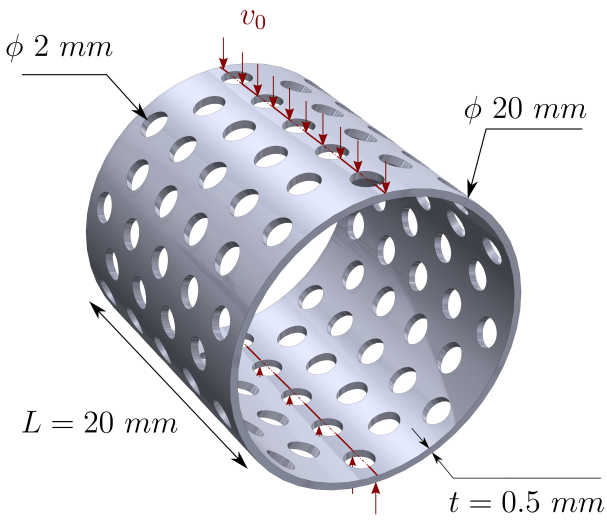

Figure 28: Stent-like structure [61]. The Computer Aided Design (CAD) file can be downloaded from GrabCAD.

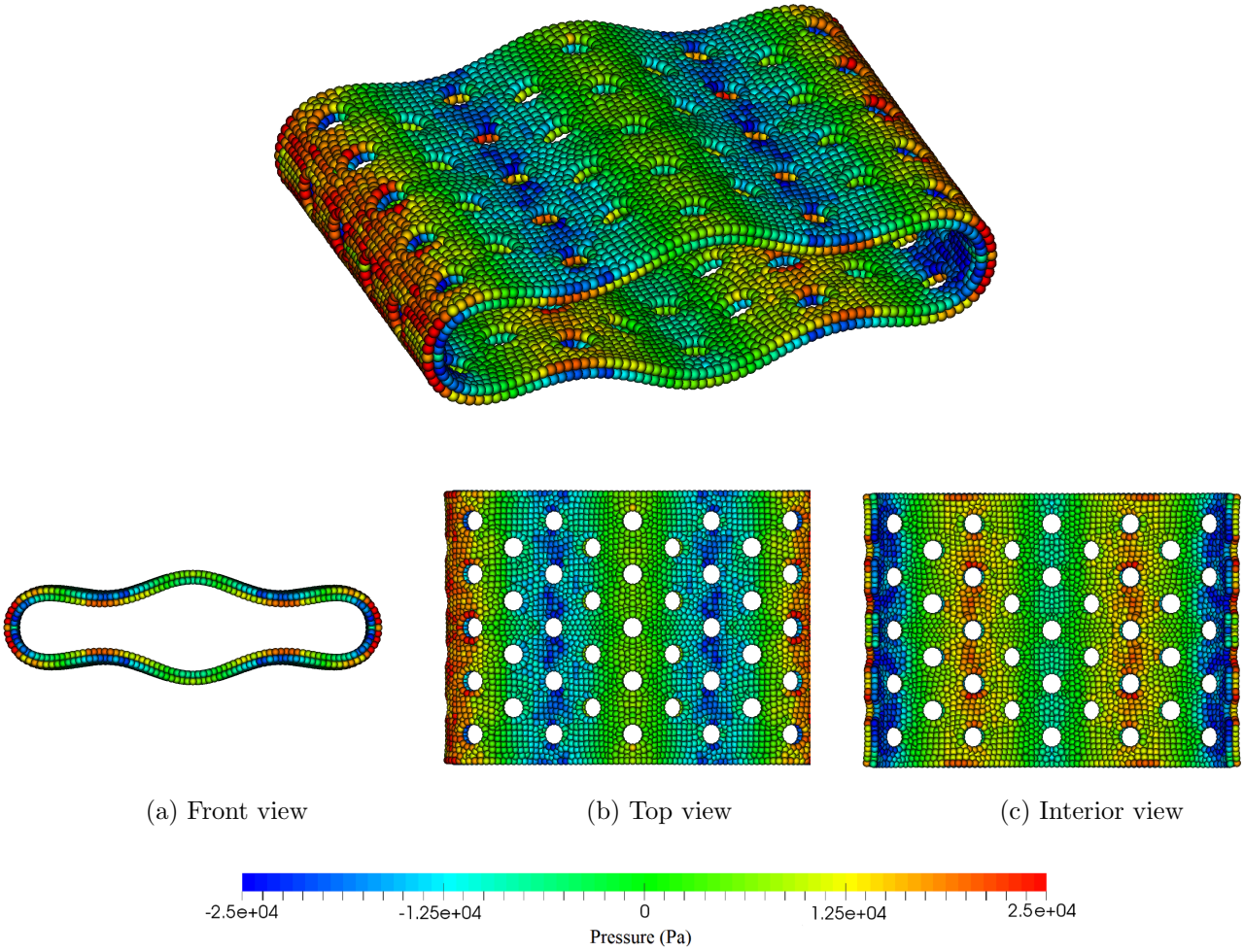

(a) Front view (b) Top view (c) Interior view

Figure 29: Stent-like structure. Deformed configuration of the structure at $t = 0.0216$ s simulated using the mixed-based $\{\boldsymbol{p}, \boldsymbol{F}, \boldsymbol{H}, J\}$ Upwind-SPH algorithm. A nearly incompressible neo-Hookean constitutive model is employed with Young's modulus $E = 0.9$ MPa, density $\rho_0 = 1000$ kg/m^3, Poisson's ratio $\nu = 0.45$ and $\alpha_{\text{CFL}} = 0.3$.

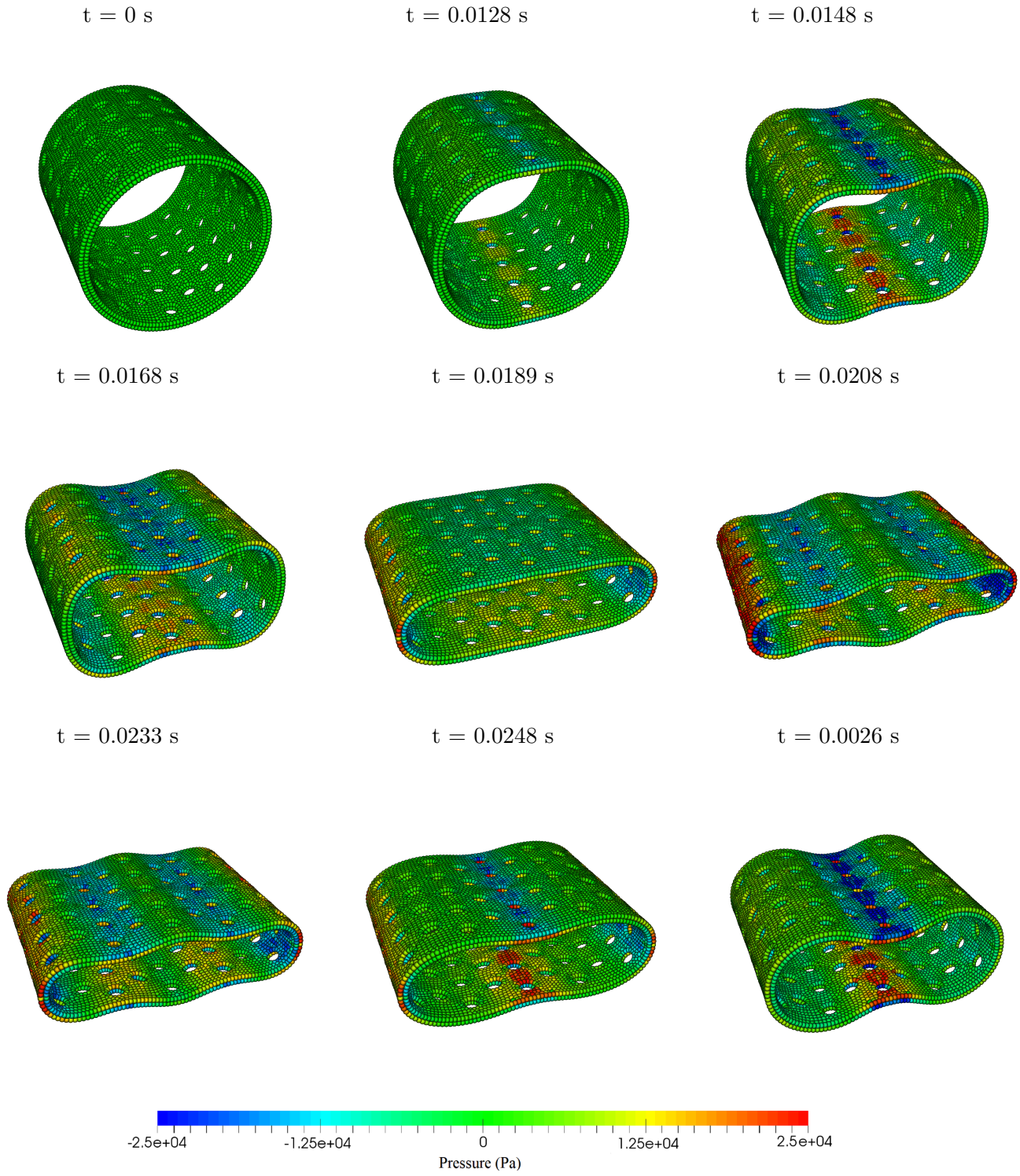

Figure 30: Stent-like structure. A sequence of deformed configurations using the mixed-based $\{\boldsymbol{p}, \boldsymbol{F}, \boldsymbol{H}, J\}$ Upwind-SPH algorithm. A nearly incompressible neo-Hookean constitutive model is employed with Young's modulus $E = 0.9$ MPa, density $\rho_0 = 1000$ kg/m^3, Poisson's ratio $\nu = 0.45$ and $\alpha_{\text{CFL}} = 0.3$.

between accuracy and speed of computation. In terms of computational efficiency, an adapted artificial compressibility approach has been formulated particularly useful when dealing with extremely large (or even infinite) wave speeds in the incompressible limit.

Finally, a comprehensive set of numerical examples has been presented in order to benchmark the results obtained against other numerical methodologies, including Finite Element Method [25–27, 30, 35], Finite Volume Method [3, 34, 38, 42] and Smooth Particle Hydrodynamics Method [1, 2]. Both velocities and (volumetric and deviatoric) stresses display equal second order of convergence, advantageous in those scenarios where stresses are of primary interest. The consideration of thermoelasticity within the current mesh-free computational framework is the next step of our work.

Acknowledgements
The authors gratefully acknowledge the financial support provided by the Sêr Cymru National Research Network for Advanced Engineering and Materials, United Kingdom. The third author acknowledges the financial support received through the European Commission EACEA Agency, Framework Partnership Agreement 2013-0043 Erasmus Mundus Action 1*b*, as a part of the EM Joint Doctorate Simulation in Engineering and Entrepreneurship Development (SEED).

Appendix A. von Mises plasticity model

The standard algorithm to ensure that the Kirchhoff stress satisfies a von Mises type of plastic constraint is summarised here for completeness in Algorithm 2.

Appendix B. Discrete angular momentum preserving algorithm

The resulting Upwind-SPH algorithm does not intrinsically fulfil conservation of angular momentum, since the strain measures $\{\boldsymbol{F}, \boldsymbol{H}, J\}$ are no longer exclusively obtained from the current geometry [42]. Specifically, the deformation gradient $\boldsymbol{F} \neq \boldsymbol{F}_{\boldsymbol{x}} := \boldsymbol{\nabla}_0 \boldsymbol{x}$, its co-factor $\boldsymbol{H} \neq \boldsymbol{H}_{\boldsymbol{x}} := \frac{1}{2}\boldsymbol{F}_{\boldsymbol{x}} \boldsymbol{\times} \boldsymbol{F}_{\boldsymbol{x}}$ and its Jacobian $J \neq J_{\boldsymbol{x}} := \det \boldsymbol{F}_{\boldsymbol{x}}$.

In this paper, and following the work of Jibran *et al.* [42], a monolithic discrete angular momentum projection algorithm is presented. Specifically, the local internal nodal force $\boldsymbol{T}_a$ is modified (in a least-square sense) in order to preserve the total angular momentum, whilst still ensuring the global conservation of linear momentum.

Following Reference [42], sufficient conditions for the global preservation of the discrete linear and angular momentum within a time step are enforced at each stage of the one-step two-stage Runge Kutta time integrator (40) described as:

$$\sum_a V_a \boldsymbol{T}_a^{\chi} = \boldsymbol{0}; \quad \sum_a V_a \mathscr{X}_a \times \boldsymbol{T}_a^{\chi} = \boldsymbol{0}; \quad \mathscr{X}_a = \begin{cases} \boldsymbol{x}_a^n, & \chi = n \\ \boldsymbol{x}_a^n + \frac{\Delta t}{2\rho_0}\left(\boldsymbol{p}_a^n + \boldsymbol{p}_a^{\star}\right), & \chi = \star \end{cases}; \tag{B.1}$$

where $\chi = \{n, \star\}$.

A least-square minimisation procedure is used to obtain a modified set of internal nodal forces $\hat{\boldsymbol{T}}_a$ that satisfy the above conditions (B.1). This can be achieved by computing the

Algorithm 2: Time update of first Piola Kirchoff stress tensor

Input : $\boldsymbol{F}^{n+1}, \left[\boldsymbol{C}_p^{-1}\right]^n, \varepsilon_p^n$
Output: $\boldsymbol{P}^{n+1}$

(1) Obtain Jacobian of deformation: $J_{\boldsymbol{F}}^{n+1} = \det\left(\boldsymbol{F}^{n+1}\right)$

(2) Evaluate pressure: $p^{n+1} = \kappa \frac{\ln\left(J_{\boldsymbol{F}}^{n+1}\right)}{J_{\boldsymbol{F}}^{n+1}}$

(3) Compute trial elastic left strain tensor: $\bar{\boldsymbol{b}}_e^{n+1} = \boldsymbol{F}^{n+1}\left[\boldsymbol{C}_p^{-1}\right]^n\left[\boldsymbol{F}^T\right]^{n+1}$

(4) Spectral decomposition of $\bar{\boldsymbol{b}}_e^{n+1}$: $\bar{\lambda}_{e,i}\ ,\ \bar{\boldsymbol{n}}_i \longleftarrow \bar{\boldsymbol{b}}_e^{n+1} = \sum_{i=1}^{3}\left(\bar{\lambda}_{e,i}\right)^2\left(\bar{\boldsymbol{n}}_i \otimes \bar{\boldsymbol{n}}_i\right)$

(5) Obtain trial deviatoric Kirchoff stress tensor:
$\bar{\boldsymbol{\tau}}' = \sum_{i=1}^{3}\bar{\tau}'_{ii}\left(\bar{\boldsymbol{n}}_i \otimes \bar{\boldsymbol{n}}_i\right), \qquad \bar{\tau}'_{ii} = 2\mu\ln\left(\bar{\lambda}_{e,i}\right) - \frac{2}{3}\mu\ln\left(J_{\boldsymbol{F}}^{n+1}\right)$

(6) Obtain yield criterion: $f\left(\bar{\boldsymbol{\tau}}', \varepsilon_p^n\right) = \sqrt{\frac{3}{2}(\bar{\boldsymbol{\tau}}' : \bar{\boldsymbol{\tau}}')} - \left(\tau_y^0 + H\varepsilon_p^n\right)$

(7) Compute direction vector and plastic multiplier:
if $f\left(\bar{\boldsymbol{\tau}}', \varepsilon_p^n\right) > 0$ **then**
Direction vector: $\boldsymbol{\upsilon}_i^{n+1} = \frac{\bar{\tau}'_{ii}}{\sqrt{\frac{2}{3}(\bar{\boldsymbol{\tau}}' : \bar{\boldsymbol{\tau}}')}}$
Plastic multiplier: $\Delta\gamma = \frac{f\left(\bar{\boldsymbol{\tau}}', \varepsilon_p^n\right)}{3\mu + H}$
else
$\boldsymbol{\upsilon}_i^{n+1} = \Delta\gamma = 0$
end

(8) Evaluate elastic stretch: $\lambda_{e,i}^{n+1} = \exp\left(\ln(\bar{\lambda}_{e,i}) - \Delta\gamma\,\boldsymbol{\upsilon}_i^{n+1}\right)$

(9) Set spatial normals: $\boldsymbol{n}_i^{n+1} = \bar{\boldsymbol{n}}_i$

(10) Compute Kirchoff stresss tensor:
$\boldsymbol{\tau}^{n+1} = \sum_{i=1}^{3}\tau_{ii}\left(\boldsymbol{n}_i^{n+1} \otimes \boldsymbol{n}_i^{n+1}\right)$
$\tau_{ii} = \tau'_{ii} + J_{\boldsymbol{F}}^{n+1}p^{n+1}, \qquad \tau'_{ii} = \left(1 - \frac{2\mu\Delta\gamma}{\sqrt{\frac{2}{3}(\bar{\boldsymbol{\tau}}' : \bar{\boldsymbol{\tau}}')}}\right)\bar{\tau}'_{ii}$

(11) Evaluate first Piola Kirchoff stress tensor: $\boldsymbol{P}^{n+1} = \boldsymbol{\tau}^{n+1}\left[\boldsymbol{F}^{-T}\right]^{n+1}$

(12) Update elastic left strain tensor: $\boldsymbol{b}_e^{n+1} = \sum_{i=1}^{3}\left(\lambda_{e,i}^{n+1}\right)^2\left(\boldsymbol{n}_i^{n+1} \otimes \boldsymbol{n}_i^{n+1}\right)$

(13) Compute plastic right Cauchy Green tensor: $\left[\boldsymbol{C}_p^{-1}\right]^{n+1} = \left[\boldsymbol{F}^{-1}\right]^{n+1}\boldsymbol{b}_e^{n+1}\left[\boldsymbol{F}^{-T}\right]^{n+1}$

(14) Update plastic strain: $\varepsilon_p^{n+1} = \varepsilon_p^n + \Delta\gamma$

minimum of the following functional [38, 42] (ignoring time arguments for brevity):

$$\begin{aligned}\Pi_{\boldsymbol{T}}(\hat{\boldsymbol{T}}_a, \boldsymbol{\lambda}_{\text{ang}}, \boldsymbol{\lambda}_{\text{lin}}) = \frac{1}{2}\sum_a V_a(\hat{\boldsymbol{T}}_a - \boldsymbol{T}_a)\cdot(\hat{\boldsymbol{T}}_a - \boldsymbol{T}_a) \\ - \boldsymbol{\lambda}_{\text{ang}}\cdot\left(\sum_a V_a \mathscr{X}_a \times \hat{\boldsymbol{T}}_a\right) - \boldsymbol{\lambda}_{\text{lin}}\cdot\left(\sum_a V_a \hat{\boldsymbol{T}}_a\right).\end{aligned} \tag{B.2}$$

After some simple algebra, a modified set of internal nodal forces $\hat{\boldsymbol{T}}_a$ arise:

$$\hat{\boldsymbol{T}}_a = \boldsymbol{T}_a + \boldsymbol{\lambda}_{\text{ang}} \times \mathscr{X}_a + \boldsymbol{\lambda}_{\text{lin}}. \tag{B.3}$$

The Lagrange multipliers $\{\boldsymbol{\lambda}_{\text{ang}}, \boldsymbol{\lambda}_{\text{lin}}\}$ are the solutions of the following system of equations

$$\begin{bmatrix} \sum_a V_a\left[(\mathscr{X}_a\cdot\mathscr{X}_a)\boldsymbol{I} - \mathscr{X}_a\otimes\mathscr{X}_a\right] & \sum_a V_a\hat{\mathscr{X}}_a \\ \sum_a V_a\hat{\mathscr{X}}_a & -\sum_a V_a \end{bmatrix}\begin{bmatrix} \boldsymbol{\lambda}_{\text{ang}} \\ \boldsymbol{\lambda}_{\text{lin}} \end{bmatrix} = \begin{bmatrix} -\sum_a V_a \mathscr{X}_a\times\boldsymbol{T}_a \\ \sum_a V_a \boldsymbol{T}_a \end{bmatrix}, \tag{B.4}$$

with the indicial notation $\left[\hat{\mathscr{X}}_a\right]_{ik} = \mathcal{E}_{ijk}\left[\mathscr{X}_a\right]_j$.

In addition, an extra condition must be added for the satisfaction of the global angular momentum preservation, namely

$$\sum_a V_a \boldsymbol{\mathcal{D}}(\boldsymbol{p}_a) = \boldsymbol{0}; \quad \sum_a V_a \mathscr{X}_a \times \boldsymbol{\mathcal{D}}(\boldsymbol{p}_a) = \boldsymbol{0}. \tag{B.5}$$

Similarly to the least-square minimisation procedure described above, a set of modified upwinding dissipation terms can now be obtained by replacing $\{\hat{\boldsymbol{T}}_a, \boldsymbol{T}_a, \boldsymbol{\lambda}_{\text{lin}}, \boldsymbol{\lambda}_{\text{ang}}\}$ in (B.3) and (B.4) with $\{\hat{\boldsymbol{\mathcal{D}}}(\boldsymbol{p}_a), \boldsymbol{\mathcal{D}}(\boldsymbol{p}_a), \boldsymbol{\mu}_{\boldsymbol{D_p}}, \boldsymbol{\lambda}_{\boldsymbol{D_p}}\}$.

Appendix C. Laplacian evaluation

The artificial compressibility procedure to be employed in this paper to effectively handle near incompressibility regimes may require the evaluation of the Laplacian (harmonic operator [1]) of a solution function. For this purpose, consider the Laplacian of any arbitrary scalar function g to be numerically approximated as

$$\mathcal{L}\left[g(\boldsymbol{X}_a)\right] := \boldsymbol{\nabla}_0\cdot\left[\boldsymbol{\nabla}_0 g(\boldsymbol{X}_a)\right] \approx \sum_{b\in\Lambda_a^b} \boldsymbol{\nabla}_0 g(\boldsymbol{X}_b)\cdot\boldsymbol{G}_b(\boldsymbol{X}_a). \tag{C.1a}$$

Addition of the redundant term $\boldsymbol{\nabla}_0 g(\boldsymbol{X}_a)$ to (C.1a) yields an alternative expression as

$$\mathcal{L}\left[g(\boldsymbol{X}_a)\right] \approx \sum_{b\in\Lambda_a^b} 2\left[\frac{\boldsymbol{\nabla}_0 g(\boldsymbol{X}_a) + \boldsymbol{\nabla}_0 g(\boldsymbol{X}_b)}{2}\right]\cdot\boldsymbol{G}_b(\boldsymbol{X}_a). \tag{C.2}$$

It is worth pointing out that the squared bracket term shown in (C.2) represents the gradient approximation at the mid-edge connecting particles a and b. This can be further approximated via a second order central difference scheme as [64]

$$\left[\frac{\boldsymbol{\nabla}_0 g(\boldsymbol{X}_a) + \boldsymbol{\nabla}_0 g(\boldsymbol{X}_b)}{2}\right] \approx \frac{g_b - g_a}{\|\boldsymbol{X}_b - \boldsymbol{X}_a\|}\boldsymbol{N}_{ab}, \qquad \boldsymbol{N}_{ab} := \frac{\boldsymbol{X}_b - \boldsymbol{X}_a}{\|\boldsymbol{X}_b - \boldsymbol{X}_a\|}. \tag{C.3}$$

For the SPH method under consideration, the normal $\boldsymbol{N}_{ab}$ is defined through a direction vector between particles a and b, as depicted in Figure 3b.

Finally, substitution of (C.3) into (C.2) yields the discrete version of the Laplacian evaluation

$$\mathcal{L}\left[g(\boldsymbol{X}_a)\right] \approx 2 \sum_{b \in \Lambda_a^b} \left[\frac{g_b - g_a}{\|\boldsymbol{X}_b - \boldsymbol{X}_a\|} \boldsymbol{N}_{ab} \right] \cdot \boldsymbol{G}_b(\boldsymbol{X}_a). \tag{C.4}$$

[1] C. H. Lee, A. J. Gil, G. Greto, S. Kulasegaram, J. Bonet, A new Jameson-Schmidt-Turkel Smooth Particle Hdrodynamics algorithm for large strain explicit fast dynamics, Computer Methods in Applied Mechanics and Engineering 311 (2016) 71–111.

[2] C. H. Lee, A. J. Gil, O. I. Hassan, J. Bonet, S. Kulasegaram, A variationally consistent Streamline Upwind Petrov Galerkin Smooth Particle Hydrodynamics algorithm for large strain solid dynamics, Computer Methods in Applied Mechanics and Engineering 318 (2017) 514–536.

[3] M. Aguirre, A. J. Gil, J. Bonet, C. H. Lee, An upwind vertex centred finite volume solver for Lagrangian solid dynamics, Journal of Computational Physics 300 (2015) 387–422.

[4] P. W. Randles, L. D. Libersky, Smoothed Particle Hydrodynamics: Some recent improvements and applications, Computer Methods in Applied Mechanics and Engineering 139 (1996) 375–408.

[5] G. R. Johnson, S. R. Beissel, Normalized smoothing functions for SPH impact computations, International Journal for Numerical Methods in Engineering 39 (1996) 2725–2741.

[6] Y. Vidal, J. Bonet, A. Huerta, Stabilized updated Lagrangian corrected SPH for explicit dynamic problems, International Journal for Numerical Methods in Engineering 69 (2006) 2687–2710.

[7] J. Bonet, S. Kulasegaram, Remarks on tension instability of Eulerian and Lagrangian Corrected Smooth Particle Hydrodynamics (CSPH) methods, International Journal for Numerical Methods in Engineering 52 (2001) 1203–1220.

[8] G. C. Ganzenmüller, An hourglass control algorithm for Lagrangian Smooth Particle Hydrodynamics, Computer Methods in Applied Mechanics and Engineering 286 (2015) 87–106.

[9] G. C. Ganzenmüller, S. Hiermaier, M. May, On the similarity of meshless discretizations of Peridynamics and Smooth-Particle Hydrodynamics, Computers and Structures 150 (2015) 71–78.

[10] S. A. Silling, Reformulation of elasticity theory for discontinuities and long-range forces, Journal of the Mechanics and Physics of Solids 48 (2000) 175–209.

[11] J. J. Monaghan, SPH without a tensile instability, Journal of Computational Physics 159 (2000) 290–311.

[12] M. A. Puso, J. S. Chen, E. Zywicz, W. Elmer, Meshfree and finite element nodal integration methods, International Journal for Numerical Methods in Engineering 74 (2008) 416–446.

[13] J. W. Swegle, D. L. Hicks, S. W. Attaway, Smoothed Particle Hydrodynamics stability analysis, Journal of Computational Physics 116 (1995) 123–134.

[14] T. Belytschko, Y. Guo, W. K. Liu, S. P. Xiao, A unified stability analysis of meshless particle methods, International Journal for Numerical Methods in Engineering 48 (2000) 1359–1400.

[15] J. Bonet, A. J. Burton, A simple average nodal pressure tetrahedral element for incompressible and nearly incompressible dynamic explicit applications, Communications in Numerical Methods in Engineering 14 (1998) 437–449.

[16] M. W. Gee, C. R. Dohrmann, S. W. Key, W. A. Wall, A uniform nodal strain tetrahedron with isochoric stabilization, International Journal for Numerical Methods in Engineering 78 (2009) 429–443.

[17] C. R. Dohrmann, M. W. Heinstein, J. Jung, S. W. Key, W. R. Witkowski, Node-based uniform strain elements for three-node triangular and four-node tetrahedral meshes, International Journal for Numerical Methods in Engineering 47 (2000) 1549–1568.

[18] M. A. Puso, J. Solberg, A stabilized nodally integrated tetrahedral, International Journal for Numerical Methods in Engineering 67 (2006) 841–867.

[19] J. J. Monaghan, Smoothed particle hydrodynamics, Annual Review of Astronomy and Astrophysics 30 (1992) 543–574.

[20] P. W. Randles, L. D. Libersky, Normalized SPH with stress points, International Journal for Numerical Methods in Engineering 48 (2000) 1445–1462.

[21] J. S. Chen, C. T. Wu, S. Yoon, Y. You, A stabilized conforming nodal integration for Galerkin mesh-free methods, International Journal for Numerical Methods in Engineering 50 (2001) 435–466.

[22] M. B. Liu, G. R. Liu, K. Y. Lam, Constructing smoothing functions in smoothed particle hydrodynamics with applications, Jounal of Computational and Applied Mathematics 155 (2003) 263–284.

[23] J. K. Chen, J. E. Beraun, T. C. Carney, A corrective smoothed particle method for boundary value problems in heat conduction, International Journal for Numerical Methods in Engineering 46 (1999) 231–252.

[24] J. Bonet, S. Kulasegaram, Correction and stabilization of smooth particle hydrodynamics methods with applications in metal forming simulations, International Journal for Numerical Methods in Engineering 47 (2000) 1189–1214.

[25] J. Bonet, A. J. Gil, C. H. Lee, M. Aguirre, R. Ortigosa, A first order hyperbolic framework for large strain computational solid dynamics. Part I: Total Lagrangian isothermal elasticity, Computer Methods in Applied Mechanics and Engineering 283 (2015) 689–732.

[26] A. J. Gil, C. H. Lee, J. Bonet, M. Aguirre, A stabilised Petrov-Galerkin formulation for linear tetrahedral elements in compressible, nearly incompressible and truly incompressible fast dynamics, Computer Methods in Applied Mechanics and Engineering 276 (2014) 659–690.

[27] C. H. Lee, A. J. Gil, J. Bonet, Development of a stabilised Petrov-Galerkin formulation for conservation laws in Lagrangian fast solid dynamics, Computer Methods in Applied Mechanics and Engineering 268 (2014) 40–64.

[28] R. Courant, K. Friedrichs, H. Lewy, On the partial difference equations of mathematical physics, Mathematische Annalem 100 (1928) 32–74.

[29] A. J. Gil, Z. Zhang, O. Hassan, K. Morgan, Parallel multigrid detached eddy simulation algorithm for three-dimensional unsteady incompressible flows on unstructured grids, Journal of Aerospace Engineering 19 (2006) 271–280.

[30] A. J. Gil, C. H. Lee, J. Bonet, R. Ortigosa, A first order hyperbolic framework for large strain computational solid dynamics. Part II: Total Lagrangian compressible, nearly incompressible and truly incompressible elasticity, Computer Methods in Applied Mechanics and Engineering 300 (2016) 146–181.

[31] A. J. Chorin, The numerical solution of the Navier-Stokes equations for an incompressible fluid, Bulletin of the American Mathematical Society 73 (1967) 928–931.

[32] A. J. Chorin, Numerical solution of the Navier-Stokes equations, Mathematics of Computation 22 (1968) 745–762.

[33] A. J. Chorin, On the convergence of discrete aapproximations to the Navier-Stokes equations, Mathematics of Computation 23 (1969) 341–353.

[34] C. H. Lee, A. J. Gil, J. Bonet, Development of a cell centred upwind finite volume algorithm for a new conservation law formulation in structural dynamics, Computers and Structures 118 (2013) 13–38.

[35] I. A. Karim, C. H. Lee, A. J. Gil, J. Bonet, A two-step Taylor Galerkin formulation for fast dynamics, Engineering Computations 31 (2014) 366–387.

[36] G. Kluth, B. Després, Discretization of hyperelasticity on unstructured mesh with a cell-centered Lagrangian scheme, Journal of Computational Physics 229 (2010) 9092–9118.

[37] N. C. Nguyen, J. Peraire, Hybridizable Discontinuous Galerkin methods for partial differential equations in continuum mechanics, Journal of Computational Physics 231 (2012) 5955–5988.

[38] M. Aguirre, A. J. Gil, J. Bonet, A. A. Carreño, A vertex centred finite volume Jameson-Schmidt-Turkel (JST) algorithm for a mixed conservation formulation in solid dynamics, Journal of Computational Physics 259 (2014) 672–699.

[39] J. Bonet, A. J. Gil, R. Ortigosa, On a tensor cross product based formulation of large strain solid mechanics, International Journal of Solids and Structures 84 (2016) 49–63.

[40] J. Bonet, A. J. Gil, R. Ortigosa, A computational framework for polyconvex large strain elasticity, Computer Methods in Applied Mechanics and Engineering 283 (2015) 1061–1094.

[41] J. A. Trangenstein, P. Colella, A higher-order Godunov method for modelling finite deformation in elastic-plastic solids, Communications on Pure and Applied Mathematics 44 (1991) 41–100.

[42] J. Haider, C. H. Lee, A. J. Gil, J. Bonet, A first order hyperbolic framework for large strain computational solid dynamics: An upwind cell centred Total Lagrangian scheme, International Journal for Numerical Methods in Engineering 109 (2017) 407–456.

[43] J. Bonet, A. J. Gil, R. D. Wood, Nonlinear Solid Mechanics for Finite Element Analysis: Statics, Cambridge University Press, 2016.

[44] J. E. Marsden, T. J. R. Hughes, Mathematical foundations of elasticity, Dover Publications, 1994.

[45] J. M. Ball, Energy-minimising configurations in nonlinear elasticity, Archive for Rational Mechanics and Analysis 63 (1976) 337–403.

[46] J. M. Ball, Convexity conditions and existence theorems in nonlinear elasticity, Archive for Rational Mechanics and Analysis 63 (1976) 337–403.

[47] J. Bonet, T.-S. Lok, Variational and momentum preservation aspects of smooth particle hydrodynamic formulations, Computer Methods in Applied Mechanics and Engineering 180 (1999) 97–115.

[48] G. R. Johnson, R. A. Stryk, S. R. Beissel, SPH for velocity impact computations, Computer Methods in Applied Mechanics and Engineering 139 (1996) 347–373.

[49] R. L. Leveque, Finite volume methods for hyperbolic problems, Cambridge University Press, 2002.

[50] E. F. Toro, Riemann solvers and numerical methods for fluid dynamics: A practical introduction, Springer-Verlag, second edition, 2006.

[51] A. Huerta, S. Fernández-Méndez, Enrichment and coupling of the finite element and meshless methods, International Journal for Numerical Methods in Engineering 48 (2000) 1615–1636.

[52] A. Huerta, S. Fernández-Méndez, Locking in the incompressible limit for the element-free Galerkin method, International Journal for Numerical Methods in Engineering 51 (2001) 1361–1383.

[53] K. J. Bathe, Finite element procedures, Prentice Hall, 1996.

[54] S. Fernández-Méndez, A. Huerta, Continuous blending of SPH with finite elements, Computes and Structures 83 (2005) 1448–1458.

[55] J. P. Gray, J. J. Monaghan, R. P. Swift, SPH elastic dynamics, Computer Methods in Applied Mechanics and Engineering 190 (2001) 6641–6662.

[56] R. Vignjevic, J. Campbell, L. Libersky, A treatment of zero-energy modes in the smoothed particle hydrodynamics method, Computer Methods in Applied Mechanics and Engineering 184 (2000) 67–85.

[57] M. A. Puso, A highly efficient enhanced assumed strain physically stabilized hexahedral element, International Journal for Numerical Methods in Engineering 49 (2000) 1029–1064.

[58] G. Scovazzi, B. Carnes, X. Zeng, S. Rossi, A simple, stable, and accurate linear tetrahedral finite element for transient, nearly and fully incompressible solid dynamics: A dynamic variational multiscale approach, International Journal for Numerical Methods in Engineering 106 (2016) 799–839.

[59] J. C. Simo, N. Tarnow, A new energy and momentum conserving algorithm for the non-linear dynamics of shells, International Journal for Numerical Methods in Engineering 37 (1994) 2527–2549.

[60] Y. Onishi, K. Amaya, A locking-free selective smoothed finite element method using tetrahedral and triangular elements with adaptive mesh rezoning for large deformation problems, International Journal for Numerical Methods in Engineering 99 (2014) 354–371.

[61] E. Boatti, G. Scalet, F. Auricchio, A three-dimensional finite-strain phenomenological model for shape-memory polymers: Formulation, numerical simulations, and comparison with experimental data, International Journal of Plasticity 83 (2016) 153–177.

[62] A. J. Gil, A. A. Carreño, J. Bonet, O. Hassan, The Immersed Structural Potential Method for haemodynamic applications, Journal of Computational Physics 229 (2011) 8613–8641.

[63] A. J. Gil, , A. A. Carreño, J. Bonet, O. Hassan, An enhanced Immersed Structural Potential Method for fluid-structure interaction, Journal of Computational Physics 250 (2013) 178–205.

[64] J. P. Morris, P. J. Fox, Y. Zhu, Modeling low Reynolds number incompressible flows using SPH, Journal of Computational Physics 136 (1997) 214–226.